UNIVERSITÀ
DEGLI STUDI
DI PADOVA

Head Office: Università degli Studi di Padova

Department: Industrial Engineering

PhD Course: Space Sciences, Technologies and Measurements

Curriculum: Mechanical Measurements for Engineering and Space

Series: XXX Cycle

Tethers for Deorbit of Objects in High Eccentricity Orbits at the End-of-Life

Thesis written with the financial contribution of
Fondazione Cariparo (*Cassa di Risparmio di Padova e Rovigo*)

Coordinator: Prof. Giampiero NALETTO

Supervisor: Prof. Enrico LORENZINI

Co-Supervisor: Ing. Marco PERTILE

PhD Student: Ing. Guido PASTORE

This PhD thesis is dedicated to my family.

Abstract

The present PhD research investigates the removal from orbit (i.e. deorbit) of inactive objects in high eccentricity orbits, considering as specific target *Sylda*, a large dual-payload adapter used onboard *Ariane 5* heavy launches to Geostationary Earth Orbit (GEO), and released in Geostationary Transfer Orbit (GTO). The population of space debris always increased since the start of space activities, due to the fact that deorbit procedures were never implemented so far. The adoption of a deorbit system, onboard payloads or other objects delivered into space in the future, is an effective solution to significantly attenuate the otherwise exponentially increasing debris density and consequent collision risk in space. The deorbit is performed with a dedicated system that dissipates orbital energy, causing a gradual decrease of orbital altitude until the object degrades while reentering the Earth's atmosphere. Deorbit from Low Earth Orbits (LEO) has been widely studied in literature, whereas very little is present regarding deorbit from GTO or other high eccentricity orbits, even if such objects are very important targets for removal since the cross continuously both highly valuable zones of LEO and GEO. International guidelines for space debris attenuation set 25 years as maximum time for removal from orbit. The present research employs a *Bare Electrodynamic Tether* (BET) as deorbit device: such tape tether creates a Lorentz drag from the interaction between the current circulating along the tether, from the collection of electrons from space plasma, and the geomagnetic field. *Sylda* is a major threat from the collision risk standpoint, given its very large exposed area and high mass, and therefore it is an optimal candidate for deorbit implementation, also due to the high rate of dual-payload launches to GEO. The research covers both the numerical simulation and analysis of deorbit and of pre-deorbit procedures. Regarding deorbit, two main simulation campaigns are performed: the first simulates the deorbit on the orbital plane, neglecting the out-of-plane oscillations of the system. One of the main outcomes from this first batch of analyses is that the optimal configuration for the tethered system is having one electrodynamic tether subdivided in two segments deployed along opposite directions from Sylda: this is called *butterfly* configuration. A second phase of deorbit analysis follows, with a different computational model, adopting the *butterfly* configuration, and including also the out-of-plane dynamics of the system. Before starting the deorbit from GTO, two procedures must be performed: at first the detumbling of *Sylda*, i.e. the minimization of the residual angular velocity of rotation of Sylda around its center of mass. This procedure is analyzed proposing a set of magnetic torquers to accomplish this task. After detumbling is complete, the deployment of the tethers can start. The deployment is then simulated, accounting for three different options: deployment at apogee, at perigee, or at mid-way along the initial orbit, the last resulting as the most favorable location. Another part of research is dedicated to the study of the attitude detection of the two tether segments of the butterfly configuration, during deployment, using a vision system that tracks the tip-mass at the end of each tether. An analysis is performed to estimate the uncertainty affecting the measure, considering two main configurations for the vision system, i.e. a *monocular* system and a *stereo* system.

Contents

List of Figures

List of Tables

List of Symbols

a	Semi-major axis of orbit 52
α	Angle of rotation of Sylda on the orbital plane during deployment . 91
$\boldsymbol{B}$	Earth's magnetic field 54
c_d	Aerodynamic drag coefficient 54
e	Eccentricity of orbit 52
$\boldsymbol{E}_t$	Electrical Field component along the tether 54
$\boldsymbol{F}_{atm}$	Atmospheric drag force 141
$\boldsymbol{F}_L$	Lorentz Drag Force 40
f_r	Perturbation acceleration (force per unit mass) along the R direction in the RSW reference system 70
f_s	Perturbation acceleration (force per unit mass) along the S direction in the RSW reference system 70
f_w	Perturbation acceleration (force per unit mass) along the W direction in the RSW reference system 70
h_t	Thickness of tether 50
i	Orbital inclination 67
$\overline{i_{av}}$	Normalized average current along the electrodynamic tether 54
$\overline{i_B}$	Normalized maximum current along at the zero-bias point B 57
i_{sc}	Short circuit current along electrodynamic Tether 54
J^G	Moment of inertia of the entire system with respect to its center of mass G and about the axis orthogonal to the orbital plane 52
$J_{S,x}$	Moment of inertia of Sylda around the first body axis 26
$J_{S,y}$	Moment of inertia of Sylda around the second body axis 26
$J_{S,z}$	Moment of inertia of Sylda around the third body axis 26
L_t	Total tether length 50
L_{t1}	Length of first tether segment in case of butterfly configuration . . 102
L_{t2}	Length of second tether segment in case of butterfly configuration 102
L_*	Characteristic tether length 58
L_1	Length of first segment of tether in case of butterfly configuration . 67
L_2	Length of second segment of tether in case of butterfly configuration 67
m_A	Anodic tip-mass 50
m_C	Cathodic tip-mass 50
m_e	Electron mass 54
m_S	Mass of Sylda or other object to deorbit (spacecraft or other) 51
m_t	Mass of tether 50
M^G	Total torque with respect to the axis orthogonal to the orbital plane and passing through the system's center of mass G 56
N_e	Electron number density 54

List of Acronyms

ATP Area-Time Product

BET Bare Electrodynamic Tether

EDT ElectroDynamic Tether

ECP ElectroDynamic Center of Pressure

EOL End-Of-Life

FEAC Field Emitter Array Cathodes

FOV Field of View

GEO Geostationary Earth Orbit

GTO Geostationary Transfer Orbit

HEO High Eccentricity Orbit

IGRF International Geomagnetic Reference Field

IRI International Reference Ionosphere

LEO Low Earth Orbit

OML Orbital Motion Limited

PDF Probability Density Function

Chapter 1

Introduction

1.1 The orbital debris problem

Since the start of space activities, in the late '50s, default procedures for removing satellites and other objects launched into Earth orbits, after their end of operational life, were never implemented. The procedure of removal from orbit is called in literature, and will also be called in this thesis, as *deorbit*.
Among all the objects sent to space since that time, only a very little number of them reentered by natural decay due to atmospheric drag: the rest remained orbiting in space, causing an increase in collisions and fragmentation events. As a consequence, the debris population constantly rose up over time, as displayed in Fig.1.1. Nowadays, the number of expected collisions, due to the exponential increase of debris population, is growing too large: therefore, for the sake of future space exploitation, a solution for space debris removal is urgently needed.

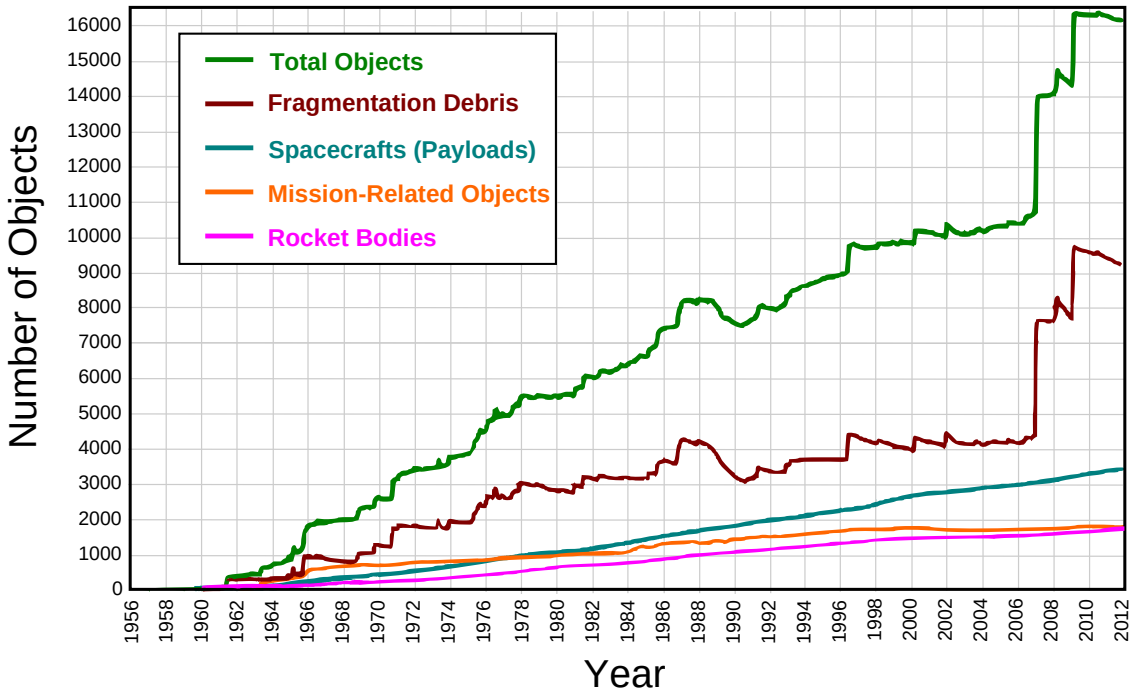

Figure 1.1: *Evolution in number of artificial cataloged objects in space, from 1956 to 2012.*

Any collision in space creates hundreds to thousands of new space debris. As of now,the majority of cataloged orbital debris is made of fragments from collisions (see Fig. 1.3). Large objects like inactive satellites, spent upper stages, and payload adapters are the main sources of debris propagation, due to their large cross section that makes them statistically the most likely objects to be involved in collisions. In case of collision, thousands of new debris can be generated, covering a broad spectrum of sizes. For example, in February 2009, a defunct Russian communication satellite, *Cosmos 2251*, collided with an operational Iridium spacecraft, leading to nearly 2000 new trackable objects and, most likely, tens of thousands of smaller, but still very dangerous, fragments.

The highest concentration of space debris is reached in the Low-Earth-Orbits (LEO) region, but debris are also significantly present in GTO and other high eccentricity orbits, as shown in Fig. 1.2. Debris in GEO are a lighter problem, since they do not cross the LEO region, where most of the active payloads are located; moreover, the solution for GEO, once a payload becomes inactive, it is generally to reboost them in sligthly higher or lower regions of space not employed by active missions. Objects in GTO or High-Eccentricity-Orbits (HEO), such as Molnija orbits, are instead a much higher problem, since they cross continuously both highly valuable zones of LEO, and GEO. Such objects are then important targets for orbit removal procedures.

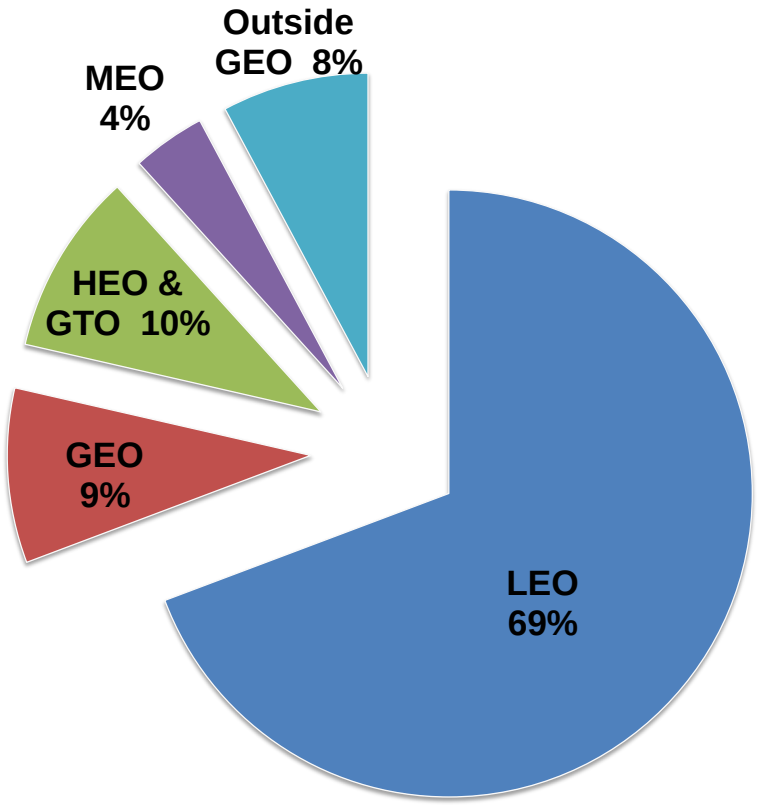

Figure 1.2: *All cataloged space objects, classified by orbital region, as of January 2002. Values from Ref.[21].*

Fig.1.3 displays all the man-made objects orbiting around the Earth: surprisingly, only 6% is made of active payloads, the rest being inactive and unwanted debris. Most of debris come from fragmentation events, i.e. 40% of the total. Inactive payloads, mission related objects (such as dual-payload adapters), and spent rocket stages, they amount in total to 54% of cataloged objects population: this 54% includes all the objects whose abandonment in space can be avoided in future missions, once deorbit systems are finally implemented onboard.

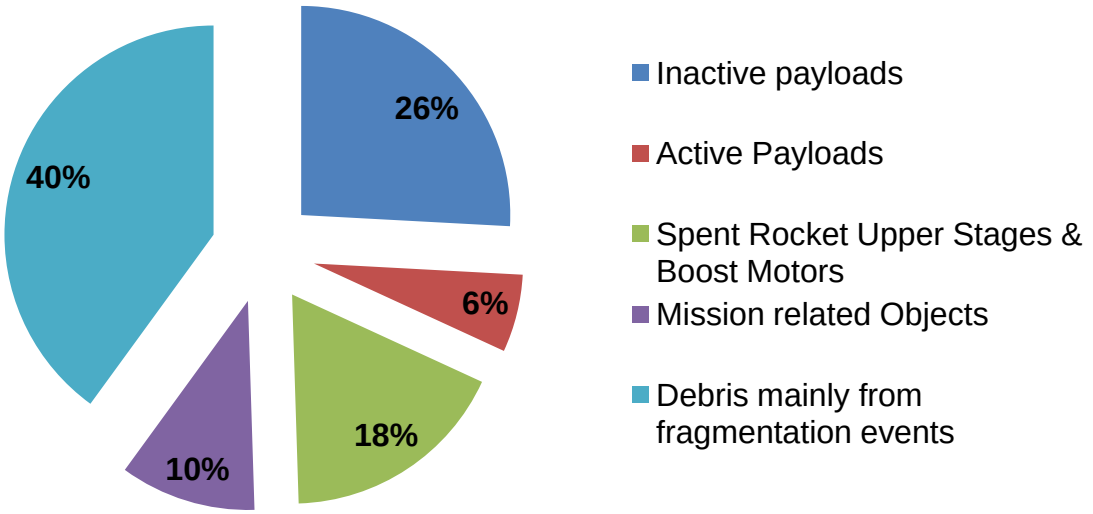

Figure 1.3: *All cataloged space objects, classified by object type, as of January 2002. Values from Ref.[21].*

The objects orbiting around the Earth can be categorized as shown in the diagram below.

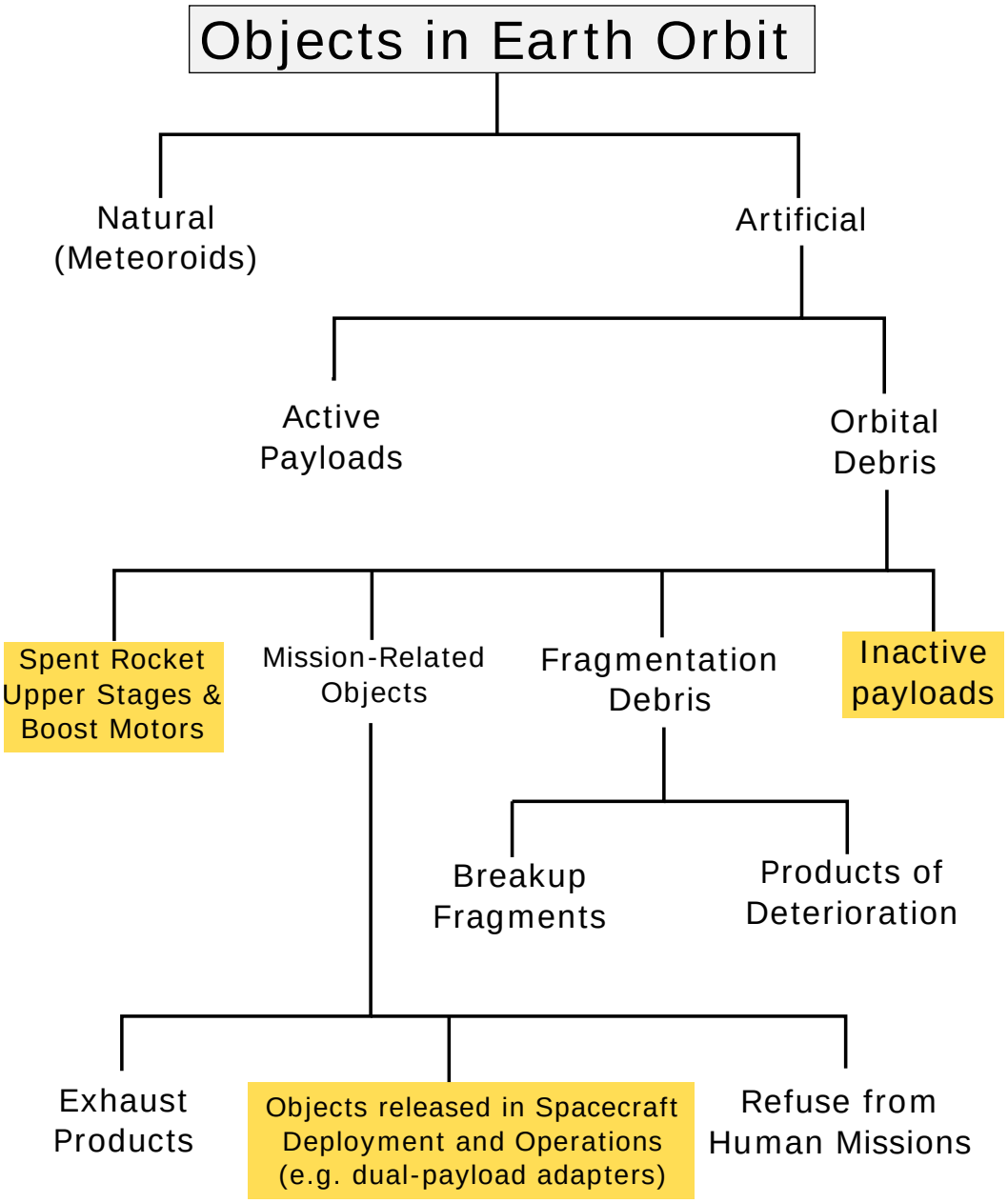

Figure 1.4: *Classification of objects in Earth orbits. The objects that can be enabled with a deorbit system are highlighted.*

As reported in Ref.[21], an effective and inexpensive measure for long-term debris mitigation is to act on objects launched to space in the future: this means to provide these objects, delivered into Earth orbits in the future, with a system, activated at their end-of-life, to lower their orbit until they degrade in atmosphere. Lowering the orbit means to dissipate orbital energy and to increase the orbital velocity (this is the so-called *satellite paradox*, see Ref. [28] for more details). Reorbiting inactive satellites to higher storage orbits is convenient only for GEO satellites: for any other orbit, i.e. LEO, MEO and high-eccentricity orbits, this solution is not viable.

Ref.[21] provides numerical estimates of what would happen in LEO if no deorbit mea-

sure is taken, in a time span of 100 years from year 2000 (*business-as-usual* scenario): the number of objects with diameter d larger than 1 m, in LEO orbits, would increase fourfold. It is considered the annual trend of launches of new objects in LEO orbits, plus a typical annual rate of fragmentation occurrences in orbit. From approximately 2000 objects with $d > 1$ m in year 2000, it would be reached a number of about 8000 objects with $d > 1$ m in year 2100. Moreover, the expected number of catastrophic collisions in LEO orbits during the 100 years would be higher than 50. This would determine a steep growth of massive objects and even higher increase of smaller debris, leading in year 2100 to a number of about 50000 objects in LEO with $d > 10$ cm (with respect to the current 10000, hence a five-fold increase), and a number of about 1.6e+06 objects with $d > 1$ cm (with respect to the current number of about 3e+05, thus again an approximately five-fold increase). This study regards directly also objects in high-eccentricity orbits, that continuously cross the entire LEO region.

Ref.[21] also reports that the most effective mitigation measure is the mass removal from orbit (deorbit), with priority for objects with mass higher than 100 kg (hence spent rocket bodies, dual-payload adapters, and inactive satellites), especially from orbital regions with high debris densities, such as LEO. International regulations for debris attenuation are present, and they set 25 years as the maximum time for deorbit (e.g. see Ref.[1]). This maximum allowed time comes from from the following facts (see Fig.1.5):

- regardless of the specific *debris mitigation* scenario, even when deorbit times are extremely long (e.g. 100 years), the number of collisions would still significantly decrease over 100 years. Between the *Business-as-Usual* scenario and the 100-years deorbit scenario, there is a difference of more than 30 collisions.
- comparing a 25-year deorbit scenario for all future inactive objects, with a *direct* deorbit (0 years curve in Fig.1.5), there is only a slight difference in cumulative number of collisions, over the 100 years span (about 3 collisions). The difference in number of collisions grows much more significantly when going from a 25-year deorbit scenario to a 100-year deorbit scenario. Choosing 25 years deorbit procedures, instead of direct deorbit, allows to significantly reduce the cost of deorbit and the dedicated system.

In summary, the cumulative number of catastrophic collisions would exponentially increase if no deorbit measure is taken in the near future, on a 100-year time span. However, if deorbit procedures were to be implemented, with maximum removal time of 25 years, as set by international guidelines (Ref.[1]), the problem would be consistently healed, with less than 10 catastrophic collisions expected in 100 years instead of more than 50 in a business-as-usual scenario[21].

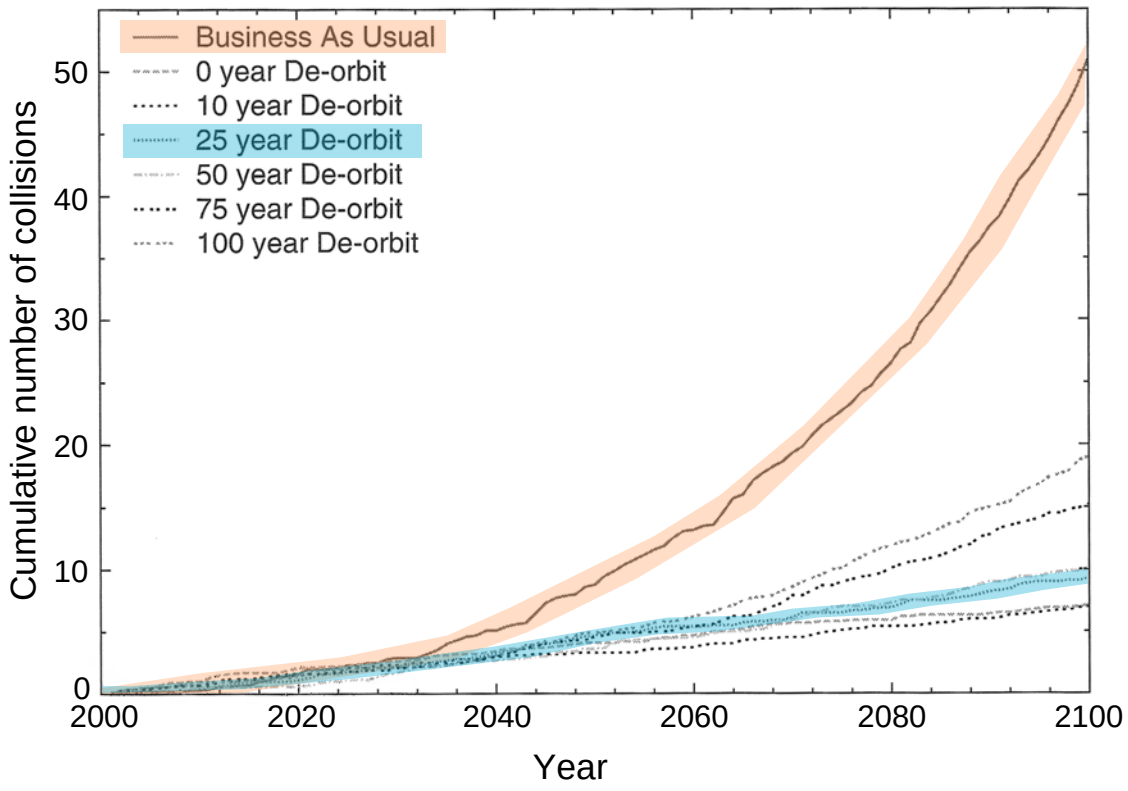

Figure 1.5: *Evolution of cumulative number of catastrophic collisions in LEO region, over 100 years starting from year 2000. Different curves allow comparison between* business-as-usual *scenario, and scenarios with mitigation measures plus deorbit of inactive payloads. Different curves are computed, in case of* debris mitigation *scenario, for different deorbit times.*

As reported in Ref.[21], [1], the debris mitigation guidelines from *NASA*, *US Government*, *ESA*, *CNES*, *EDMS*, and *JAXA*, they all set **25 years** as maximum time for re-entry of any object in orbit, after its operational life, in case it is not economically convenient a direct retrieval or not viable the re-orbiting to higher orbits.

For more massive objects that might survive re-entry, the guidelines prescribe a *controlled re-entry*. The NASA guideline also sets 10 years as maximum allowed time in case of planned retrieval, i.e. in any case in which the satellite during deorbit is traveling across valuable regions of space. Consequently, the 25 years constraint must be interpreted as a general maximum constraint, but it is preferable to have a much lower deorbit time, possibly lower than 10 years. In fact, the more an objects remains in orbit, the higher is the collision risk. At the same time the deorbit solution must be low-cost: this leads to a system that must be technologically simple, possibly passive or with very little energy required, and with low mass. Electrodynamic tether systems have these features, and they are consequently worth of further study, especially regarding their dynamics during all the phases of deorbit.

1.2 Deorbit solutions

The solutions for debris mitigation explored in scientific literature are mainly the following ones:

1. **Natural Decay**
2. ***Active* systems**:
    - *Chemical Propulsion*
    - *Electrical Propulsion*
3. ***Passive* systems** (a very low amount of energy might be required only during the deployment of the device):
    - *Drag Augmentation devices*: inflatable (*aerodynamic drag balloons*) and non-inflatable, i.e. supported by rigid booms (*aerodynamic drag sails*).
    - *Electrodynamic Tether (EDT)* systems. Electrodynamic tethers proved to work successfully in space, e.g. in missions PMG (1993) and TSS-1R (1996), but have never been used for deorbit so far. In particular, *Bare Electrodynamic Tethers* (BETs), equipped with a hollow cathode for electron emission, have been studied and proposed in literature (e.g. in Ref.[3, 45, 13]) as an effective deorbit device for various applications.

Candidates for deorbit application are all the objects on orbits with perigee crossing the LEO region: this includes all the LEO satellites, but also objects in high eccentricity orbits.

Considering objects in LEO, the natural decay (i.e. energy dissipation due to aerodynamic drag) allows reentry in a time lower than 25 years only for objects orbiting at altitude below about 500–700 km (the precise value depending on the mass and aerodynamic drag area of the body). However, only a very low percentage of LEO objects are orbiting below 500 km, i.e. about 10% of the total: for these bodies, deorbit devices are not strictly necessary.

About 25% of LEO population is made of objects orbiting at altitudes between 500 km and 700 km: for all the objects that would not naturally reenter in 25 years, a deorbit device is needed. In this altitude range, effective solutions are either using a *Chemical Propulsion* system, if shortest deorbit time and lowest Area-Time-Product are top priorities. The Area-Time-Product (ATP) is a measure of collision risk, since it is the product of the exposed area (including deorbit device) of the object to deorbit multiplied by the time it takes to deorbit it. Hence, it is desirable to minimize the ATP, but a compromise with cost of implementation must be found. In fact, *Electrodynamic Tether* systems are applicable too in that altitude region, and have the potential be the most economically convenient option since they lead to a mass considerably lower, in some cases about half, than the mass required for a direct reentry with *Chemical Propulsion*, as showed in Ref.[31].

The most populated LEO region is the one between 700 km and 1500 km, with about 65% of all LEO satellites and spent stages. In this range, effective solutions for deorbit are either the *Electrodynamic Tether* systems, or the *Electrical Propulsion* systems. Chemical propulsion can be used only for lower orbits in this range, otherwise the mass of required propellant becomes too high. *Electrical Propulsion* is generally not present onboard LEO missions and the addition of it just for deorbit purposes might be not well perceived given the generally high cost of an electrical propulsion system. Moreover, it is an active system that requires active attitude control: it would not be mountable on spent stages for example or dual-payload adapters. Eventually, Electrodynamic Tethered (EDT) systems have the potential to be an optimal solution for a large amount of LEO satellites, being a simple and cheap system in comparison to other solutions.

Moreover, EDT systems, and more specifically Bare Electrodynamic Tether systems (BET), can be used onboard objects like spent stages or dual-payload adapters orbiting in high-eccentricity orbits, such as in Geostationary Transfer Orbit (GTO). Additionally, mounting chemical propulsion or electrical propulsion systems outside the walls of spent stages or dual-payload adapters might also be not allowed by manufacturers due to the inherent risk of having a propulsion system lying between these components and the fairing walls of a launch system.

Ref. [31] showed with numerical simulations that Aerodynamic Drag Augmentation devices are generally never a good solution for deorbit since they have an Area-Time-Product always higher than other solutions.

Among all the solutions for deorbit investigated in literature, Bare Electrodynamic Tether systems showed, through numerical simulations (e.g. see Ref.[11]), to be capable of complying, and with a large margin, with the time constraint of 25 years for orbit removal. BET systems, equipped with a hollow cathode for electron emission, are proposed in various literature references (Ref.[3, 45, 13]) as a cheap, low-mass, and easily implementable solution for deorbiting objects from LEO.
The present research, given this application potential of electrodynamic tether systems, aims to expand the study of deorbit, with such systems, of objects that are left in high eccentricity orbits, at the end of their operational life.

1.3 Objects in high-eccentricity orbits

In addition to bodies in LEO over 500–700 km, there are also several objects in high eccentricity orbits that would not reenter naturally in 25 years: these objects might have a very low perigee, as low as 300 km, where the aerodynamic drag is consistent. However, they spend most of the orbital time at high altitudes, where the atmospheric drag is negligible, since the transit through the perigee region is very fast.

A report by Fisher and David (Ref.[19]) points out that 294 mission-related objects were left in GTO in the period between 2004 and 2012, including upper stages, fuel tanks, and dual-payload adapters. Only 43 objects re-entered by natural decay. All the others cross continuously both highly valuable zones of LEO and GEO, making these inactive objects a threat to operational satellites. Among all these objects left in GTO, dual-payload adapters are particularly massive and have a very large exposed area: the combination of these two factors makes them the most dangerous objects in GTO, due to the high risk of collision with other objects in space. *Inter-stage adapters*, or *dual-payload adapter*, are structures employed onboard launches to GEO in order to house two separate payloads inside the fairing: a first payload is stored inside the adapter, and a second one on its top. An example of such object is *Sylda-5* (*Système de Lancement Double Ariane 5*), used onboard *Ariane 5* heavy launches to GEO.

1.3.1 Sylda and dual-payload adapters

As previously stated, very interesting targets for deorbit application are the dual-payload adapters released in Geostationary Transfer Orbit (GTO) during the last phase of insertion of a double-payload in Geostationary Earth Orbit (GEO). A most significant example is Sylda, given the persistent launch rate of dual-payloads to GEO orbits with the Ariane 5 launch system. Therefore, finding an optimal deorbit device for Sylda has a high commercial relevance.

Moreover, *Sylda* is a major threat for operational satellites, being a massive hollow structure with very large exposed area: it is then a major contributor to collision risk in space.
Every payload that is launched to GEO employs a Geostationary Transfer Orbit (GTO), performing a transfer from a LEO parking orbit, e.g. at altitude of 300 km, up to the GEO altitude at about 35786 km. Shortly before the apogee burn with orbit circularization and inclination change, the dual-payload adapter is released in GTO nearby its apogee.

Sylda has the following features, reported in the *Ariane 5 User Manual* (2016 version):

- It is a bell-shaped hollow structure with diameter 4.5 m and variable height, depending on the specific configuration, from 5 m up to about 7 m.
- It is made of an Aluminum honeycomb core covered by carbon fiber sheets.
- The mass ranges from 425 kg, for the mimimum height configuration, up to 535 kg for the maximum height configuration.
- Its orbit has a perigee at about 300 km, apogee approximately at GEO altitude, inclination of 6°. Precise values of these orbital parameters depend on the specific launch configuration.

Figure 1.6: On the left: Sylda 5 *support structure being lowered over the* Planck *spacecraft (27 April 2009). This view up along the Planck spacecraft gives a look inside the SYLDA 5, with its tapered base, high cylindrical shell and an upper truncated conical shell.* Sylda 5 *is used here to carry the Herschel spacecraft on top of the Planck spacecraft during their joint launch. Photo courtesy of ESA.* On the right: *exploded view of the Ariane 5 payload module.*

Sylda, and dual-payload adapters in general, they are massive but have thin walls, i.e. they have a large area-to-mass ratio: therefore, they are expected to degrade completely in the atmosphere during reentry, without need of a controlled reentry

procedure. Sylda is widely used, given the high rate of launches using the Ariane 5. According to a study by Fisher and David (Ref.[19]), among 43 launches with *Ariane 5*, 43 upper stages and 40 *Sylda* adapters were released in GTO. Only 5 *Sylda*, all of them with very low initial perigee (229–268 km), re-entered between 1 to 7 years after launch, and none of the upper stages.

An accurate model of Sylda, whose features are used in numerical computations presented in this thesis, is created with *Solidworks*. The selected configuration of Sylda used in numerical models is close to the maximum height, and has these main features: diameter of cylindrical part of 4.5 m; height of 6.81 m; material average density of 180 kg/m^3; wall thickness of 3 cm. The resulting mass is 536 kg. The moments of inertia, with respect to Sylda's center of mass, about the principal axes of inertia of the body frame, are $J_{S,x} = J_{S,y} = 3459.44\,\text{kgm}^2$ and $J_{S,z} = 2632.24\,\text{kgm}^2$ where Z is the longitudinal axis of Sylda, while X and Y are transversal axes. These axes are fixed with Sylda, i.e. they are body-frame axis X_B, Y_B, Z_B, with respective unit vectors $\boldsymbol{u}_\xi$, $\boldsymbol{u}_\eta$, $\boldsymbol{u}_\zeta$ (refer to Appendix B). The mass and inertia properties are computed, given the geometry and the material density as inputs, using *Solidworks*.

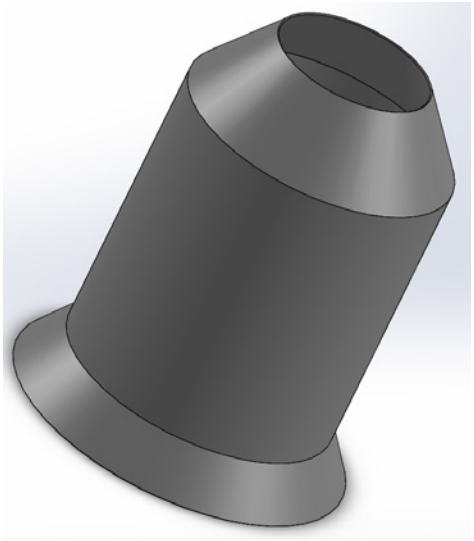

Figure 1.7: *Model of Sylda in* Solidworks

Different solutions were attempted in the past in order to remove *Sylda* from orbit in a time lower than 25 years. Mainly, either by setting a low initial perigee, penalizing the launcher capacity (about 200 kg less for *Ariane 5*), or launching with favorable Sun-synchronous resonance conditions, with no sure warranty to comply with the 25 years guideline, or anyhow with very high deorbit times. Hence, the research about a faster and cheap solution for deorbit of Sylda, based on Bare Electrodynamic Tethers, corresponds to an actual commercial need.

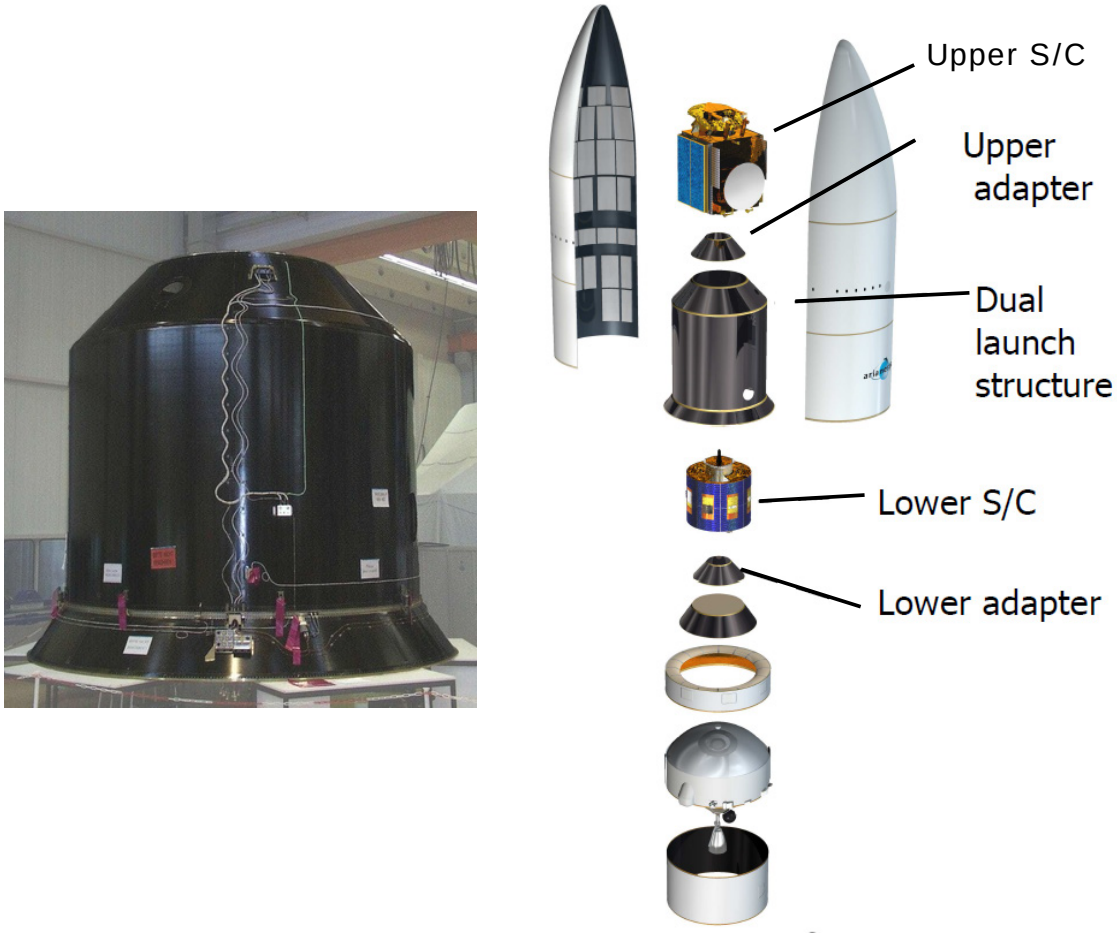

Figure 1.8: On the left*: photo of Sylda dual-payload adapter. Courtesy of* ArianeSpace. On the right*: Exploded view of upper stage of Ariane 5 launch system. Courtesy of* ArianeSpace.

1.4 Bare Electrodynamic Tether (BET) system

The deorbit system studied in this PhD thesis is based on a *Bare Electrodynamic Tether*, i.e. a system that exploits an electrodynamic process in order to dissipate orbital energy and consequently lower the orbital altitude of the object, until it completely degrades in the lower layers of the atmosphere. This result is obtained by generating a *Lorentz drag force* created by the relative motion of the tether, with an electrical current running through, with respect to the Earth's magnetic field. The electrical current is created by collecting electrons, impacting on the tether from the ambient plasma. The tether is traveling either in the *F-Layer* of the *ionosphere*, for altitudes lower than about 1000 km, or in the *plasmasphere* for higher altitudes. The electron density varies with several parameters, including orbital altitude, latitude, longitude, and solar activity. For altitudes higher than 2000 km, regardless of the other variables, the electron density becomes negligible. A profile of electron number density is extracted from the NASA *IRI* database, and posted below. Refer to Appendix E for additional details.

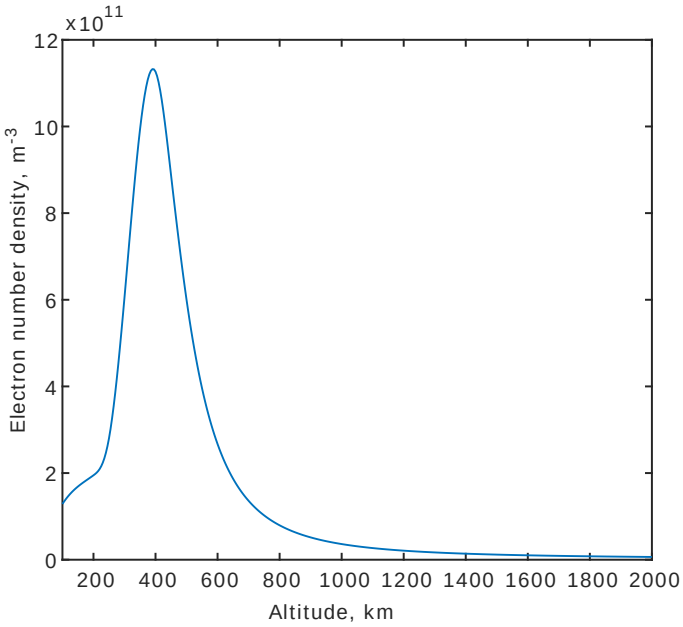

Figure 1.9: *Electron Number Density with respect to the orbital altitude, for average solar activity.*

The current is variable along the tether, and so the Lorentz force acting on every segment of it: this is a distributed pressure force which results in a resultant drag force acting on a point along the tether called *electrodynamic center of pressure*.

The tether must be made of conductive material: the higher is the conductivity, the higher is the current and the deorbit performance (i.e. lower deorbit times). Higher lengths of tether would also improve the deorbit performance, but they would lead to an increase in risk of tether being severed and higher mass to be carried onboard. An optimal compromise must then be found between cost of implementation, risk and performance. The electrodynamic tether can be deployed one-way, or be subdivided in two segments, following the so-called *butterfly* configuration, that are deployed along opposite directions.

In every BET system, a tip-mass must be attached to the free end of the tether: this mass is needed for tether stability over time, and for deployment control. The tip-mass can be made of components that are necessary for the functioning of the deorbit system, such as a hollow cathode for emitting electrons, after running along the tether, back to space. The tether is reeled and stored in a dedicated box until the start of deployment.

A great advantage of the BET system is that it is essentially *passive*, i.e. it requires no added energy in order to perform the deorbit. A very low amount of energy, might be required only in the first stages of deployment, that is performed and controlled with the aid of a small electrical motor. In fact, at the beginning of deployment, when a too short segment of tether is deployed, the generated current is too low: therefore, it may be necessary to use an auxiliary source of energy, possibly provided by a small

primary battery. Afterwards, the current flowing along the tether can be exploited, as it reaches the deployer, for providing the necessary amount of power, a part of which is used by the hollow cathode (refer to Sec.1.4.2 for description of cathode).

A BET system does not generally need an active attitude control during deorbit, i.e. after the tether is completely deployed. This is an advantage over a deorbit system based on *electrical propulsion*, for example. In fact, BET system must be designed in order to reach a self-stabilized condition during deorbit: this is achieved with different strategies, depending on the initial orbit of the object. For deorbit from LEO, the tether tends to librate around the system's center of mass: the highest performance is reached by keeping the tether as vertically aligned as possible. *Gravity gradient stabilization* can be used for longer tethers, also thanks to the presence of a tip-mass at the end. Another investigated solution is the use of passive viscous oscillation dampers applied at the tether's end attached to the body to deorbit (Ref. [24]). The use of an inert segment of tether, in series to the conductive segment, is another feasible way to increase stability (Ref.[52]).
For deorbit from high eccentricity orbits, where a tethered system naturally undergoes full rotations around its center of mass, a stable configuration can be achieved thanks to the centrifugal force created by the rotation. The positive tension created as a consequence along the tether keeps it straight and taut throughout deorbit, with the whole tethered system rotating around its center of mass, and moving along the deorbit path, approximately as a single rigid body.

1.4.1 Short historical review of tethered missions

20 sub-orbital and orbital flights have been made with tethered systems. Among all these missions, 8 of them used an electrodynamic tether. The table below summarizes all tethered missions, providing some essential information.

Mission	Date	Orbit	Tether Length	Additional Details
Gemini 11	1967	LEO	30 m	Spin Stabilized (0.15 rpm)
Gemini 12	1967	LEO	30 m	Gravity Gradient Stabilized, local vertical, stable swing
H-9M-69 [a]	1980	Sub-Orbital	500 m	Partial Deployment
S-520-2 [a]	1981	Sub-Orbital	500 m	Partial Deployment
Charge-1 [a]	1983	Sub-Orbital	500 m	Full Deployment
Charge-2 [a]	1984	Sub-Orbital	500 m	Full Deployment
Echo-7	1988	Sub-Orbital	–	Magnetic Field Alignment
Oedipus-A	1989	Sub-Orbital	958 m	Spin Stabilized (0.7 rpm), Magnetic Field Aligned
Charge-2B [a]	1992	Sub-Orbital	500 m	Full Deployment
TSS-1 [a]	1992	LEO	20 km, only 260 m deployed	Partially Deployed, Retrieved
SEDS-1	1993	LEO	20 km	Downward full deployment, swing and cut
PMG [a]	1993	LEO	500 m	Conductive, Upward Deployment
SEDS-2	1994	LEO	20 km	Downward full deployment, local vertical stabilized
Oedipus-C	1995	Sub-Orbital	1 km	Spin Stabilized (0.7 rpm), magnetic field aligned
TSS-1R [a]	1996	LEO	19.6 km	Close to full deployment, severed after 4 days by arcing
TiPS	1996	LEO	4 km	At 1022 km/63° since 1996, longest life tether on orbit (survived 12 years)
ATEx	1999	LEO	6 km	Partial deployment
ProSEDS [a]	2003	LEO	15 km	Hardware Built but not flown
MAST	2007	LEO	1 km	Did not deploy
YES2	2007	LEO	30 + km	Full deployment

[a] Electrodynamic Tether (EDT) Mission

Table 1.1: *Table reporting all tethered satellite missions to date.* Data from Ref.[40], [21].

1.4.2 Components of BET Deorbit System

Tether

References [40] and [11] propose a tape-shaped Bare Electrodynamic Tether as effective solution for deorbit. Typically, a tape tether would have a width of about 2–3 cm and a thickness of approximately 50–100 μm. The reason of this specific geometry is that it minimizes the risk of the tether being severed by impacts with meteoroids or other debris. Moreover, such typical sizes for the cross-section, that is constant along the tether length, allow to model the electron collection, from ambient plasma, with the *Orbital Motion Limited (OML)* theory (Ref.[10]).

Figure 1.10: *Image of Aluminum Tape Tether. Courtesy of* Tether Applications Inc.

The tether must be made of a conductive material. Previous studies propose Aluminum as base material: for example, **Al 1100-H19**, an Aluminum alloy made of 99% of Aluminum, plus very low percentages of other metals, including Copper (Cu). The presence of Copper enhances the electrical conductivity of the tether. Aluminum, used as main material, leads to higher thermal and mechanical resistance, and at the same time has a much lower density than Copper. Keeping the material density as low as possible is important, since the tether must have a low mass. The selected material then comes from a trade-off between electrical, mechanical and thermal properties, and density.

A crucial aspect is the tether being *bare*: there is no insulating outer layer wrapping the tether. This feature is chosen in order to maximize the electron collection from ambient plasma, as reported in Ref.[3]. In fact, a *bare* tether reaches the highest electrical contact with surrounding plasma. The former solution was to have an insulated tether, equipped with a conductive sphere, at one end, working as electron collection anode. Conversely, with a Bare Electrodynamic Tether, the tether itself works as a positively polarized anode attracting electrons from ambient plasma: this occurs all along the so-called *anodic segment* of tether. The number of collected electrons, and as consequence the electrical current, they are much higher with a bare tether, due to the much larger collecting area with respect to having a small collector only at the

tether's end. A higher current leads to a higher Lorentz drag force: therefore, the deorbit time is lower. Moreover, having a *bare* tether allows to save mass, since only a cathodic emitter is necessary, not also an anodic collector, given that its function is performed by the tether itself. Only a tiny segment of tether closest to the object to deorbit, where the tether is attached, might need insulation, in order to prevent electrical arcing.

While the largest portion of tether is positively charged, and collects electrons from space, there is a small segment of bare tether that is negatively charged. This segment works then as a cathode, emitting electrons: however, since the cathodic portion of tether is much shorter than the anodic one, a dedicated cathode is necessary to expel all the electrons back to space. This component is described in 1.4.2.

Cathode

A dedicated cathode is placed at the end of the tether attached to the object to deorbit, or as part of one tip-mass in case the *butterfly* configuration is used (refer to Sec.2.2 for description of this configuration). The cathode is a component that maximizes the electrical contact with space plasma, enabling a regular and continuous ejection back to space of the electrons flowing from the anodic part of the tether towards the cathodic end. Just before the cathode, an additional load can be inserted if it is necessary to use electrical current to power any active device. The cathodic emitter that has been most largely used and tested during tethered missions, is the *Xenon hollow cathode*.

This *hollow cathode* expels electrons through gas ionization: Xenon is widely preferred for its low specific ionization energy. The ionization generates a high density plasma plume, where the electron density is approximately equal to the ion density. However, the much higher electron velocities lead to electron currents much greater than Xenon ion currents: thus, for each ion leaving the cathode an incredibly higher number of electrons is expelled. The cathode requires a voltage bias of tens of volts only, determining a negligible contact impedance.

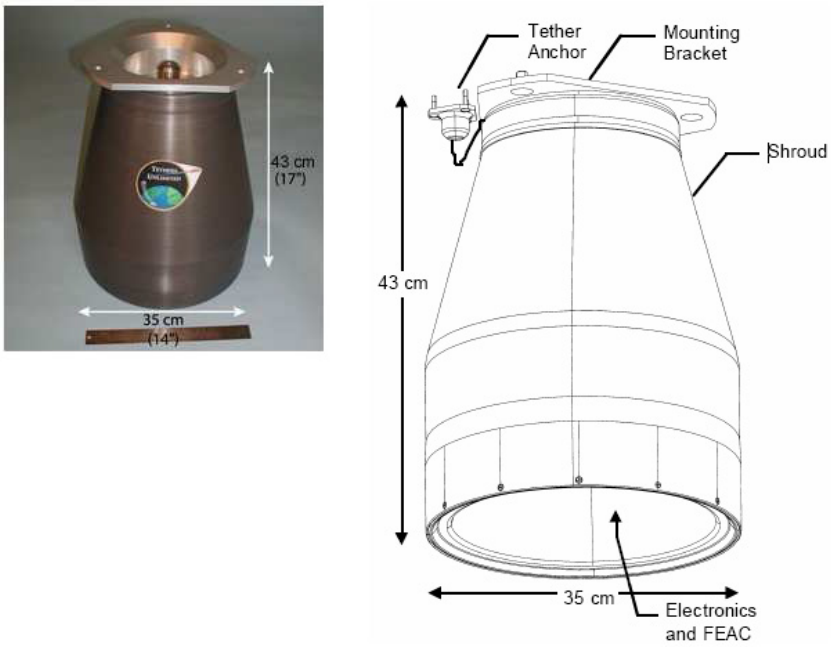

Figure 1.11: *Photograph and schematic view of cathode for EDT by* Tethers Unlimited^{TM}. *Courtesy of* Tethers Unlimited^{TM}.

The Xenon mass flow rate, and related cathode size, depend on current intensity. This means that the cathode is chosen accordingly to the maximum current expected during deorbit.

New technologies for cathodic emitters that do not require ionization gas are under study.
One of the most promising technologies, is the *Field Emitter Array Cathode (FEAC)*: essentially, it is a grid with millions of miniature low-biased tips that individually expel a tiny electron current (on the order of micro-ampere). The collection of all these tips creates a total current emission of the order of amperes. The larger is the array, the higher is the maximum current that can be expelled. Recently, important steps forward have been done with FEACs, ensuring compliance with requisites dictated by the harsh space environment, such as capability of working in vacuum and strong thermal resistance. A major issue presently under analysis is the capability of working efficiently even after contamination of the array tips (or, as alternative, ways to prevent contamination). In fact, contamination, e.g. due to outgassing phenomena, affects significantly the performance of this emitter. More details about the FEAC can be found at Ref.[29].
Another promising solution is to have a *Bare Thermionic Tether* (Ref. [50]), i.e. to have the cathode embedded in the part of tether as a *thermionic* coating (Ref. [12]), using *low-work-function* materials. One problem with this new technology, under investigation, is the degradation in space of the thermionic coating over time, and consequent decrease in performance.

1.4.3 Physics of Electrodynamic Drag force generation

Considering a segment of straight bare tether, and the axis x on the direction perpendicular to the tether, pointing from the tether's surface towards the surrounding plasma. Two simultaneous phenomena are responsible for the current generation along the tether:

1. *Potential Bias*: the difference of electrical potential along x direction, i.e. the difference of electrical potential between the surrounding plasma and tether, at every point along the tether's length. The electrical potential shows a variation along x only inside a thin region called *sheath*, that is a layer surrounding the tether with thickness of the order of a *Debye length*. Outside the *sheath* the plasma is globally neutral, whereas inside the *sheath* it is non neutral (Ref.[9]). This difference of potential, at every point along the tether, enables the electrons collection from ambient plasma to the tether. Electrons are collected by the tether, i.e. they move from surrounding plasma to the tether, at every point where the plasma potential is lower than the tether potential, i.e. in the *anodic* part of the tether. However, in a very limited portion of tether, i.e. the cathodic segment, the plasma potential becomes higher than the tether potential. Consequently, electrons are expelled towards space instead of being collected.
   The potential outside the *sheath* ($x > x_{sheath}$) is equal to the plasma potential, i.e. $V(x > x_{sheath}) = V_{pl}$. At each point on the tether's surface ($x = 0$) the potential is $V(x = 0) = V_t$. At the generic x location between the tether and the sheath boundary, the potential is $V(x)$.

$$\Delta V(x) = V(x) - V_{pl} \tag{1.1}$$

$$\lim_{x \to 0} \Delta V(x) = V_t - V_{pl} = \Delta V \tag{1.2}$$

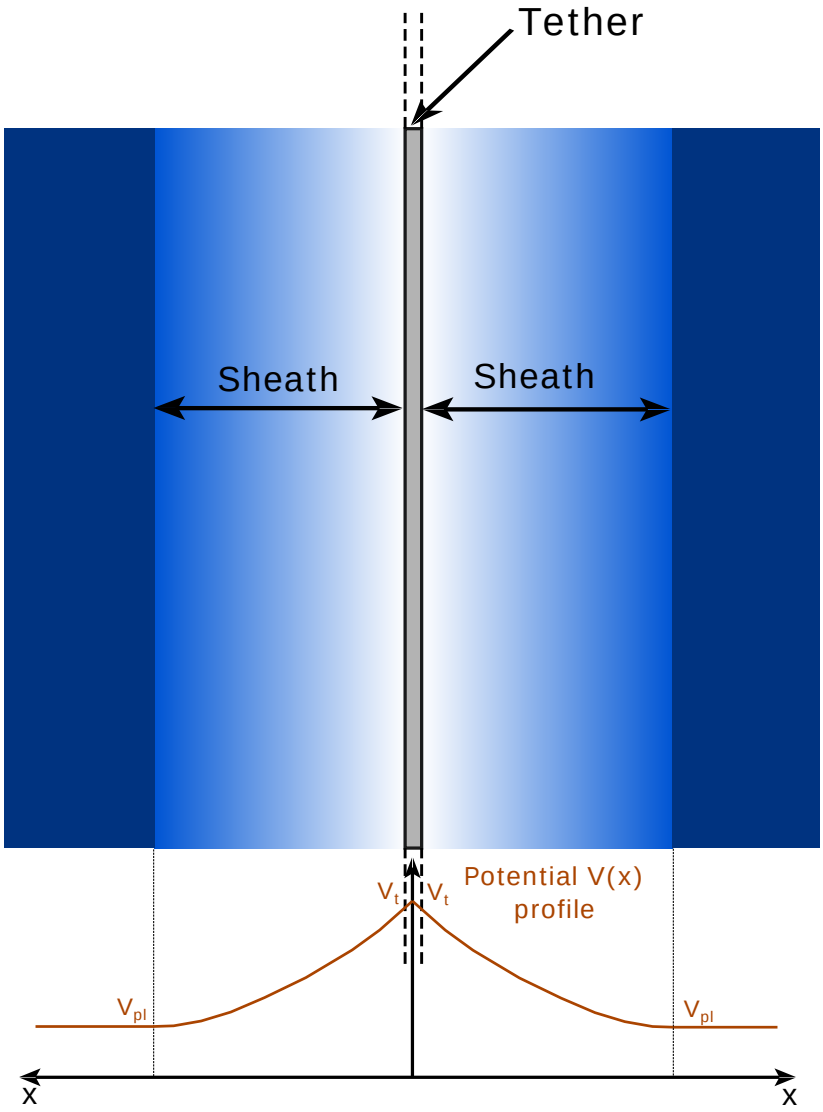

Figure 1.12: *Sketch of plasma* sheath *surrounding the tether, with electrical potential variation profile along the x direction*

2. *Difference of electrical potential along the tether.* The relative motion of the tether with respect to the geomagnetic field determines the generation of an induced electrical field $\boldsymbol{E}$ pointing along each segment of tether. The velocity of the system's center of mass is generally much larger than the relative velocity of tether with respect to the center of mass: consequently, it is assumed in calculations to have a linear velocity of the tether equal to the orbital velocity of system's center of mass $\boldsymbol{v}_t = \boldsymbol{v}_G$. The geomagnetic field can be reasonably assumed to be co-rotating with the Earth. With this assumption, the magnitude of linear velocity of the magnetic field, $\boldsymbol{v}_B$, at a specific orbital altitude h and orbital inclination i, can be computed as:

$$v_B = \Omega_E(R_E + h)sin(\frac{\pi}{2} - i) \tag{1.3}$$

where $\boldsymbol{\Omega}_E$ is the spin angular velocity of the Earth.

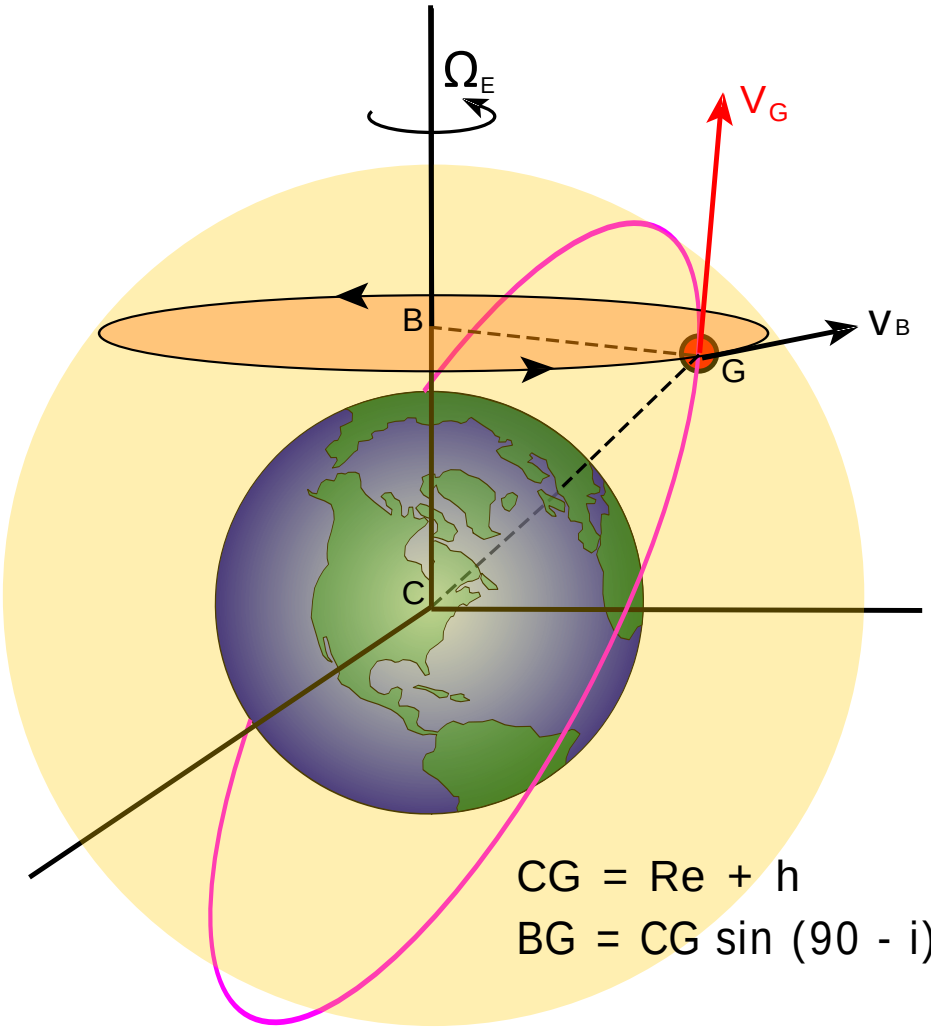

Figure 1.13: *Sketch showing the orbital velocity $\boldsymbol{v}_G$ of the system's center of mass (generally assumed equal to the tether's linear velocity) and the linear velocity of the geomagnetic field $\boldsymbol{v}_B$, at a generic point in space.*

The electrical field created along each segment of tether is computed as:

$$\boldsymbol{E} = \boldsymbol{v}_{rel} \times \boldsymbol{B} \tag{1.4}$$

where $\boldsymbol{v}_{rel} = \boldsymbol{v}_t - \boldsymbol{v}_B$ and $\boldsymbol{B}$ is the local magnetic field vector. The component of $\boldsymbol{E}$ projected along the tether is responsible of the creation of a variable potential $V_t(s)$ along the tether's length, i.e. along the parametric direction s.

The total difference of potential between the anodic and cathodic ends of the tether, $\Delta V_{t,TOT} = V_{t,A} - V_{t,C}$, is calculated as:

$$\Delta V_{t,TOT} = \int_0^L \boldsymbol{E} \cdot \hat{\boldsymbol{u}}_s ds = \int_0^L E_t ds \tag{1.5}$$

where E_t is the component of the electrical field $\boldsymbol{E}$ projected along each segment of tether.

The combination of electron collection inside the tether from ambient plasma, and the variation of potential along the tether, triggers the generation of an electrical current $i(s)$. This current has a variable intensity along the tether (typical profiles are shown in Fig.1.14 and Fig.1.15). The electron current flows in the direction opposite to $\boldsymbol{E}_t$, whereas the positive conventional current flows in the same direction as $\boldsymbol{E}_t$.

The local bias between plasma potential outside the sheath and the potential of the tether, $\Delta V = V_t - V_{pl}$, varies along the tether depending on the profiles of V_t and V_{pl}. Representative profiles, based on the study described in Ref. [10], are posted in Fig.1.14 and 1.15.

The plasma potential V_{pl} is initially lower than tether potential, and then it constantly increases along s. It intersects the V_t profile at zero bias point B, where $V_{pl} = V_t$ and $\Delta V = 0$. At last, it becomes higher than V_t in the short cathodic portion of tether.

The electrical current profile is shown too: it increases from zero, at the anodic end A, to a maximum value at the zero-bias point, and then it slightly decreases, due to a small ejection of electrons in the short cathodic segment.

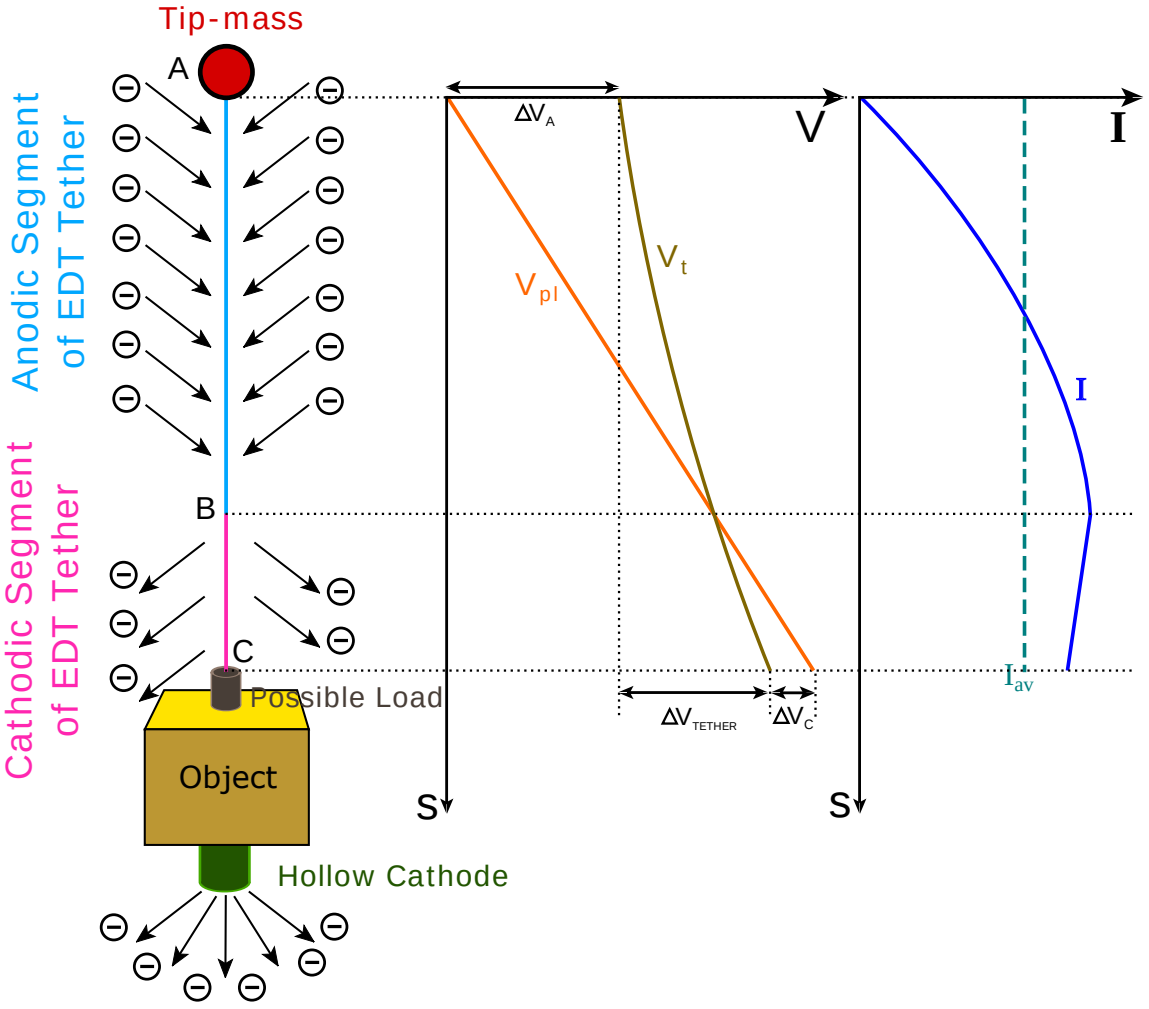

Figure 1.14: *Sketch of potential profiles and current profile along the Bare Electrodynamic Tether, for* prograde *orbits in LEO, for which the tether must be deployed upwards (i.e. away from the Earth's center). Instead, in high eccentricity orbits, the tethered system naturally rotates, therefore the direction of deployment is not relevant. In case the* butterfly *configuration is used, as described in Sec.2.2, the profile is the same but translated, and the cathode is mounted on one of the two tip-masses, not on the object to deorbit.*

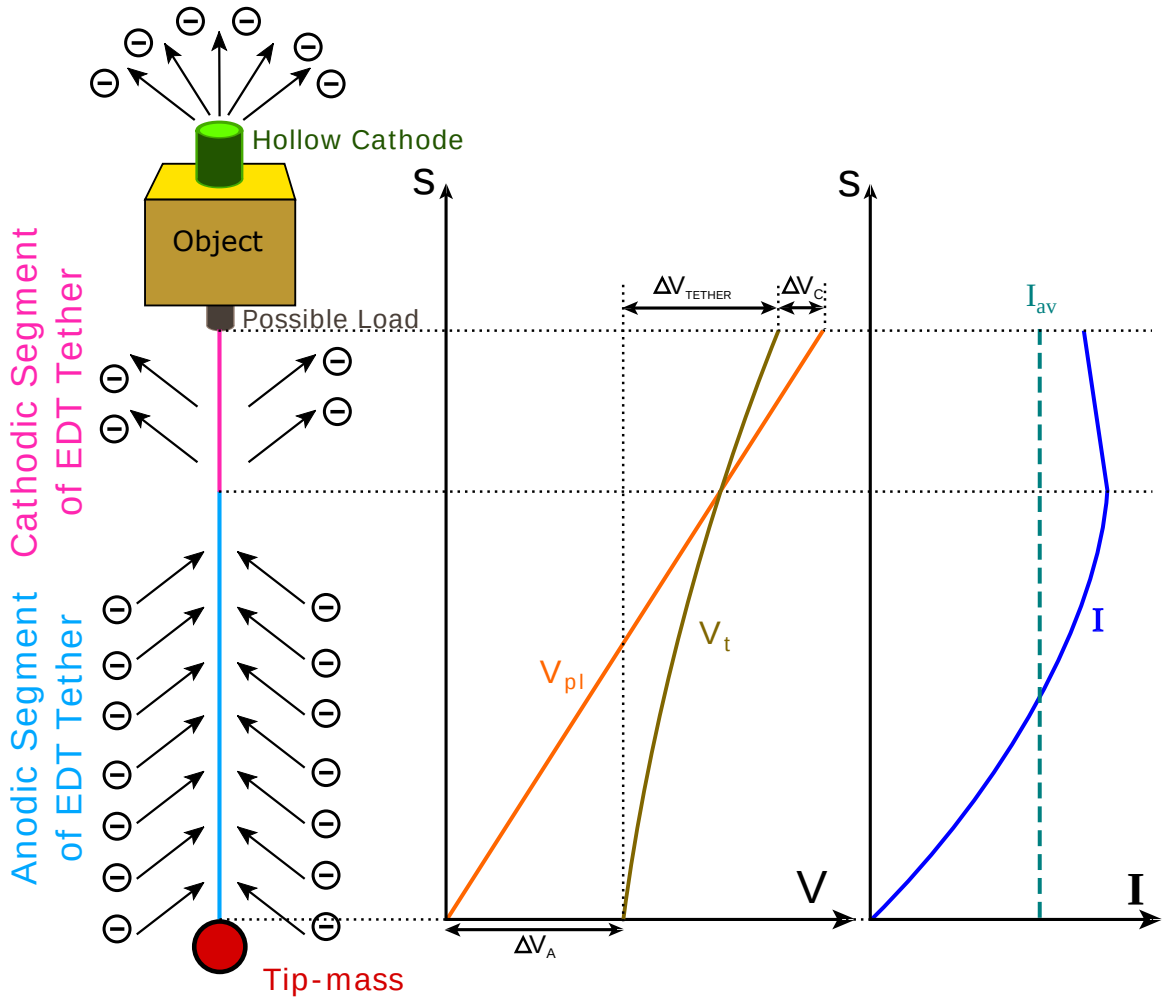

Figure 1.15: *Sketch of potential profiles and current profile along the Bare Electrodynamic Tether, for* retrograde *orbits in LEO, for which the tether must be deployed downwards (i.e. towards the Earth's center). Instead, in high eccentricity orbits, the tethered system naturally rotates, therefore the direction of deployment is not relevant. In case the* butterfly *configuration is used, as described in Sec.2.2, the profile is the same but translated, and the cathode is mounted on one of the two tip-masses, not on the object to deorbit.*

Electrons naturally flow from regions of lower electrical potential to regions of higher electrical potential. This is the reason why they are collected by the tether from ambient plasma only in the anodic segment of tether, where $V_t > V_{pl}$. Every infinitesimal segment of the anodic part of the tether collects a certain amount of electrons. The amount of electrons depends on the local value of bias ΔV, variable along s. At the zero-bias point electrons are not collected since $V_{pl} = V_t$. Lastly, in the cathodic segment, the tether potential is lower than plasma potential, so electrons are released by the tether towards space.

The fact that electrons flow from lower to higher electrical potential regions also explains why, after being collected by the tether, electrons move, generating a current,

from the anodic end A to the cathodic end C, given that $V_{t,C} > V_{t,A}$. Some literature references employ the *conventional current*, defined considering positive charges, that move opposite to the electrons flow. Consequently, the *conventional current* flows from the cathode towards the anode. The present research employs the electron current, not the conventional current (as displayed in Fig. Fig.1.14,1.15).

The current flowing through every infinitesimal segment ds of the tether interacts with the geomagnetic field, creating infinitesimal Lorentz forces acting on each segment ds. The integration over the entire tether length of these infinitesimal contributions gives the total Lorentz force acting on the system. This force is created only when the tether orientation in space is such that the electrical field $\boldsymbol{E}_t$ is positive, i.e. going from the cathodic end towards the anodic end. This is in fact the only condition in which an electrical current can be passively generated. It turns out, that for a passive BET system, the resulting Lorentz force is always a drag force, i.e. pointing opposite to the orbital motion. The Lorentz force $\boldsymbol{F}_L$ is then calculated as:

$$\boldsymbol{F}_L = \int i(s) d\vec{s} \times \boldsymbol{B}(s) \tag{1.6}$$

Both the current $i(s)$ and the magnetic field $\boldsymbol{B}(s)$ vary along the tether. The variation of geomagnetic field $\boldsymbol{B}$ is surely low on the typical length of BET tethers (on the order of 2 km as maximum). Hence, it is generally reasonable to assume $\boldsymbol{B}$ constant along the tether. Conversely, the current $i(s)$ varies significantly along the tether, given that, traveling from one end to the other, there is a continuous addition of new electrons collected from plasma by subsequent segments of tether. In the analyses presented in this thesis it is always assumed to have a straight tether and a value of current i_{av} is employed, averaged along the entire tether's length L_t. With these considerations, the integral in Eq.[1.4.3] can be reduced to:

$$\boldsymbol{F}_L = i_{av} L_t \hat{\boldsymbol{u}}_t \times \boldsymbol{B} \tag{1.7}$$

where $\hat{\boldsymbol{u}}_t$ is the unit vector of the tether direction. i_{av} depends on several parameters, such as plasma density and geometry of the tether. In metallic tethers, like the ones considered in this research, only electrons, not ions, are collected from space plasma. Thus, only the electron density N_e is needed for computations.

The distributed action of the Lorentz force creates a moment acting on the tether, that is equivalent to having the total Lorentz force acting on a specific point along the tether called *Electrodynamic Center of Pressure (ECP).*

Fig.1.14 and Fig.1.15 show the fact that when deorbiting from LEO, and using a configuration with a single eletrodynamic tether, the tether must be deployed upwards in case of prograde orbits, and downwards in case of retrograde orbits. This is due to the fact that in LEO a tethered system naturally librates, without experiencing full

rotations as happens in GTO or other high eccentricity orbits. It is then convenient to deploy in the direction such that a positive electrical field is generated along the tether, and then a drag Lorentz force is created. In case of deorbit from GTO, this is not applicable, and what happens is that during part of the rotation when the electrical field is negative, a current cannot flow along the tether, and a Lorentz force is then not generated. This is accounted in the codes presented in Chapter 2.

1.4.4 ED Tether System configuration

The peak of tether's current is reached at the *zero-bias point* B, i.e. the point along the tether where the potential bias between the tether and the ambient plasma is zero. This point generally lies very close to the cathodic end. This means that the segment of tether in proximity of the cathode is the part where the most of the distributed Lorentz drag force is concentrated.

Given that, as previously stated, the highest contribution of the Lorentz force is generated close to the cathode, this means that the Electrodynamic Center of Pressure (ECP) too will be much closer to the cathode than to the anode. In order to achieve the highest stability, and ensure resistance, of the tether, it is fundamental to have the ECP as close as possible to the system's center of mass G. In fact, the farther is the ECP from the system's center of mass, the higher is the *electrodynamic force moment*, since there would be a larger moment arm. This condition would excessively increase the rotation of the tethered system in high eccentricity orbit, as discussed in Sec. 2.1.3, leading to higher risk of tether breaking due to an excessive tension along the tether.

In order to have the ECP as close as possible to the system's center of mass, two strategies are applicable:

- In case of deorbit from LEO, where the tethered system librates without fully rotating, or anyhow in any case of single tether deployed one-way, the cathode must be mounted on the object to deorbit. The object to deorbit is generally more or much more massive than the tip-mass, and the tethers are of the order of 2 km as maximum length. As a consequence, the *system's center of mass* is generally located much closer to the object to deorbit than to the tip-mass. If the cathode were placed at the free end, together with the tip-mass, the ECP would then be very close to the tip-mass, and very far from the system's center of mass, that is instead very close to the object to deorbit. Such configuration would then surely lead to stability problems. Consequently, improving the stability of the system is the first reason why the cathode must be attached to the object to deorbit, as shown in Fig.1.14 and 1.15. Moreover, having the cathode attached to the object to deorbit allows to employ the current arriving from the tether. For example, power can be supplied to the small electrical motor used for tether deployment, after a long enough portion of tether is already deployed and generating enough current.

- In case of deorbit from LEO, a proposed strategy to have the ECP as close as possible to the system's center of mass, it is to use an *inert (non-conductive)* segment of tether attached in sequence to the conductive segment (Ref.[52]). The inert segment will then have the tip-mass attached at its end. Such configuration, with inert tether too, is displayed in Fig. 1.16. In fact, the addition of an inert segment, after the conductive one, affects the location of the system's center of mass, moving it a farther from the object to deorbit, and then closer to the ECP. The system's center of mass is generally much closer to the object to deorbit than it is the ECP. Low density materials, like *Kevlar*®, could be used for the inert tether segment (density of about $1440\,\mathrm{kg/m^3}$, and the length of the inert segment would be small compared to the conductive segment. Hence, using an inert tether would lead to only a small mass increase.
- The optimal strategy, in case of deorbit from high eccentricity orbits with fully rotating tethered system, it is to use the so-called *butterfly* configuration. This configuration is thoroughly described in Sec.2.2. The fact that this is the optimal choice in case of deorbit from high eccentricity orbits, such as Sylda from GTO, is demonstrated in the analysis presented in Sec. 2.1.3. Implementing the butterfly configuration means to have a single electrodynamic tether subdivided in two electrically connected segments, that are deployed along opposite directions from the object to deorbit, i.e. Sylda in this case. Each segment has a tip-mass mounted at its free end. The two segments have different lengths, and these lengths are selected in order to minimize the gap between the ECP and the system's center of mass. It is important to note that the ECP always changes over time during deorbit, oscillating inside a certain range along the tether. Consequently, the distance with respect to the center of mass is generally never zero, but it can be minimized. The present research investigates specifically the use of this *butterfly* configuration, instead of having an additional inert segment of tether, that does not contribute to current generation, and that would lead to an undesirable mass increase of the system. In case of butterfly configuration, there is a tip-mass at the free end of each of the two tether segments: thus, there are two tip-masses in total. One tip-mass must include the cathodic emitter, and the other tip-mass should possibly include other components that are needed by the deorbit system, in order not to be entirely a ballast mass. These tip-masses should be typically on the order of maximum 5 kg for an object to deorbit of mass around 500 kg, as in case of Sylda.

1.4.5 Motion of a tethered system in space

In low eccentricity orbits, such as LEO orbits, the tether generally oscillates around an equilibrium position, in a certain angular range: this motion is called *libration*, and it takes place both on the orbital plane and out of it. In deorbit procedures from LEO, as described in Ref.[40], the desired configuration is to have the tether as aligned as possible with the local vertical, or anyhow librating with a small angle with respect to the local vertical. In order to have an electrical field along the tether in the direction such that a Lorentz drag force is generated, and at the same time the cathode attached to the body to deorbit (for the reasons explained in Sec.1.4.4), the

deployment must be performed with the tip-mass pointing upwards in case of prograde orbits, and downwards in case of retrograde orbits. More precisely, as from Ref.[31], the deployment must be pointing upwards for initial LEO orbits of inclination i from zero to approximately 78.5°, considering a dipole model for the geomagnetic field; for *retrograde* orbits, with $101.5° < i < 180°$, a downwards deployment is required. For inclinations $78.5° < i < 101.5°$ an analysis must be performed to estimate what is the most favorable direction for deployment, i.e. the one that maximizes the Lorentz drag force over the entire deorbit.

Figure 1.16 shows both the prograde and retrograde configurations. Some simplifications are present in the pictures, such as magnetic field orthogonal to both the relative velocity vector and the tether: this is of course not true in general. The placement of the cathode here is just representative: the cathode is surely attached to the body to deorbit, but the exact placement is not discussed here and not shown in the pictures.

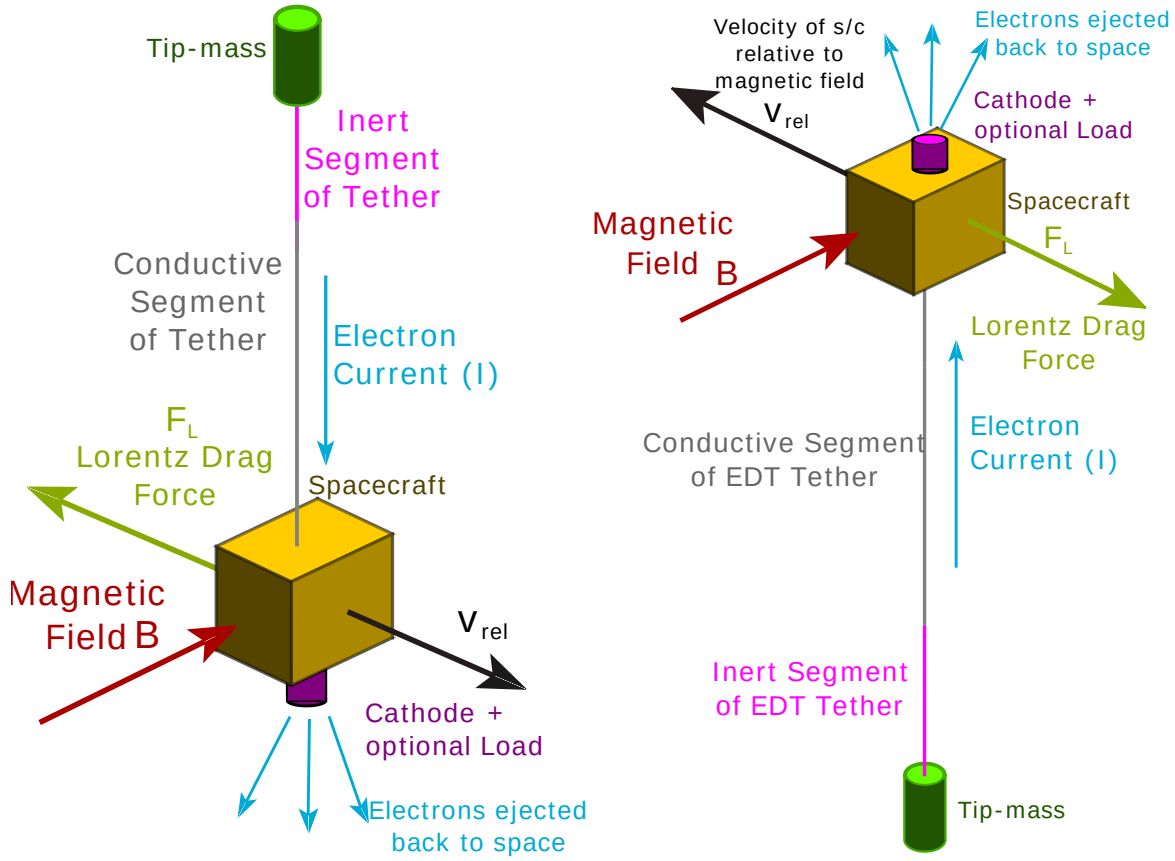

Figure 1.16: *BET system for deorbit from LEO. On the left: case of* prograde *orbits. On the right: case of* retrograde *orbits.*

A stable nadir alignment of the tethered system cannot be naturally achieved (i.e. without passive or active control) along any eccentric orbit. Moreover, this nadir pointing stability becomes increasingly challenging with increasing eccentricity.

Instead, in the case studied in this PhD research, i.e. deorbit from high eccentricity

initial orbits, the motion of any tethered system is different than the motion of the same system in LEO.
As reported in Ref. [44], tethered systems in orbits with eccentricity higher than about 0.355, as in case of Sylda that is left in GTO, an unconstrained tethered system would fully rotate around its center of mass. In this case, it is not convenient to seek the vertical alignment of the tether. The optimal stabilization strategy is different: in fact, the centrifugal force created by the rotation of the tethered system can be exploited in order to maintain a straight, taut and stable, configuration of the tether. However, the rotation must be passively controlled with an optimal design of the system: in fact, an uncontrolled rotation, if increasing too much, it would lead to an excessively high tension along the tether, and eventually to tether breaking. Hence, the tension, and consequently the rotational velocity, must be kept below a maximum threshold. This limit is dictated by the mechanical properties of the tether material. These aspects are discussed in Sec.2.1.3 of this thesis.

1.5 Objectives of PhD research

This PhD research has its general objective in expanding the knowledge about the dynamics of a Bare-Electrodynamic-Tether (BET) system attached to an object in high eccentricity orbit, throughout all the stages to remove it from orbit: a procedure called *deorbit*. The electrodynamic tether considered in all the analyses has a tape-like shape, and it is equipped with a hollow cathode for electron emission.
A major driver in the selection of the optimal deorbit device is its cost. Deorbit is not regarded as a scientifically or commercially pay-back measure, even if crucial for the safety of the space environment. Consequently, the cost of deorbit, and the mass of the deorbit system, must be minimum.
Bare Electrodynamic Tethers have this potential, and they can also be implemented on objects where other solutions are not applicable, such as dual-payload adapters, i.e. bell-shaped structures used inside the fairing of a launch system in order to provide housing for two separate payload units: a deorbit system based on chemical propellant, for example, would be hardly acceptable to be mounted outside such structures, in proximity of the fairing walls, due to the hazard that they would cause during the launch phase. The technology of electrodynamic tethers has been tested in space, and proved to work successfully, such as in missions PMG (1993) and TSS-1R (1996): nonetheless, tethers have never been used for an actual deorbit application. Together with all the positive features that tethers can bring to deorbit applications, the issue is that tethers in space exhibit a more complex dynamics than alternative systems proposed in literature, such as mounting small thrusters based on chemical or electrical propulsion; a tethered system for deorbit requires then further research and acquisition of new know-how, that this research aims to provide.

The dual-payload adapter used onboard *Ariane 5* heavy launches to GEO, called *Sylda*, is chosen as practical target, due to its large exposed area and mass, that make it a major threat for active payloads both in LEO and GEO. In fact, Sylda is released in GTO in the last phase of insertion of the dual payload in GEO: from this GTO

orbit, Sylda continuously crosses both highly valuable zones of LEO and GEO. This research focuses on deorbit from high-eccentricity initial orbits, also because there is very little literature about it, even though it is of sure commercial interest, whereas deorbit from LEO has been widely studied in many scientific references. This research considers Sylda as specific target, but the results presented here are applicable with only slight modifications to other objects to be removed from any high eccentricity orbit: for example, inactive satellites in Molnija orbits.

A pivotal objective of this research is then the development of physical and numerical models to simulate all the phases required to remove Sylda from orbit: this means that not only the deorbit phase, with fully deployed tether is studied, but also the phase of deployment of the tether and other necessary pre-deorbit procedures. A system configuration is found from this research, that ensures compliance, by a large extent, with deorbit international guidelines (setting 25 years as maximum time for removal), while keeping the mass of the deorbit system as low as possible.

Another objective is to define an optimal system design, and boundary conditions, that ensure the tether stability and the avoidance of tether breaking throughout deorbit. In order to achieve this objective, two main configurations for the Bare Electrodynamic Tether system are explored:

- a first configuration with single BET tether deployed one-way, discussed in Sec.2.1
- a second configuration with a single BET tether, but subdivided in two segments, that are electrically connected, and deployed along two opposite directions from Sylda. This configuration, called *butterfly* configuration, is selected as the optimal one, after the results presented in Sec.2.1.3, and then used for all the subsequent analyses.

Lastly, the research also aims to study procedures to guarantee the correct deployment of the two tether segments in butterfly configuration, by detumbling Sylda before deployment starts, and by detecting and controlling the tethers attitude. In particular, for the attitude detection, a vision system is proposed and different configurations are analyzed, evaluating the uncertainty in the measure of the angular position and the distance of the tip-mass, at the end of each tether segment, from Sylda.

Based on numerical simulations of BET systems in space, a flexible deorbit architecture can be developed in the near future, in which BET systems can be easily tailored according to the specific target to remove from orbit. This PhD research is oriented towards this scenario, in which deorbit becomes a routine procedure, for any future object launched into Earth orbits.

The research is subdivided in three main branches, presented in separate Chapters of this dissertation:

- **Deorbit simulation from GTO**. In Chapter 2 all the deorbit analyses and

simulations are presented. This means that Chapter 2 deals with only what happens after the tether segments are fully deployed, and the deorbit procedure starts.

A first phase of analyses is performed with the principal aim of simulating with a fast computational model the deorbit phase, and to estimate the conditions to avoid tether breaking and instability. The model is created in a way such that it is employable both to study a single tether configuration, or the *butterfly* configuration, with two tether segments deployed on opposite directions from Sylda. This capability is given by the fact that the model is nondimensional, and receives among the inputs directly the location of the system's center of mass along the tether, without need of specifying the system's configuration. A nondimensional model with normalized parameters and equations is used, with the tethered system modeled as a rigid dumbbell, and including both the global orbital motion and the simultaneous local rotation around the system's center of mass. Only the local rotation on the orbital plane is considered, and perturbation forces are the Lorentz drag and atmospheric drag. The Lorentz drag, created by the BET tether, becomes significant only when the system is orbiting below 2000 km; the atmospheric drag only when below 1000 km. Tether stability during deorbit is studied: in case of rotating tethered systems, as happens in GTO, the tether can be maintained on a straight stable configuration by exploiting the centrifugal force generated by the rotation. An analysis on the maximum tension created along the tether is implemented too, in order to evaluate the conditions to avoid tether breaking during deorbit. Results from this first campaign of analyses provide information about the optimal configuration to choose for the BET system, leading to the employment of the *butterfly* configuration.

A second campaign of deorbit analyses is then performed, with the selected *butterfly* configuration for the BET system. For this campaign, the numerical model is expanded and made even more accurate, including also the out-of-plane dynamics of the system. The dumbbell model is preserved, or more precisely a *double-dumbbell* model, since there are now two segments of tether deployed on opposite directions. A *hybrid* numerical model is developed and used, i.e. a model including both nondimensional and dimensional equations and variables. This is done in order to combine the advantages and attenuate the disadvantages of both dimensional and nondimensional approaches.

- **Deployment of the two tether segments**. In Chapter 3 the study of tether deployment, adopting the *butterfly* configuration, is performed. The storage of the deorbit system and mounting on Sylda is discussed too, providing a solution of easy integration with the default design of the *Ariane 5* launcher equipped with Sylda. Three scenarios of deployment are modeled, starting at different locations along the initial GTO orbit of Sylda, where it is released: deorbit at apogee; deployment at perigee; deployment at mid-way, after leaving the perigee region going back towards the apogee. In Chapter 3, the detumbling of Sylda, a

necessary procedure to be performed before starting the deployment, is analyzed too.

- **Vision system for tether's attitude detection**. Chapter 4 presents an analysis of possible configurations of a vision system to detect the tether's attitude, by tracking the tip-mass at the end of each tether segment. A *monocular* and a *stereo* vision system are both considered, and their measurement performance is simulated numerically in order to estimate the uncertainty in the measured output. The application of a Kalman filter is discussed too, both with correlation and without correlation between the measures provided by two cameras used to track the same tip-mass. Results outline optimal solutions for the vision system, i.e. the configurations that minimize the uncertainty on the measure.

Lastly, Chapter 5 draws conclusive remarks from all the analyses performed in the previous Chapters.

An Appendix is inserted too, in order to provide expanded insights on the *nondimensional* model used in the analyses presented in Sec. 2.1, on the environmental parameters computation, and on the reference frames that are employed throughout this research.

Chapter 2

Analysis of Deorbit

This Chapter deals with the study of the deorbit of Sylda from its initial Geostationary Transfer Orbit (GTO)behavior, once the tether is completely deployed, taut and straight due to the rotation of the system around its center of mass. All the necessary steps to be performed before starting the deorbit, including the tether deployment, will be discussed in Chapter 3. A dumbbell model is reasonably assumed for the tethered system, since the tether and Sylda start, at the end of deployment, to approximately rotate together as a single rigid body as discussed in Chapter 3.

2.1 First phase of analysis

A first campaign of deorbit simulations is performed with these main features:

- Only dynamics on the orbital plane are considered, i.e. the out-of-plane motion of the system is neglected.
- A single tether is used and modeled as a dumbbell, i.e. the system has only one *local* degree of freedom that is the rotation on the orbital plane around the system's center of mass. At the same time, the system moves as a whole along the deorbit path. The dumbbell has two tip-masses, one at each end of the tether: one tip-mass includes Sylda, the hollow cathode for electron ejection, and other hardware of the deorbit system.
- A *nondimensional* model is used in order to achieve the maximum computational efficiency and flexibility, with all the parameters and equations normalized. This model is described in Sec. 2.1.1.
- The orbital inclination is kept constant throughout deorbit, and equal to zero. This is reasonable given that Sylda is released on a very low inclination GTO (about 6°) and that the inclination changes little during deorbit, as will be demonstrated in Sec.2.2.2 and shown in Fig. 2.13.

2.1.1 Nondimensional Physical Model

The first computational model developed for deorbit simulation relies upon the *nondimensional approach*, i.e. all variables and equations are made nondimensional in order to provide a very computationally efficient and flexible solution method. However, all the references to the dimensional form of the main equations is provided, and a table is posted in Appendix A, with the dimensional and corresponding nondimensional parameters used in the model, and coefficients to switch from one form to the other.

Two reference frames are used in the model:

1. *Orbital* frame, with unit vectors $\boldsymbol{u}_r$, $\boldsymbol{u}_s$, $\boldsymbol{u}_w$.
2. *Perifocal* frame, with unit vectors $\boldsymbol{u}_p$, $\boldsymbol{u}_q$, $\boldsymbol{u}_w$.

Refer to Appendix B for a description of these frames. The angular velocity of rotation of the orbital frame with respect to the perifocal frame is $\dot{\nu}\boldsymbol{u}_w$.

The system is modeled as a single dumbbell with two point masses at each end, i.e. m_A as anodic tip-mass and m_C as cathodic tip-mass. These two masses are connected by a conductive bare electrodynamic tape tether of mass m_t, width w_t, thickness h_t, and length L_t. The tether is assumed to be rigid and inextensible. This is an approximation, however it is realistic since with the rotation of the system, that starts during the deployment, the tether tend to a straight configuration with the increase of the angular velocity of rotation. Once reaching a straight configuration, since the rotation about the center of mass does not decrease during deorbit, the tethered system keeps rotating approximately as a single rigid body.

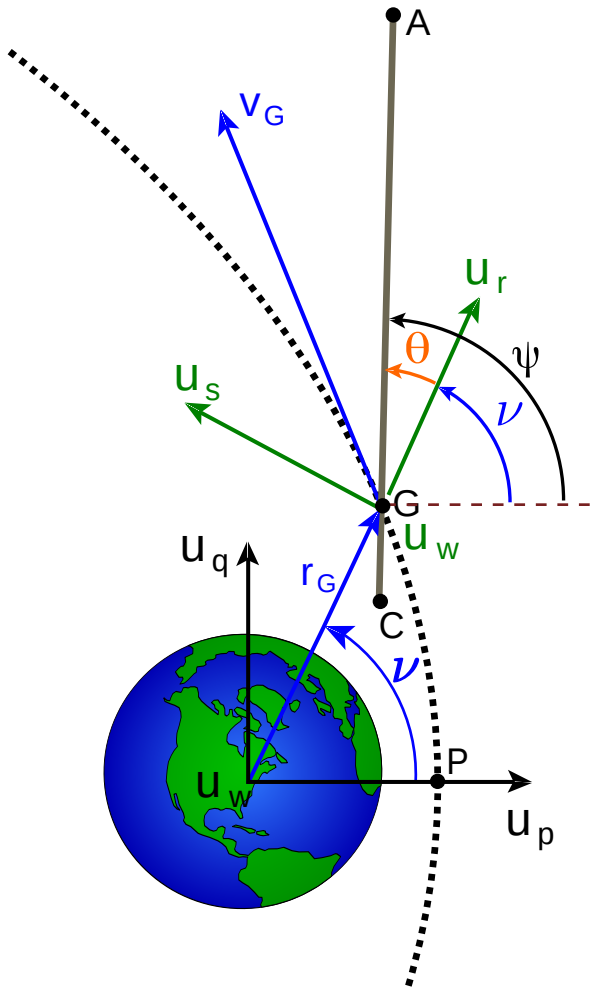

Figure 2.1: *BET deorbit system with angles of global and local motion. Point A and C are the anodic and cathodic ends where the masses are placed: Sylda is included in the mass at point C together with a hollow cathode mounted on it. Point G is the center of mass of the entire system. The system's center of mass G moves along the deorbit path (dashed black line), with position $\boldsymbol{r}_G$ and velocity $\boldsymbol{v}_G$. The angles of true anomaly ν, local tether in-plane rotation θ, and $\Psi = \nu + \theta$ are displayed too.*

The tether carries a current intensity $\boldsymbol{i} = i(x)\boldsymbol{u}_t$, where $\boldsymbol{u}_t$ is a unit vector directed along the tether and pointing from the cathodic point C, where Sylda and the hollow cathode are placed, towards the anodic point A. Similarly to what was done in other works (e.g. Ref.[35]), normalized variables are introduced, and distinguished from the corresponding dimensional variable with a bar on the top.

In this first campaign of analyses, the cathode is assumed to be mounted on Sylda, and the tether to be deployed one-way only: consequently, the mass m_C is made of Sylda's mass m_S plus the mass of anything that is mounted on Sylda, including the cathode. $m = m_A + m_C + m_t$ is the total mass of the system. The masses m_A and m_C are expressed as function of the total mass m and two nondimensional variables

$\overline{m}_t$ and ϕ, where:

$$\overline{m}_t = \frac{m_t}{m} \tag{2.1}$$

is the fraction between tether mass and total mass, and ϕ is such that:

$$m_A = m\left(\cos^2\phi - \frac{\overline{m}_t}{2}\right) \tag{2.2}$$

$$m_C = m\left(\sin^2\phi - \frac{\overline{m}_t}{2}\right) \tag{2.3}$$

The minimum and maximum value of ϕ are $\phi_{min} = arcsin\left(\sqrt{\overline{m}_t/2}\right)$ and $\phi_{max} = arccos\left(\sqrt{\overline{m}_t/2}\right)$, and they correspond to $m_C = 0$ and $m_A = 0$, respectively (as from Ref.[35]). The position vector of the center of mass G, with respect to point C is then:

$$\boldsymbol{x}_{CG} = L_t \cos^2\phi \boldsymbol{u}_t \tag{2.4}$$

and the moment of inertia of the system J^G, relative to a line orthogonal to the tether and passing through G, is computed as:

$$J^G = \frac{1}{12} m L_t^2 \left(3\sin^2 2\phi - 2\overline{m}_t\right) \tag{2.5}$$

The trajectory of the system's center of mass in the *perifocal* frame is defined using the Keplerian orbital parameters: the semi-major axis a, eccentricity e and the true anomaly ν are considered variable over time, whereas the other Keplerian parameters are assumed constant throughout the deorbit. The inclination, as previously stated, is assumed to be zero in all the analyses presented in Sec. 2.1: therefore, the equatorial plane is always coincident with the orbital plane.

The out-of-plane dynamics of the tether, as previously stated, are neglected: in other words, only the motion on the orbital plane is considered throughout the analyses presented in this Sec. 2.1. The in-plane *local* motion of the system around its center of mass is defined by the angle θ between $\boldsymbol{u}_r$ and $\boldsymbol{u}_t$.

The components in the orbital frame of the unit vector $\boldsymbol{u}_t$ are:

$$\boldsymbol{u}_t = \cos\theta \boldsymbol{u}_r + \sin\theta \boldsymbol{u}_s \tag{2.6}$$

The normalized position vector of the center of mass $\boldsymbol{r}_G$, and its velocity $\boldsymbol{v}_G$, expressed in orbital frame components, are defined as follows:

$$\bar{\boldsymbol{r}}_G = \frac{\boldsymbol{r}_G}{R_E} = \frac{\bar{a}(1-e^2)}{1+e\cos\nu}\boldsymbol{u}_r \tag{2.7}$$

$$\bar{\boldsymbol{v}}_G = \sqrt{\frac{R_E}{\mu_E}}\boldsymbol{v}_G = \frac{1}{\sqrt{\bar{a}(1-e^2)}}\left[e\sin\nu\ \boldsymbol{u}_r + (1+e\cos\nu)\,\boldsymbol{u}_s\right] \tag{2.8}$$

where the normalized velocity $\bar{\boldsymbol{v}}_G$ and radius vector $\bar{\boldsymbol{r}}_G$ of the center of mass are introduced, as well as the normalized semi-major axis $\bar{a} = a/R_E$. R_E and μ_E are the Earth radius and gravitational parameter, respectively.

The deorbit path (global motion) of the center of mass and the tether attitude over time are affected by the total perturbation force, $\boldsymbol{F}$, and the total moment $\boldsymbol{M}^G$ about the system's center of mass.
The global motion of the center of mass is analyzed using the Gauss planetary equations (Ref. [7]), written in nondimensional form as follows:

$$\dot{\bar{a}} = \frac{2\bar{a}^{3/2}}{\sqrt{1-e^2}}\left[\overline{F}_r e\sin\nu + \overline{F}_s\,(1+e\cos\nu)\right] \tag{2.9}$$

$$\dot{e} = \sqrt{\bar{a}(1-e^2)}\left[\overline{F}_r\sin\nu + \frac{2\cos\nu + e\,(1+\cos^2\nu)}{1+e\cos\nu}\overline{F}_s\right] \tag{2.10}$$

$$\dot{\nu} = \frac{\sqrt{\bar{a}(1-e^2)}}{\bar{r}_G^2} \tag{2.11}$$

The dots over each variable denote derivatives with respect to the normalized time $\tau \equiv t\sqrt{\frac{\mu_E}{R_E^3}}$.
The local rotation around G is studied with an equation derived from previous literature (Ref.[8, 45]), with slight modifications and normalized parameters:

$$\ddot{\Psi} = -\frac{3}{2r^3}\sin\left[2\,(\Psi-\nu)\right] + \overline{M}^G \tag{2.12}$$

where $\Psi = \theta + \nu$ is introduced for convenience. After finding the profile of Ψ and ν over time with Eqs.2.12,2.11, the profile of $\theta = \Psi - \nu$ can be found. Vector $\overline{\boldsymbol{F}} = \overline{F}_r\boldsymbol{u}_r + \overline{F}_s\boldsymbol{u}_s$ in Eqs. 2.9-2.10 is the total vector of perturbation forces, accounting for both aerodynamic drag and electrodynamic drag, and split in components on the orbital frame, and normalized as $\overline{\boldsymbol{F}} = \boldsymbol{F}R_E^2/(m\mu_E)$. The scalar $\overline{M}^G$ in Eq.2.12 is the projection on $\boldsymbol{u}_w$, i.e. on the perpendicular to the orbital plane, of the total torque exerted by the perturbation forces around the system's center of mass G, $\overline{M}^G = \left[R_E^3/(\mu_E I^G)\right]\boldsymbol{M}^G\cdot\boldsymbol{u}_w$.

The dominant perturbations for a BET system in GTO are the Lorentz electrodynamic force and the aerodynamic force. Both of them are drag forces, that dissipate orbital energy. The total perturbation force is then calculated as:

$$\boldsymbol{F} = i_{sc}L_t\overline{i_{av}}\,(\boldsymbol{u}_t\times\boldsymbol{B}) - \frac{1}{2}c_d\rho_{atm}Sv_G\boldsymbol{v}_G \tag{2.13}$$

where $i_{sc} = E_t \sigma_t w_t h_t$ is the short circuit current computed from the induced electrical field $E_t = \boldsymbol{u}_t \cdot (\boldsymbol{v}_G \times \boldsymbol{B})$; $\boldsymbol{B}$ is the geomagnetic field; $\overline{i_{av}}$ is the normalized average current along the tether; c_d is the aerodynamic drag coefficient; ρ_{atm} is the atmospheric density; S is the total area exposed to atmospheric drag of the entire system, projected on the plane orthogonal to the drag force. The Lorentz force is active only when $E_t > 0$. This is due to the fact that when the induced electrical field, during the local rotation of the system, becomes negative, i.e. pointing from anode to cathode, no current can be generated by the tether. Consequently, no Lorentz drag is created. The code implements this condition by automatically zeroing the current at every integration time-step when the electrical field component along the tether is negative.

The normalized average tether current, $\overline{i_{av}}$ in Eq. 2.13, is here computed assuming an *ideal* tether, i.e. a tether with both zero cathodic impedance and zero cathodic voltage drop. Moreover, the electron collection by the tether is assumed to take place under the *Orbital Motion Limited* (OML) theory [41]. This assumption is reasonable given the very low influence, on the overall electrodynamic behavior, of neglecting these two parameters (Ref. [3], [37]). As reported in Refs.[3] and [40], the normalized average current $\overline{i_{av}}$ depends only on the normalized tether length, defined as

$$\overline{L}_t = \frac{L_t}{h_t^{2/3}} \frac{1}{l^{1/3}}, \tag{2.14}$$

involving the tether length L_t, the tether thickness h_t, and the ambient-dependent parameter

$$l \equiv \frac{9\pi^2}{128} \frac{m_e \sigma_t^2}{q_e^3} \frac{E_t}{N^2} \tag{2.15}$$

where m_e, q_e, σ_t, and N_e are respectively the mass and charge of a single electron, the tether conductivity and the electron number density. The computation of $\overline{i_{av}}$ is performed with an algorithm partially derived from Ref.[38], and described in Sec. 2.1.1.

In this first part of analysis presented in Sec.2.1, the geomagnetic field is always computed, using the dipole model, as:

$$\boldsymbol{B} = \frac{B_0}{r^3} \boldsymbol{u}_w \tag{2.16}$$

where $B_0 = 3.12 \times 10^{-5} T$. The field is always directed along the unit vector $\boldsymbol{u}_w$ given that the deorbit simulation takes place on the equatorial plane and the magnetic field is a simple dipole. For inclinations different than zero, the geomagnetic field has other components too.

The *IRI* (International Reference Ionosphere) 2007 database from NASA is employed to extract data of ionospheric electron number density N_e (see Fig. 2.2, and Appendix

E). This specific model computed the values of N_e on a Julian Day such that the Solar activity was at approximately average level ($F10.7 \approx 145$ s.f.u.), and it only includes the variation with altitude (not with time, nor with latitude and longitude). For altitudes greater than 2000 km, N_e becomes negligible, and the Lorentz drag is then automatically zeroed by the code.

The atmospheric density, needed for the aerodynamic drag computation in Eq. 2.13, is extracted from the *Jacchia-Bowman 2008* empirical model, for a value of average Solar flux. The atmospheric density becomes negligible above 900 km, and the atmospheric drag is then set to zero above this altitude. More details are provided in Appendix C. The electron number density and atmospheric density profiles used in the simulations are posted in Fig. 2.2.

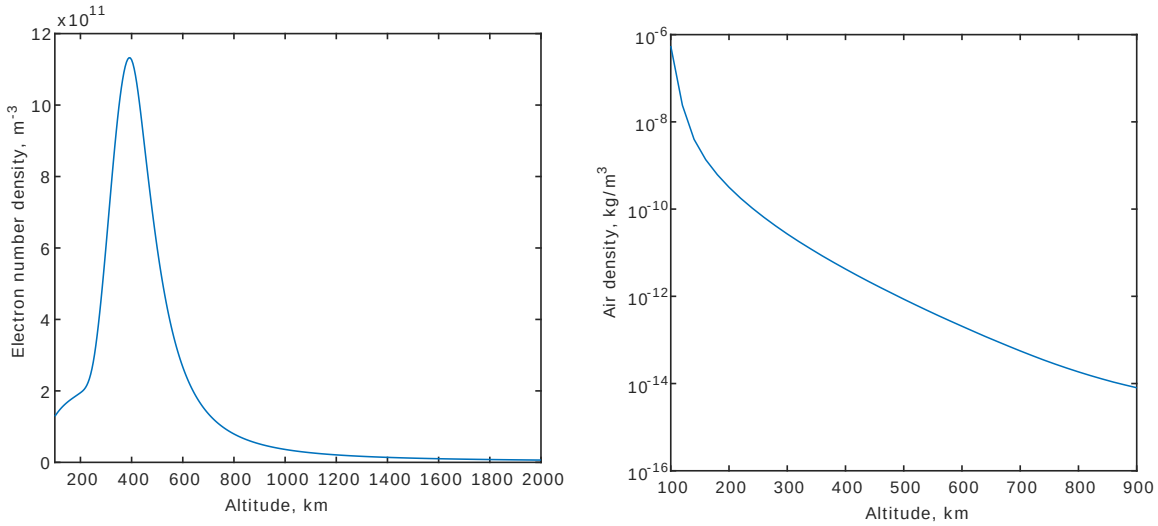

Figure 2.2: *Left: electron number density versus altitude. Right: atmospheric density versus altitude.*

The normalized perturbation force in Eqs. 2.9 and 2.10 is calculated as:

$$\overline{\boldsymbol{F}} = \alpha_L \overline{m}_t \frac{[\boldsymbol{u}_t \cdot (\bar{\boldsymbol{v}}_G \times \boldsymbol{u}_w)]}{\bar{r}_G^6} \overline{i_{av}} \, (\boldsymbol{u}_t \times \boldsymbol{u}_w) - \alpha_{atm} \frac{\rho_{atm(r)}}{\rho_p} \bar{v}_G \bar{\boldsymbol{v}}_G \tag{2.17}$$

where $m_t = \rho_t L_t w_t h_t$ is the tether mass, being ρ_t the tether density; ρ_p is the atmospheric density at the perigee; $b = m(c_d S)$ is the total ballistic coefficient; the parameter α_L is defined as:

$$\alpha_L = \frac{\sigma_t}{\rho_t} \frac{B_0^2 R_E^{3/2}}{\sqrt{\mu_E}}, \qquad \alpha_{atm} = \frac{1}{2b} R_E \rho_p \tag{2.18}$$

The ballistic coefficients of the tip-masses and the tether is here approximated as equal; furthermore, the rotational velocity of the system about its center of mass is much smaller than the orbital velocity, and can be then neglected. With these two assumptions, the torque about G, created by the aerodynamic forces, vanishes. The

torque about G is then generated only by the electrodynamic perturbations. The torque component orthogonal to the orbital plane, M^G, used in Eq. 2.12, is then computed and normalized as:

$$\overline{M}^G = \boldsymbol{u}_w \cdot \boldsymbol{M}^G = \boldsymbol{u}_w \cdot \left(\overline{GA} \times \overline{\boldsymbol{F}}_L + \overline{\boldsymbol{M}}^A\right) \tag{2.19}$$

$$= \boldsymbol{u}_w \cdot \left[- \int_0^{L_t} s\, i(s) ds \boldsymbol{u}_t \times (\boldsymbol{u}_t \times \boldsymbol{B}) + (L_t \boldsymbol{u}_t - \boldsymbol{x}_{CG}) \times \boldsymbol{F}_L \right] \tag{2.20}$$

$$= \frac{B_0}{\bar{r}_G^3} i_{sc} L_t^2 \left[\frac{x_{CG}}{L_t} - \left(1 - \frac{\overline{M}^A}{\overline{i_{av}}}\right) \right] \overline{i_{av}} \tag{2.21}$$

where $\boldsymbol{F}_L$ and $\boldsymbol{M}^A$ are the resultants of the Lorentz force and its moment about the anodic tip A. Eq.2.21 is obtained knowing that $\boldsymbol{u}_w \cdot [\boldsymbol{u}_t \times (\boldsymbol{u}_t \times \boldsymbol{u}_w)] = -1$. $\overline{M}^A$ depends only on the normalized tether length $\overline{L}_t$. From Eq. 2.21, the normalized torque appearing in Eq.2.12 is calculated as follows:

$$\overline{M}^G = \beta_L \left(\frac{R_E}{L_t}\right) \frac{\overline{m}_t}{3\sin^2 2\phi - 2\overline{m}_t} \frac{\boldsymbol{u}_t \cdot (\bar{\boldsymbol{v}}_G \times \boldsymbol{u}_w)}{\bar{r}_G^6} \left(\cos^2\phi - \bar{x}_{cp}\right) \overline{i_{av}} \tag{2.22}$$

where

$$\beta_L = 12 \sqrt{\frac{R_E}{\mu_E}} \frac{R_E B_0^2 \sigma_t}{\rho_t} \tag{2.23}$$

$$\bar{x}_{cp} = \frac{x_{cp}}{L_t} = 1 - \frac{\overline{M}^A}{\overline{i_{av}}} \tag{2.24}$$

The normalized variables $\overline{i_{av}}$, $\overline{M}^A$ and $\bar{x}_{cp}$, as well as the normalized maximum current i_B, at zero-bias point B, are plotted versus $\overline{L}_t$ in Fig. 2.3. $\bar{x}_{cp}$ is the normalized distance of the electrodynamic center of pressure from point C, i.e. the dimensional location x_{cp} divided by the tether length.

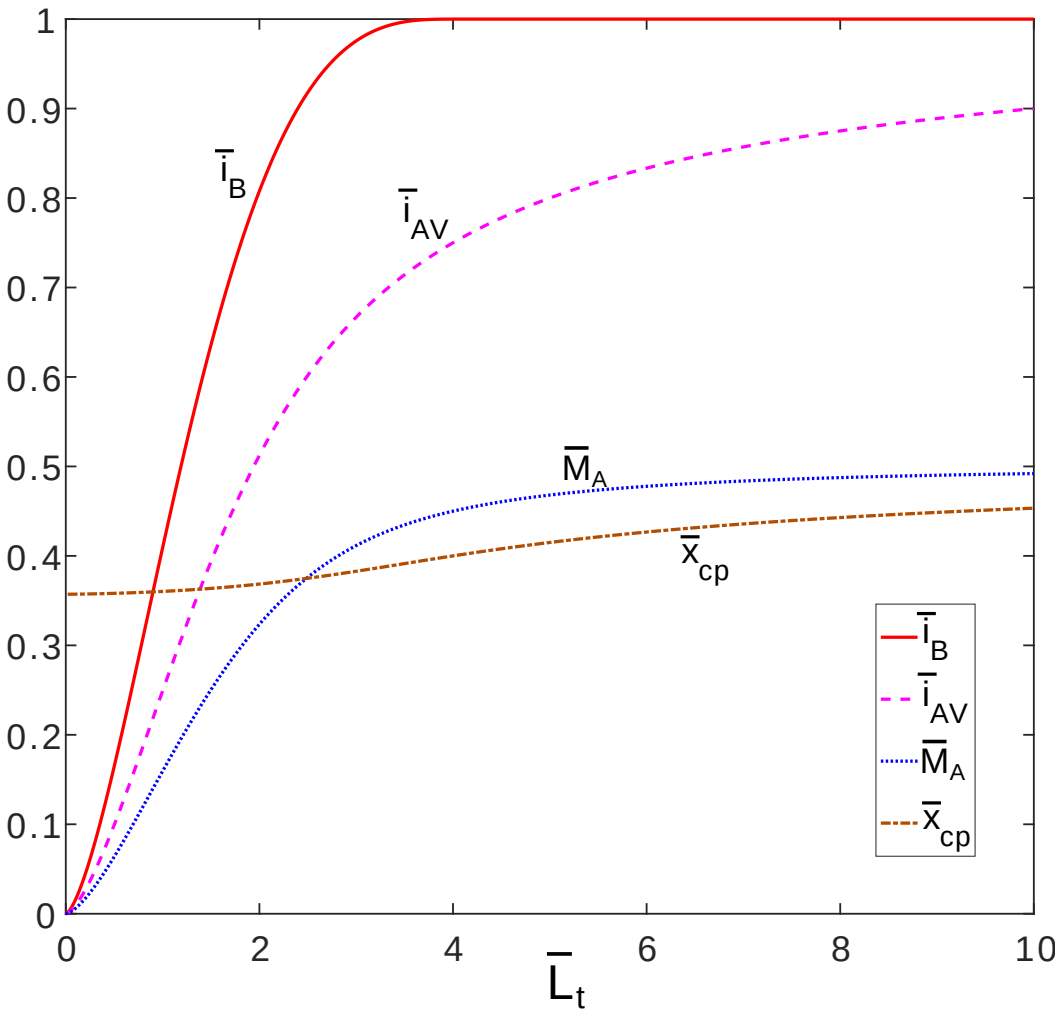

Figure 2.3: *Profiles of normalized maximum current $\overline{i_B}$, normalized average current $\overline{i_{av}}$, normalized torque about the anodic tip $\overline{M}_A$, normalized location along the tether of the electrodynamic center of pressure $\bar{x}_{cp}$. All these profiles with respect to the normalized tether length $\bar{L}_t$*

The numerical integration of Eqs. 2.9–2.12 with an ODE45 returns the time evolution of the orbital parameters. In parallel with these calculations, it is fundamental to monitor the evolution of the maximum tension along the tether, that occurs at the system's center of mass G. The tension is generated by the local rotation of the system about G, that gives the most relevant contribution, but also by the orbital motion, and the gravity gradient. Given that the Lorentz force is acting orthogonal to the tether, it does not contribute to tether tension. The contribution to tension from atmospheric drag can be reasonably neglected. The tether tension at the center of mass G, named T_G, must be smaller than the breaking tension dictated by tether material properties, accounting for a safety factor $\kappa > 1$. $T_G(\tau)$ varies during the deorbit time (or normalized time τ). The breaking tension is $T_* = (\sigma_{uts} w_t h_t)/\kappa$, where σ_{uts} is the ultimate tensile strength of the tether material and $w_t h_t$ the cross-section area of the tape tether. The following equation is computed for $T_G(\tau)/T_*$,

based on Ref. [8]:

$$\frac{T_G(\tau)}{T_*} = \delta \left(\frac{L_t}{R_E}\right)^2 \frac{cos^2\phi sin^2\phi}{\overline{m}_t}\left(1-\frac{\overline{m}_t}{2}\right)\left[\dot{\psi}^2 - \frac{1}{\bar{r}_G^3}(1-3cos^2\theta)\right] \tag{2.25}$$

where

$$\delta \equiv \frac{\kappa\ \mu_E\ \rho_t}{\sigma_{uts} R_E} \tag{2.26}$$

The tether does not break, during deorbit, if the maximum tension ratio $T_{G,max}/T_*$, is always lower than 1.

Calculation of normalized average current and normalized electrodynamic torque

The current and voltage profiles along an *ideal* tether with zero potential drop at the hollow cathode are described in works by Sanmartín and Ahedo (Ref. [42], [3]). The equations can be efficiently solved as presented by Sanjurjo et al.[38].

Assuming the electron collection to follow the *Orbital Motion Limited (OML)* regime, a *characteristic tether length* L_* can be defined as (Ref.[38]):

$$L_* = \left[\frac{9\pi^2}{128}\frac{m_e \sigma_t^2 E_t h_t^2}{q_e^3 N_e^2}\right]^{1/3} \tag{2.27}$$

If $\overline{L}_t = L_t/L_* < 4$ (i.e. in the *short tether regime*), the auxiliary variable υ_0 is first computed, from the nonlinear equation:

$$\overline{L}_t = \frac{4}{3}\frac{f(\upsilon_0)}{cosh^{1/3}\upsilon_0}, \quad f(x) \equiv \int_0^x \sinh^{1/3} y dy \tag{2.28}$$

by using a Newton-Raphson iterative method. The maximum normalized current, found at zero-bias point B, is $\overline{i_B} = acosh\left(1/(1-\overline{i_B})\right)$. Current and voltage profiles, in the *short tether regime*, are computed as follows:

$$\varphi(\bar{i}) = (\bar{i}_B - \bar{i})^{2/3}\left(2 - \bar{i}_B - \bar{i}\right)^{2/3} \tag{2.29}$$

$$\bar{i}(\upsilon) = 1 - (1-\bar{i}_B)\cosh\upsilon \tag{2.30}$$

$$\xi(\upsilon) = \frac{4}{3}(1-\bar{i}_B)^{1/3}\left[f(\upsilon_0) - f(\upsilon)\right] \tag{2.31}$$

Here $\xi = s/L_*$, where s is the location along tether measured from the anodic point A, $\bar{i} = i(s)/i_{sc}$, and $\varphi = V(s)/E_t L_*$ is the normalized tether bias.

Conversely, when $\overline{L}_t > 4$, the tether operates within the *long tether regime*. In this case, the maximum normalized current, at zero-bias point, is $\bar{i}_B = 1$, and

$$\varphi(\bar{i}) = (1 - \bar{i})^{4/3} \tag{2.32}$$

$$\xi(\bar{i}) = 4\left[1 - (1 - \bar{i})^{1/3}\right] \tag{2.33}$$

The normalized average current is then computed as:

$$\bar{i}_{av} = \frac{1}{i_{sc} L_t} \int_0^{L_t} i(s) ds = \frac{1}{\overline{L}_t} \int_0^{\overline{L}_t} \bar{i}(\xi) d\xi = 1 - \frac{\varphi_A}{\overline{L}_t} \tag{2.34}$$

where $d\varphi/d\xi = i - 1$ as in works by Sanmartín[42]. In the *short* and *long tether* regimes the average normalized current is, respectively, $\bar{i}_{av} = 1 - \left[\bar{i}_B^{2/3}(2 - \bar{i}_B)^{2/3}/\overline{L}_t\right]$ and $\bar{i}_{av} = 1 - \frac{1}{\overline{L}_t}$.

Using again $d\varphi/d\xi = i - 1$, and performing an integration by parts, the normalized Lorentz torque about the anodic point A is obtained:

$$\overline{M}^A = \frac{1}{i_{sc} L_t^2} \int_0^{L_t} s\, i(s) ds = \frac{1}{\overline{L}_t^2} \int_0^{\overline{L}_t} \xi \bar{i}(\xi) d\xi = \frac{1}{2} - \frac{1}{\overline{L}_t^2} \int_0^{\overline{L}_t} \varphi(\xi) d\xi \tag{2.35}$$

$\varphi(\xi)$ depends on the specific tether regime. Therefore, in the *short tether regime* the normalized torque is

$$\overline{M}^A = \frac{1}{2} - \frac{4}{3\overline{L}_t^2}(1 - \bar{i}_B)^{5/3} g(\upsilon_0) \tag{2.36}$$

where the function $g(x)$ is introduced, with respect to the variable x (that in case of Eq.2.36 is $x = \upsilon_0$, whereas the generic variable of integration is $y = \upsilon$), and defined as:

$$g(x) \equiv \int_0^x \sinh^{5/3} y dy \tag{2.37}$$

In the long tether regime:

$$\overline{M}^A = \frac{1}{2} - \frac{4}{5}\frac{1}{\overline{L}_t^2} \tag{2.38}$$

2.1.2 BET Deorbit mission design

Aluminum 1100 - H19 is used as base material for the conductive tether. Its properties are $\rho_t = 2700\,\mathrm{kg/m^3}$, $\sigma_t = 3.54e \times 10^7\,\Omega^{-1}\mathrm{m}^{-1}$. However, the numerical model can accept even other alternative conductive materials. In fact, instead of a pure Aluminum tether, a tether made of a *Metal Matrix Composite* (MMC) material, with Aluminum matrix reinforced with fibers, can be used. Such solution would lead to a much higher maximum tension sustainable by the material. Given that the code computes any Lorentz related quantity, using only the conductive material properties (i.e. the properties of the metallic matrix not of the fibers), no changes in ρ_t and σ_t are required in the code when using MMCs with Aluminum matrix instead of pure Aluminum. Results from computations are still valid: the only important feature that changes is the ratio between the maximum tension experienced by the tether and the maximum allowed tension dictated by the specific material ultimate tensile strength.

The simulations adopted these other parameters: $\kappa = 3$, frontal area-to-mass ratio $S/m = 0.03\,\mathrm{m^2kg^{-1}}$, Earth equatorial radius $R_E = 6378\,\mathrm{km}$, initial perigee altitude $H_{p0} = 300\,\mathrm{km}$ and atmospheric drag coefficient $c_d = 2.2$. With these values, these subsequent parameters are calculated and employed:

$$\alpha_L = 1.03 \times 10^{-2}, \quad \alpha_{atm} = 5.66 \times 10^{-6}, \quad \beta_L = 0.12, \quad \delta = 2.47 \times 10^3 \tag{2.39}$$

Using data extracted from the environmental models reported in Fig. 2.2, and the electrodynamic functions $\bar{i}_{av}(\overline{L}_t)$ and $\bar{x}_{cp}(\overline{L}_t)$, shown in Fig. 2.3, it turns out that the results given as output from this numerical model depend only on four design parameters given set as inputs by the user. These parameters are:

$$\overline{m}_t, \qquad \frac{L_t}{h_t^{2/3}}, \qquad L_t, \qquad \phi, \tag{2.40}$$

These input parameters need to be selected to yield a short deorbit, while ensuring a tether tension always below the maximum allowed tension.

The perturbation forces, i.e. the Lorentz drag and atmospheric drag, are proportional to the normalized tether mass $\overline{m}_t$, whereas T_G/T_* decreases with increasing $\overline{m}_t$. Consequently, the higher is $\overline{m}_t$, the lower is the deorbit time and the tether tension. However, $\overline{m}_t$ should be as low as possible in order to have a low tether mass, and therefore a competitive technology. For all simulations presented here, $\overline{m}_t = 0.03$ is used, i.e. a tether mass about 3% of the total mass of the system. This $\overline{m}_t$ value yields values of ϕ in the range $0.12278 = \phi_{min} \leq \phi \leq \phi_{max} = 1.4480$.

The second and third parameters, L_t and $L_t/h^{2/3}$ involve the tether length and its thickness. As shown in Fig. 2.3, a longer and thinner tether (large $\overline{L}_t$) is more efficient, since it leads to a higher average current. However, the tether length should not

be too high because the tension grows quadratically with L_t (see Eq. 2.25). In the analyses presented in this Section 2.1, the reasonable values $L_t = 2\,\text{km}$ and $h_t = 100\,\mu\text{m}$ are used.

The fourth parameter, ϕ, controls the mass distribution at the tether tips, and it is used to perform a parametric analysis. A particularly interesting value of ϕ is the one that makes the electrodynamic torque to vanish at the initial perigee: this value is denoted as ϕ_0. It is important to remark that $\overline{L}_t$ is ambient related, and therefore it changes continuously during deorbit, causing in turn a continuous change of location of the electrodynamic center of pressure.
The value of ϕ_0 is given by the condition:

$$cos^2(\phi_0) = \bar{x}_{cp,0} \tag{2.41}$$

where $x_{cp,0}$ is the normalized distance between the cathodic tip C and the electrodynamic center of pressure, at the initial perigee. Tethered systems with $\phi = \phi_0$ are named *self-balanced* (Ref. [33]), and were proposed in previous literature as a solution to mitigate the dynamic instability in librating tethers (Ref. [34]).

From the chosen initial perigee altitude ($H_p = 300\,\text{km}$) and environmental models, the value of $\phi_0 = 0.92099$ is computed.
The initial apogee altitude of the GTO orbit is set equal to $H_{a0} = 35786\,\text{km}$, i.e. the GEO altitude. Having set the initial perigee and apogee radii, the initial normalized semi-major axis and the initial orbital eccentricity are derived, $\overline{a}_0 = 3.8320$, $e_0 = 0.72675$. The other initial conditions are $\nu_0 = 0$ and $\theta_0 = 0$, that correspond to simulations starting from the initial perigee, and with tether initially aligned with the local vertical. The orbital inclination, the right ascension of the ascending node and the argument of perigee, are assumed to be zero and kept constant throughout all simulations.

2.1.3 Numerical Simulations

Single Case Analysis

A statistical analysis is performed with the software *Stela*® (courtesy of *Centre National d'Etudes Spatiales*, CNES) in order to estimate the reentry time by natural decay for an object like *Sylda* from GTO, with a perigee at 300 km and apogee at GEO. Results from this analysis confirm that there is about 90% probability that Sylda needs more than 25 years, in order to naturally reenter. Consequently, the maximum allowed time allowed for removal of any inactive object would be surpassed (maximum time set by international guidelines such as from NASA Ref. [1]).

Subsequently, an analysis with the model presented in Sec.2.1.1 is carried out, considering a single case of deorbit, i.e. setting a single value of $\phi = 0.99\phi_0$.

The parameters presented in Sec.2.1.2 are used, and an initial positive angular velocity of rotation about G, i.e. $d\theta/dt = 0.004\,\text{rad/s}$. When using $\phi < \phi_0$, like in this case, a positive initial angular velocity is required and its magnitude must be greater than about 0.003–0.005 rad/s, depending on the specific value of ϕ. It is fundamental to use such value at the start of simulations for two reasons: it is possible to deploy the tether reaching a non-zero angular velocity at the end of deployment, in a highly eccentric orbit; secondly, a high enough, yet still low, value of initial angular velocity prevents tether slackness in the initial phase of deorbit, i.e. it prevents any change in sign of the angular velocity. Such occurrence would lead, in fact, to instances when the tether has no positive tension acting on it, and this would generate instabilities, since a flexible tether cannot resist compression and would consequently bend, losing its nominal straight configuration. Conversely, an angular velocity that always preserves the same sign, meaning that rotation always take place in one direction, determines a variable but always positive centrifugal force, i.e. that creates tension not compression, and maintains the tether in a stable straight configuration.
The initial value of $d\theta/dt$ must be positive, since for $\phi < \phi_0$ the Lorentz torque about G will have positive sign during deorbit, so the local rotation will naturally take place in the same direction as the orbital motion (same sign as $d\nu/dt$).
The simulation leads to a total deorbit time of 987 days, i.e. approximately 2.7 years. This time is much lower than the most probable *natural decay* time for an object like *Sylda* from GTO, being higher than 25 years, as reported earlier.
Profiles of different parameters versus time are computed for this single case of deorbit, and shown in Fig.2.4.

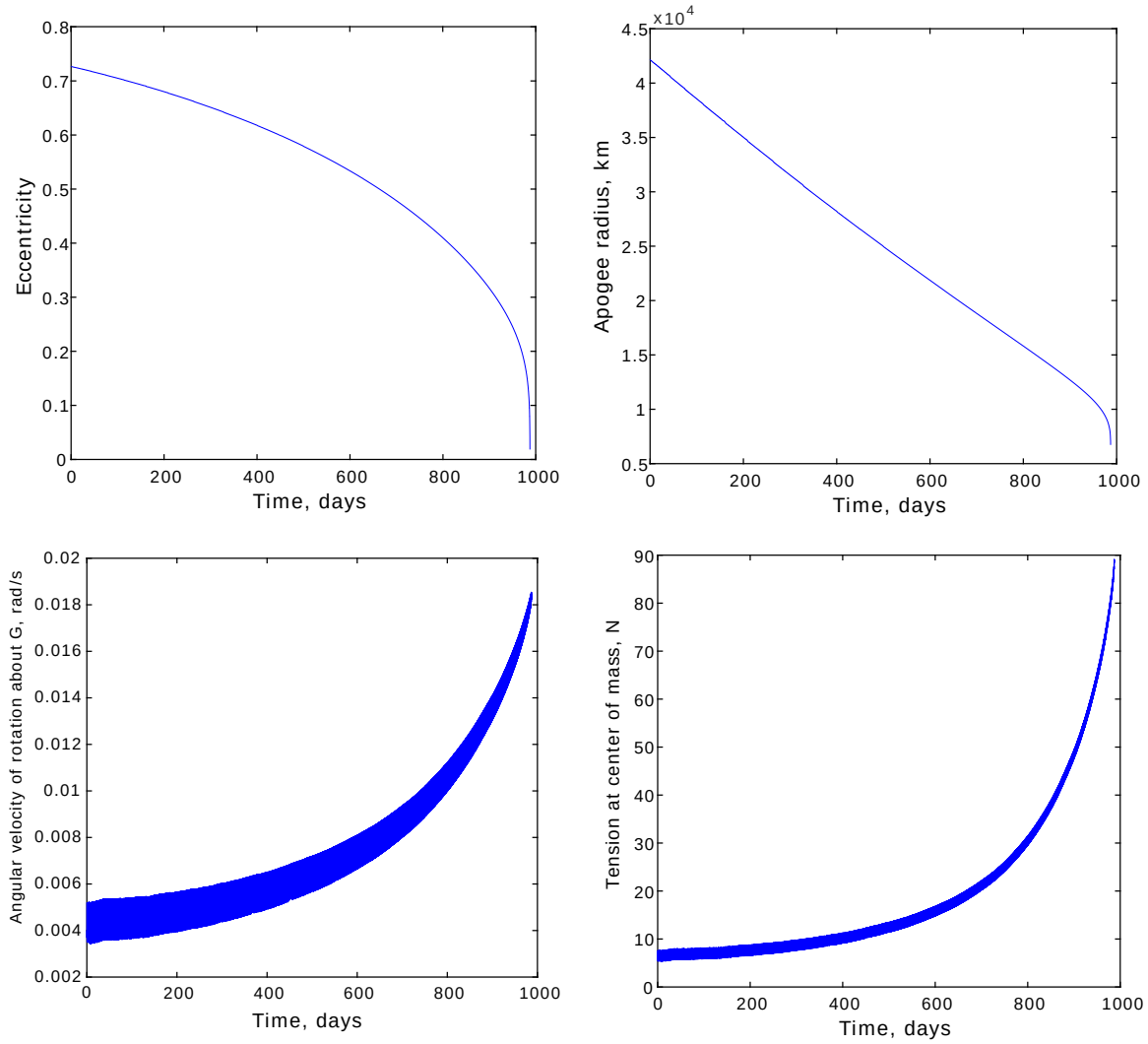

Figure 2.4: *Profiles of different parameters throughout the entire deorbit, with* $\boldsymbol{\phi = 0.99\phi_0}$*, and initial angular velocity of* $\boldsymbol{d\theta/dt = 0.004\,\mathrm{rad/s}}$.

As shown in Fig. 2.4, the orbital eccentricity and the apogee radius decrease, for most of the deorbit, almost linearly over time, especially the apogee radius. Only in the last part of deorbit they decrease faster due to the much higher time spent in regions where both Lorentz and atmospheric drag are present.
Figure 2.4 shows that the angular velocity $d\theta/dt$ oscillates over time, but has a constantly increasing trend with always positive values. This means that the system rotates locally, about its center of mass, always in the same direction as the orbital motion.
The evolution over time of tension at center of mass, Γ, shows an oscillating behavior, with values always positive, and with constantly increasing trend. This correspond to what is expected given the angular velocity $d\theta/dt$ profile. Γ experiences a very gradual increase for about 70% of the total deorbit time. In the last 30% of the deorbit, Γ steeply increases reaching its maximum value, $\Gamma_{max} \approx 88\,\mathrm{N}$, at the end of deorbit. A full deorbit, without instability and without breaking the tether, is possible even with a tether material with low mechanical properties, such as $Al1100$. This material has

an ultimate tensile strength of $\sigma_{uts} = 205\,\text{MPa}$. With a GTO typical total system mass $m = 500\,\text{kg}$, tether thickness $h_t = 100\mu m$, consequent tether width $w_t \approx 2.8\,\text{cm}$, and safety factor $\kappa = 3$, the value of Γ_* for $Al1100$ is 190 N, that is largely greater than $\Gamma_{max} \approx 88\,\text{N}$, found with this simulation.

Multiple case analysis

Following the first single-case analysis, a batch of additional simulations were run, changing only the parameter ϕ, and keeping constant all the other values. The full range of ϕ, from ϕ_{min} to ϕ_{max} is divided in a series of progressively increasing values. For each value of ϕ, a full deorbit simulation is performed, computing the maximum tension during deorbit, Γ_{max}, at the system's center of mass. Figure 2.5 shows Γ_{max} versus ϕ. The full range of possible values of ϕ is used for the plot, going from ϕ_{min}, corresponding to $m_C = 0$, to ϕ_{max}, corresponding to $m_A = 0$.

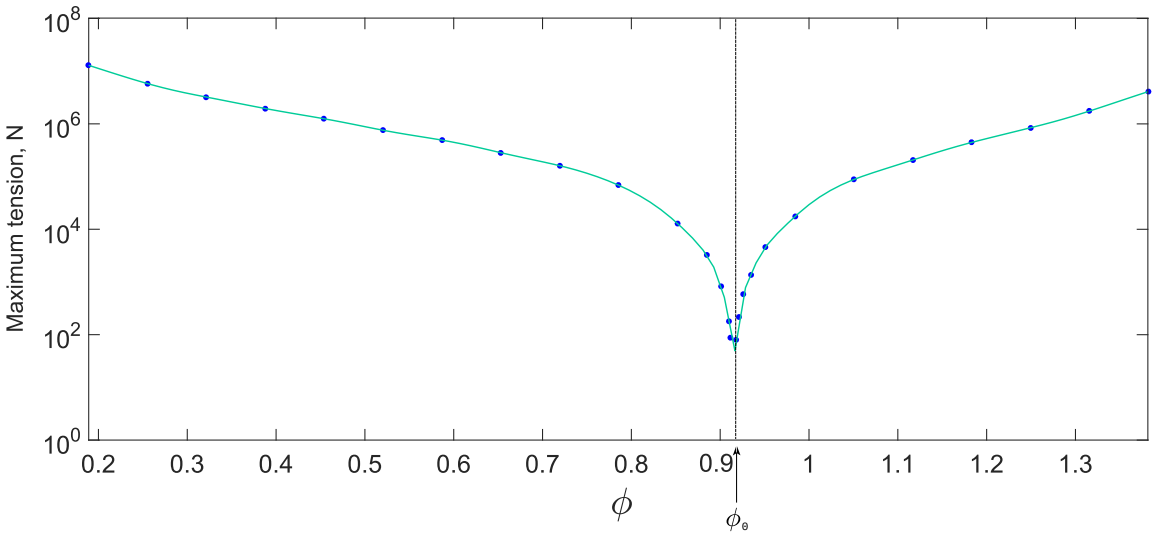

Figure 2.5: *Profile of maximum tension* $\boldsymbol{\Gamma_{max}}$*, during the entire deorbit at point G, versus different configurations of tethered system, defined by different values of* $\boldsymbol{\phi}$*. The y-axis of the plot is in logarithmic scale.* 27 *full deorbit simulations are performed, producing the* 27 *points in the figure. A spline interpolation is used to compute a curve from these* 27 *points.*

Every value in this plot is such that no tether slackness takes place. Hence, for each case, a nonzero initial angular velocity is considered. For $\phi < \phi_0$, an initial minimum value $d\theta/dt = +0.003\,\text{rad/s}$ must be used, whereas for $\phi > \phi_0$ a value of same magnitude but opposite sign ($d\theta/dt = -0.003\,\text{rad/s}$). In order to have the minimum tension during deorbit, it is important to select the minimum value of initial angular velocity that prevents slackness.
As expected, the lowest values of maximum tension at G occur for ϕ around ϕ_0. This multiple-case analysis proves the fact that it is fundamental, in order to prevent tether breaking, to keep the Lorentz torque as small as possible during deorbit. This allows for lower angular velocities of rotation about G, lower centrifugal force and ultimately

lower tether tension. In order to have small Lorentz torque, the system should be configured in a way such that its center of mass is as close as possible to the electrodynamic center of pressure throughout deorbit. The Lorentz torque will generally be nonzero and variable during deorbit, given that the center of mass is fixed, whereas the electrodynamic center of pressure location changes over time. By using a value of ϕ in the proximity of ϕ_0, the Lorentz force moment arm will be variable, yet low, during deorbit. Therefore, also tension at G will be generally low, for ϕ close to ϕ_0.
The allowed values of ϕ lie around ϕ_0. This means that the center of mass of the system must be far enough both from the anodic tip A and the cathodic tip C. This goal can be achieved by using a *butterfly* configuration for the system, i.e. by having the massive object to deorbit close to the electrodynamic center of pressure, and the tether subdivided in two segments deployed along opposite directions from the object to deorbit (Sylda in this case). The lengths of the two tether segments must be optimized in order to minimize the distance between the system's center of mass and the electrodynamic center of pressure throughout deorbit.

From the curve shown in Fig. 2.5, the user, after selecting the tether material, can derive the range of allowed ϕ values that enable a full deorbit, avoiding both tether slackness and breaking.
The values computed in this analysis assume the density and electrical conductivity of Aluminum 1100, but they are valid also for Metal Matrix Composites (MMC) where the matrix is made of Aluminum, for the reasons already described in Sec.2.1.2. For example, by using a tape tether made of *MetPreg*^{TM} *Fiber Reinforced Aluminum*, both a high resistance to space thermal environment and very high mechanical properties are achieved. This material has an *ultimate tensile strength* $\sigma_{uts} = 1450\,\text{MPa}$ (source of data `www.matweb.com`). This value, together with the already presented values $\kappa = 3$, $h_t = 100\mu m$, and $w_t = 2.8\,\text{cm}$, leads to a $\Gamma_* = 1750\,\text{N}$. In this case, it is then found a range of allowed ϕ between approximately 0.89 and 0.94, corresponding to a center of mass allowed location between about 700 m to 790 m from the cathodic tip C, with a tether of length $L_t = 2\,\text{km}$.
In case a material different from Aluminum is used, as conductive matrix, the model developed here can easily accommodate this, by just changing the values of ρ_t and σ_t. In this case, the numerical output will be different, yet the shape of the curves and the comments on the results would still apply.

For each of the 27 simulations reported in Fig. 2.5, the total deorbit time is computed too, finding out that it is only slightly variable with the variation of ϕ from ϕ_{min} to ϕ_{max}. The deorbit time, averaged on the full range of ϕ, is about 973 days, i.e. about 2.67 years.

2.2 Second phase of analysis: deorbit with BET and hybrid model

Results from Sec. 2.1 show that deorbit without tether instability and breaking can be achieved by designing a system with center of mass very close to the electrodynamic center of pressure, i.e. the point where the resultant of the Lorentz drag force is acting. The configuration of the system plays then a pivotal role. The mass of the object to deorbit is a constraint, thus the designer can play only with tether's characteristics and tip mass. The minimization of the distance between center of mass and electrodynamic center of pressure can be achieved more easily with a butterfly configuration than with a single-tether configuration. Therefore, this will be the configuration for the BET system considered in this second phase of deorbit simulations.

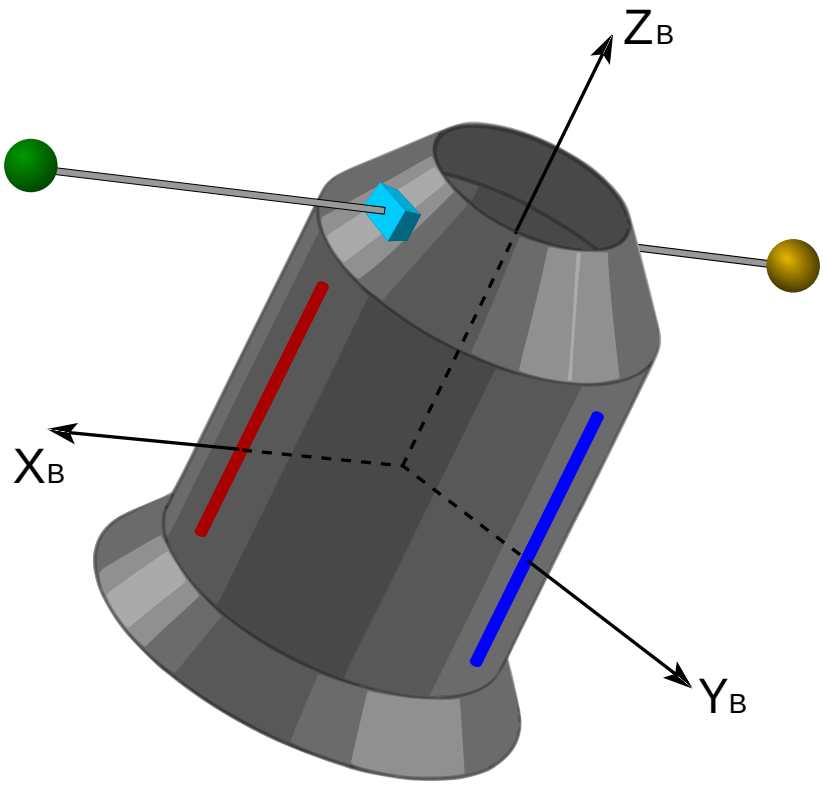

Figure 2.6: *View of Sylda when deorbit starts. The two tethers in the dumbbell model are aligned with the first axis of the body frame X_B and deployed along symmetrically opposite directions. The two tethers are then electrically connected on Sylda and stored in separate boxes placed axialsymmetrically. In green and yellow the anodic and cathodic tip-masses. On the cylindrical body two magnetic torquers are mounted (refer to Sec. 3.2) for explanation.*

In all analyses presented in Sec. 2.2, these are the main features of both the *global* and *local* motion of the BET system:

- Both dynamics on the orbital plane and out-of-plane are considered.

- All the orbital parameters are considered variable, differently from what was done in the previous batch of analyses. Hence, there is a variation in orbital inclination i, argument of perigee ω, right ascension of the ascending node Ω, in addition to semi-major axis a and eccentricity e.
- *Rigid dumbbell model* for the tether, but it is split into two separate rigid dumbbells, one for each tether when using the butterfly configuration. Therefore, there are two degrees of freedom for each tether (i.e. the local rotations on the orbital plane and out-of-plane, around the system's center of mass).
- *Hybrid* model, combining the advantages of the *dimensional* model developed in the first part of the PhD research and the *nondimensional* model described in Section 2.1.
- Sylda and the two tip-masses are all modeled as point masses rotating together with the rest of the dumbbell system.
- the variation of current along the tether is considered, and an average value of current is computed as well as an electrodynamic center of pressure, where the resulting Lorentz force acts in order to create the same dynamics as when considering a distributed force.
- Only one cathode is considered, that is part of one of the two tip-masses. This means that even is the tether is deployed two-ways, it is a single electrodynamic tether: consequently, a current is generated only during the part of the rotation when the inducted electrical field is positive, not all the times.

The state of the tethered system, with the model considered here, can be univocally defined when these parameters are known:

- the length of each tether segment L_1 and L_2 of the butterfly system.
- the radius vector $\boldsymbol{r}_G = \boldsymbol{r}_A$ from the center of the Earth to the center of mass of the system (assumed coincident with Sylda as point mass A).
- the angle of true anomaly of center of mass along the orbit, ν.
- the angle of in-plane rotation θ of the tethered system about its center of mass, on the plane of the orbit.
- the angle of out-of-plane rotation φ of the tethered system about its center of mass, out of the orbital plane.

The following perturbations are considered in the code:

- *Electrodynamic, or Lorentz, Drag*
- *Atmospheric Drag* is considered since it is desired to study the behaviour of a non-electrodynamic tether, with deorbit based only on atmospheric drag acting on the tether.

2.2.1 *Hybrid* computational model

The nondimensional approach has the great advantage of increasing the computational efficiency and providing a more flexible code, but also the disadvantage of making the parameters and the equations less intuitive and straight-forward. The solution adopted in this second phase of analyses presented in Sec. 2.2 is to combine the advantages of both methods, and attenuate the respective disadvantages. The nondimensional approach is then kept only for the computation of the electrodynamic drag and torque, whereas the integration of orbital and local dynamics, as well as all other operations are done with dimensional parameters and equations. This combined approach will be called here *hybrid* method.

The tethered system for deorbit is modeled as a rigid dumbbell with 3 point masses: the mass of the object to deorbit m_S, the mass at anodic tip m_A, and the mass at cathodic tip m_C. These masses are connected by two opposite segments of a single conductive tether, respectively of lengths L_1 and L_2. The two segments are electrically connected and homogeneous, creating a total tether of length $L_t = L_1 + L_2$. In computations these features are used for the tether: total length of 2 km, $L_2 = L_1/4$, width of 3 cm and thickness of $100\mu m$. The ratio between L_1 and L_2 is a parameter to be optimized in order to avoid tether instability and seizure during deorbit. Previous analyses showed that L_1 and L_2 should be tuned such that the center of mass G is as close as possible to the electrodynamic center of pressure of the tether. The total mass of the tether is m_t. The total mass of the system is: $m = m_A + m_S + m_C + m_t$. An abscissa x along the rigid tether is defined, starting from cathodic tip C and pointing towards A (unit vector u_t).

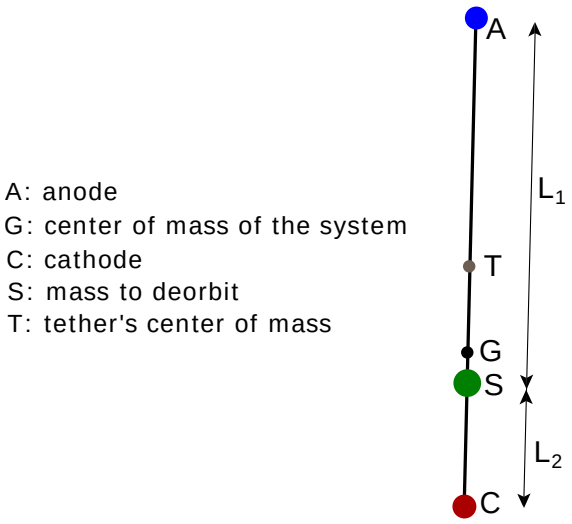

Figure 2.7: *Butterfly configuration*

Two reference frames are used, and defined as reported in Appendix B:

- an *orbital frame* of unit vectors $\boldsymbol{u}_r$, $\boldsymbol{u}_s$, $\boldsymbol{u}_w$.
- a *body frame* of unit vectors $\boldsymbol{u}_\xi$, $\boldsymbol{u}_\eta$,$\boldsymbol{u}_\zeta$. The first unit vector $\boldsymbol{u}_\xi$ is coincident

with $\boldsymbol{u}_t$ after deployment, i.e. when the tethers and Sylda rotate together as a single rigid body as a dumbbell. Before deployment and during deployment, as discussed in Chapter 3, the body frame is fixed to Sylda's body and co-moving with it, and the tethers rotate with respect to it. In Appendix B more details about the body frame are provided.

The code simulates a full deorbit by implementing perturbation equations anytime the object is at an altitude lower than 2000 km, where electrodynamic drag becomes significant. At altitudes lower than 1000 km, also the atmospheric drag is added. Other perturbation forces, such as solar pressure, or gravitational higher harmonics are less significant and therefore neglected in this analysis.

The deorbit simulation begins at the perigee of the initial GTO orbit, with perigee altitude of 300 km, with tether fully deployed and with $\boldsymbol{u}_t$ initially aligned with $\boldsymbol{u}_r$.

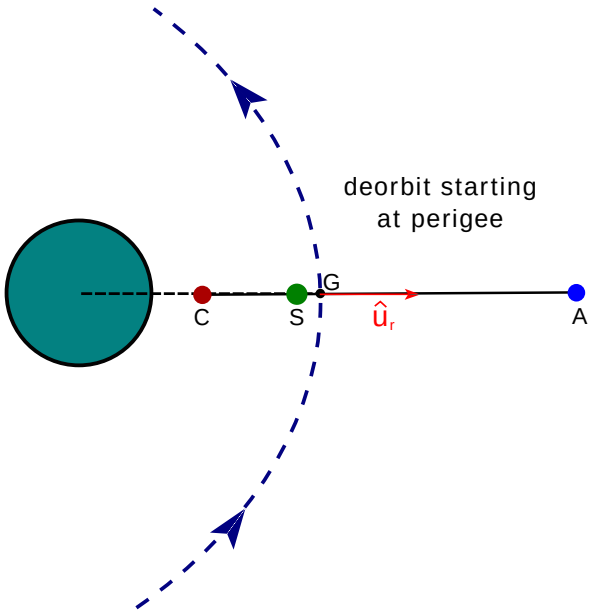

Figure 2.8: *Configuration at beginning of deployment simulation*

The following set of dimensional equations is used for the simulation of the perturbed orbital motion of the center of mass G, and for the local rotation motion of the dumbbell system around G. The orbital inclination is considered fixed and equal to zero.

The first batch of six differential equations, taken from Bate[7], employ the *Gauss* formulation to compute the variation of orbital parameters due to perturbations:

$$\frac{da}{dt} = \dot{a} = \frac{2a^{3/2}}{\sqrt{\mu(1-e^2)}} \left[e\ \sin\nu f_r + (1 + e\ \cos\nu) f_s\right] \tag{2.42}$$

$$\frac{de}{dt} = \dot{e} = \sqrt{\frac{a(1-e^2)}{\mu}} \left[\sin\nu f_r + \frac{2\cos\nu + e(1+\cos^2\nu)}{1 + e\ \cos\nu} f_s\right] \tag{2.43}$$

$$\frac{d\nu}{dt} = \dot{\nu} = \frac{\sqrt{\mu a(1-e^2)}}{r_G^2} - \sqrt{\frac{a(1-e^2)}{\mu}} \left[-\frac{\cos\nu}{e} f_r + \frac{\sin\nu}{e}\left(1 + \frac{1}{1 + e\cos\nu}\right) f_s\right] \tag{2.44}$$

$$\frac{d\Omega}{dt} = \frac{r_G\ f_w\ \sin(\omega + \nu)}{\sqrt{\mu a(1-e^2)}\ \sin i} \tag{2.45}$$

$$\frac{d\omega}{dt} = \dot{\omega} = \sqrt{\frac{a(1-e^2)}{\mu}} \left[-\frac{\cos\nu}{e} f_r + \frac{\sin\nu}{e}\left(1 + \frac{1}{1 + e\cos\nu}\right) f_s - \frac{\sin(\omega + \nu)}{\tan i(1 + e\cos\nu)} f_w\right] \tag{2.46}$$

where a is the semi-major axis, e is the orbital eccentricity, i is the orbital inclination, ω the argument of perigee, ν the true anomaly, μ the Earth's gravitational parameter. f_r, f_s, f_w are the total perturbation forces per unit mass (i.e. accelerations) along the axes of the orbital frame. The previous equations define the perturbed orbital motion of the center of mass G of the tethered system.

In addition to these equations, other two equations are used, that describe the local rotation about G. These equations are derived from Beletsky[8]. Both the rotation on the orbital plane θ and the rotation out of the orbital plane φ are considered: this means that the orientation of the tethered system, and the body frame fixed to it, with respect to the orbital frame, is defined by the two angles θ and φ.

$$\ddot{\psi} = 2\dot{\varphi}\ \dot{\psi} \tan\varphi - \frac{3\mu}{2\ r_G^3} \sin 2(\psi - \nu) + \alpha_\theta + \frac{M_\zeta}{J^G \cos\varphi} \tag{2.47}$$

$$\ddot{\varphi} = -\left[\dot{\psi}^2 + \frac{3\mu}{r_G^3} \cos^2(\psi - \nu)\right] \frac{\sin 2\varphi}{2} - \alpha_\varphi - \frac{M_\eta}{J^G} \tag{2.48}$$

where $\psi = \theta + \nu$; $r = a(1-e^2)/(1 + e\cos\nu)$ and $\alpha_\theta \approx \alpha_\varphi \approx 10^{-3}\ \dot{\nu}^2$, following the approximation at pg. 74 of Beletsky[8]. J^G is the moment of inertia of the dumbbell *butterfly* system relative to an axis perpendicular to the tether, and passing through G (the system's center of mass). It is assumed a slender rod model for the tether, and point masses for all the bodies at C, S, A points. Sylda has the same moments of inertia with respect to the axes of in-plane and out-of-plane rotations since it is an axialsymmetric body. Given these assumptions, J^G is the same regardless of the specific orientation of the axis perpendicular to the tether: this means that for in-plane and out-of-plane rotation the same J^G is used. J^G can be computed as:

$$J^G = m_A x_{GA}^2 + m_C x_{CG}^2 + J_S + m_S x_{GS}^2 + \frac{1}{12} m_t L_t + m_t x_{GT}^2 \tag{2.49}$$

being L_t the tether length; x_{GA} the distance from point A and center of mass G; x_{CG} the distance from point C and center of mass G; x_{GT} the distance from center of mass of the tether and system's center of mass G; x_{GS} the distance from point S (Sylda's location) and center of mass G. $J_S = J_{S,x} = J_{S,y}$ is the moment of inertia of Sylda with respect to the axis orthogonal to the orbital plane and passing through its center of mass (computed with *Solidworks* as reported in Sec. 1.3.1).

In Eqns. 2.47 and 2.48, the force moments (in Nm) are expressed in body frame components M_ξ, M_η, M_ζ.

Two perturbation forces, and respective moments, are computed in the orbital frame: aerodynamic ($\boldsymbol{F}_{atm}$, $\boldsymbol{M}_{atm}$) and electrodynamic ($\boldsymbol{F}_L$, $\boldsymbol{M}_L$). The torques are then transformed in body frame coordinates.

$$M_\eta = \boldsymbol{M}^G \cdot \boldsymbol{u}_\eta = (\boldsymbol{M}^G_{ad} + \boldsymbol{M}^G_L) \cdot \boldsymbol{u}_\eta \tag{2.50}$$

$$M_\zeta = \boldsymbol{M}^G \cdot \boldsymbol{u}_\zeta = (\boldsymbol{M}^G_{ad} + \boldsymbol{M}^G_L) \cdot \boldsymbol{u}_\zeta \tag{2.51}$$

The transformation matrix from the orbital frame to the body frame is computed using Euler angles θ and φ (as a 3-2 rotation):

$$R^B_O = \begin{bmatrix} \cos(\theta)\cos(\varphi) & \sin(\theta)\cos(\varphi) & -\sin(\varphi) \\ -\sin(\theta) & \cos(\theta) & 0 \\ \cos(\theta)\sin(\varphi) & \sin(\theta)\sin(\varphi) & \cos(\varphi) \end{bmatrix} \tag{2.52}$$

The aerodynamic force is computed as:

$$\boldsymbol{F}_{atm} = -\frac{1}{2} c_d S_{atm,avg} \rho_{atm} v_G \boldsymbol{v}_G \tag{2.53}$$

where $\boldsymbol{v}_G$ is the orbital velocity of the center of mass of the system, c_d the atmospheric drag coefficient, $S_{atm,avg}$ the average surface exposed to atmospheric drag, ρ_{atm} the local atmospheric density. The same velocity with respect to the atmosphere is assumed for all points of the system: this means that the difference in velocity from point to point of the system, due to the local rotational motion, is neglected (it is much lower than the orbital velocity). Likewise, the same atmospheric density is considered for all points of the system. The surface exposed to drag changes with the rotation of the system. A constant value is used, obtained making the average between a condition of maximum exposed drag area, and a minimum of zero exposed drag area (dumbbell aligned with $\boldsymbol{v}_G$. The average value of drag area is $S_{atm,avg} = (2S_{atm})/\pi$ where S_{atm} is the maximum exposed area of the entire system.

The moment generated by the drag force, about the center of mass G, is calculated using an *aerodynamic center of pressure* defined as:

$$x_{P,atm} = \frac{-x_C G S_{C,atm} - x_S G S_{S,atm} + x_A G S_{A,atm} + x_T G S_{t,atm}}{S_{atm}} \tag{2.54}$$

where $S_{C,atm}$, $S_{S,atm}$, $S_{A,atm}$, $S_{t,atm}$ are the maximum atmospheric drag exposed area of (respectively) the cathodic mass, Sylda, the anodic mass, the tether. $S_{atm} = S_{C,atm} + S_{S,atm} + S_{A,atm} + S_{t,atm}$. x is the location of each point along the tether starting from the cathodic tip C (e.g. $x_S G = x_C S - x_C G$).

The torque about G due to the aerodynamic drag is then obtained as:

$$\boldsymbol{M}^G_{atm} = x_{P,atm} \boldsymbol{u}_t \times \boldsymbol{F}_{atm} \tag{2.55}$$

The electrodynamic Lorentz force is computed, using the nondimensional method and the normalized average current $\bar{i}_{av}$, similarly as what done in Section 2.1:

$$\boldsymbol{F}_L = i_{sc} L_t \bar{i}_{av} \left(\boldsymbol{u}_t \times \boldsymbol{B} \right) \tag{2.56}$$

where $i_{sc} = E_t \sigma_t w_t h_t$, h_t tether thickness, w_t tether width, σ_t tether electrical conductivity, $E_t = \boldsymbol{u}_t \cdot (\boldsymbol{v}_G \times \boldsymbol{B})$ is the electrical field component along the tether, $\boldsymbol{B}$ is the geomagnetic induction field. The geomagnetic field, in all computations presented in Sec.2.2 is obtained with the method described in Appendix D, accounting for all higher harmonics. The moment about G created by the Lorentz force is computed by using the center of pressure location with respect to G, i.e. $x_{cp} - x_G$:

$$\boldsymbol{M}^G_{ed} = (x_{cp} - x_G) \boldsymbol{u}_t \times \boldsymbol{F}_L \tag{2.57}$$

where $x_{cp} = \bar{x}_{cp} L_t$ (being L_t the tether length). $\bar{x}_{cp}$ is the normalized distance of the electrodynamic center of pressure from the cathodic tip C. The normalized values of average current $\bar{i}_{av}$ and center of pressure location $\bar{x}_{cp}$ are found based on the normalized tether length $\bar{L}_t$, defined as described in Sec. 2.1.

For computational efficiency a numerically computed profile of i_{av} and x_{cp} with respect to l_t is implemented in the code. This means that at every step of integration a new value of l_t is calculated, and then used to extract the corresponding values of i_{av} and x_{cp} from the profile. Therefore, it is not necessary to fully compute i_{av} and x_{cp} at each integration step. This is the advantage given by the nondimensional approach, used hereby only for computation of i_{av}, x_{cp} and electron density N_e. In all other computations, the dimensional equations and parameters are employed.

Equations for nonzero variable inclination

$$\frac{da}{dt} = \dot{a} = \frac{2a^{3/2}}{\sqrt{\mu(1-e^2)}} \left[e\ \sin\nu f_r + (1 + e\ \cos\nu) f_s\right] \tag{2.58}$$

$$\frac{de}{dt} = \dot{e} = \sqrt{\frac{a(1-e^2)}{\mu}} \left[\sin\nu f_r + \frac{2\cos\nu + e(1+\cos^2\nu)}{1 + e\ \cos\nu} f_s\right] \tag{2.59}$$

$$\frac{d\nu}{dt} = \dot{\nu} = \frac{\sqrt{\mu a(1-e^2)}}{r_G^2} - \sqrt{\frac{a(1-e^2)}{\mu}} \left[-\frac{\cos\nu}{e} f_r + \frac{\sin\nu}{e}\left(1 + \frac{1}{1 + e\cos\nu}\right) f_s\right] \tag{2.60}$$

$$\frac{di}{dt} = \sqrt{\frac{a(1-e^2)}{\mu}} \frac{\cos(\omega+\nu)}{1 + e\ \cos\nu} f_w \tag{2.61}$$

$$\frac{d\Omega}{dt} = \frac{r_G\ f_w\ \sin(\omega+\nu)}{\sqrt{\mu a(1-e^2)}\ \sin i} \tag{2.62}$$

$$\frac{d\omega}{dt} = \dot{\omega} = \sqrt{\frac{a(1-e^2)}{\mu}} \left[-\frac{\cos\nu}{e} f_r + \frac{\sin\nu}{e}\left(1 + \frac{1}{1 + e\cos\nu}\right) f_s - \frac{\sin(\omega+\nu)}{\tan i(1 + e\cos\nu)} f_w\right] \tag{2.63}$$

Parameters a, e, i, Ω, ω in the equations above change only due to perturbation forces acting on the system's center of mass. Instead, the true anomaly in Eq. 2.60 is a parameter that changes along an unperturbed orbit too: thus, here $\dot{\nu}$ changes both for the features of the unperturbed orbit, and for the perturbations on the orbital plane f_r and f_s. The part of change due to perturbations is:

$$\frac{d\nu}{dt}_{pert} = -\frac{d\omega}{dt}_{r,s} \tag{2.64}$$

as reported on Ref.[7] at pg. 406.

When the inclination is not zero and variable, Eqns. 2.47 and 2.48 cannot be used anymore with the variable $\psi = \theta + \nu$. The correct equations are:

$$\ddot{\theta} = -\dot{\omega}_z + 2\dot{\varphi} tan\varphi(\dot{\theta} + \omega_z) - \frac{3\mu}{2\ r_G^3} \sin 2\theta + \alpha_\theta + \frac{M_\zeta}{J^G \cos\varphi} \tag{2.65}$$

$$\ddot{\varphi} = -\left[\left(\dot{\theta} + \omega_z\right)^2 + \frac{3\mu}{r_G^3} \cos^2\theta\right] \frac{\sin 2\varphi}{2} - \alpha_\varphi - \frac{M_\eta}{J^G} \tag{2.66}$$

where

$$\omega_z = \dot{\nu} \cos i \tag{2.67}$$

$$\dot{\omega}_z = \ddot{\nu} \cos i - \dot{\nu} \sin i \frac{di}{dt} \tag{2.68}$$

$$\ddot{\nu} = -\frac{2e\mu \sin \nu}{r_G^3} \tag{2.69}$$

The system rotates about its center of mass due to the torque exerted by external forces, but this rotation increases very slowly since the moment of inertia of the system is very large, given the length of the tether on the order of 1–2 km.

2.2.2 Numerical simulations

A simulation is run with the tether of total length of 2 km, subdivided in two segments in butterfly configuration of respective lengths of 1200 m and 800 m: these are found to be optimal length values to minimize the distance between the system's center of mass and the electrodynamic center of pressure over the entire deorbit.

The following profiles are computed, for various orbital parameters.

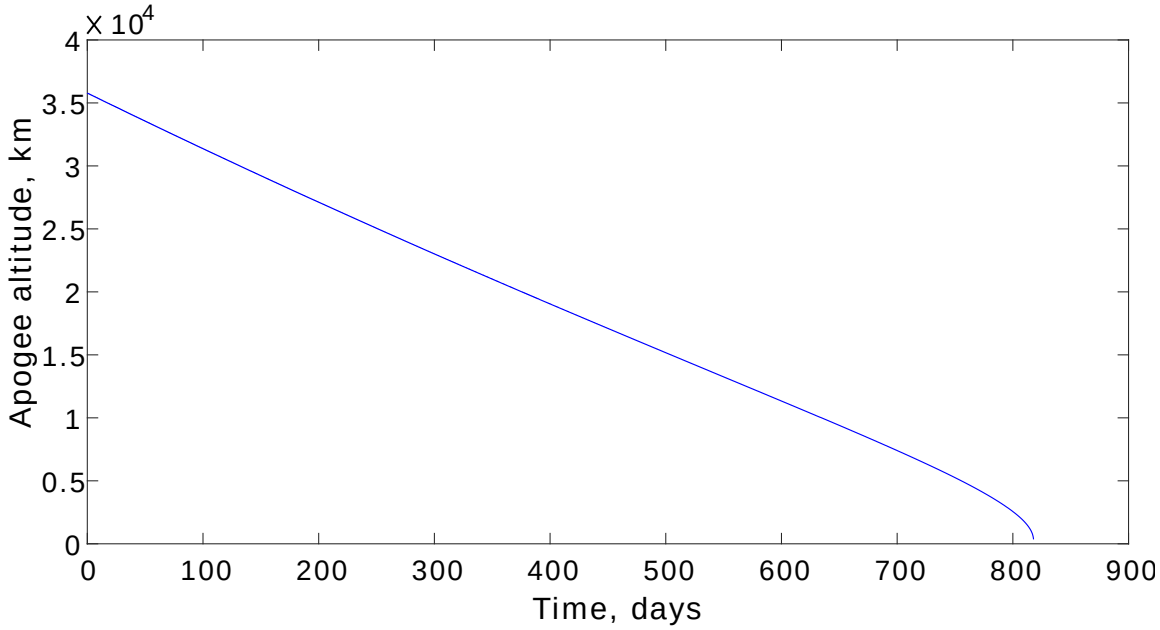

Figure 2.9: *Profile of apogee altitude during the entire deorbit of Sylda from the initial GTO orbit.*

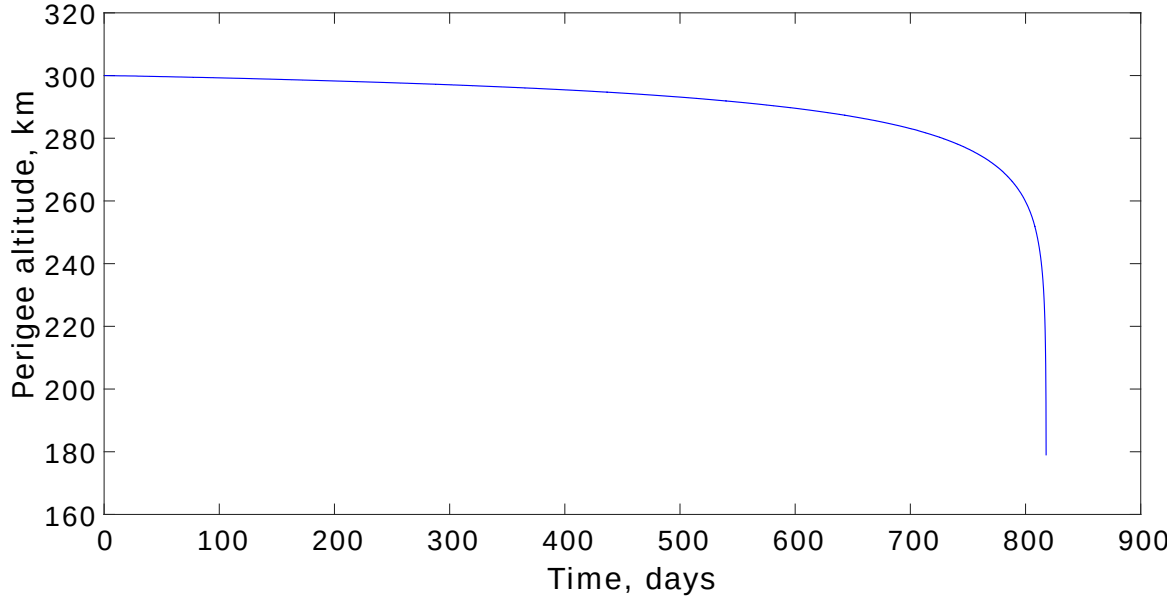

Figure 2.10: *Profile of perigee altitude of Sylda during the entire deorbit of Sylda from the initial GTO orbit.*

The apogee altitude profile is reasonable since it shows a constant decrease during the most of deorbit, with a steeper reduction at the end of deorbit due to the fact that in the last part of deorbit the system is always orbiting below 2000 km where drag perturbations are active as modeled in the codes, and is therefore constantly affected by orbital energy dissipation. Instead in the initial part of deorbit, the decrease in apogee altitude is created only during the time intervals of the passage of Sylda across the perigee region, below 2000 km. This is shown in Fig.2.11, where only the first 10 days of deorbit are displayed: the decrease in apogee altitude takes place step-by-step, non in a continuous manner. This is due to the fact that drag perturbations are active only below 2000 km and the system, in the first part of deorbit, is spending a time below that altitude on the order of 10–20% of the orbital period.

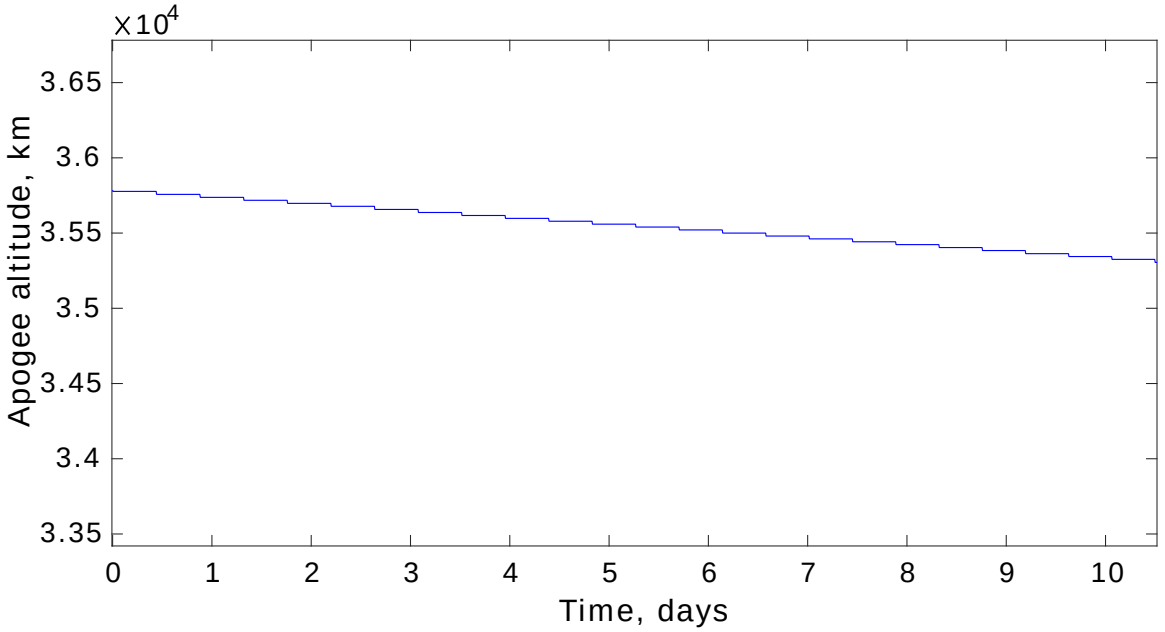

Figure 2.11: *Profile showing the evolution of the apogee altitude over the first 10 days of deorbit.*

The same observation can be done for the perigee altitude profile: in this case, it is also worth to point out that the perigee altitudes decreases much slower than the apogee altitude, until the much steeper reduction in the very last part of deorbit. All of this is proven by the fact that the orbital eccentricity is decreasing too during deorbit, as shown in Fig. 2.12, together with other significant orbital parameters.

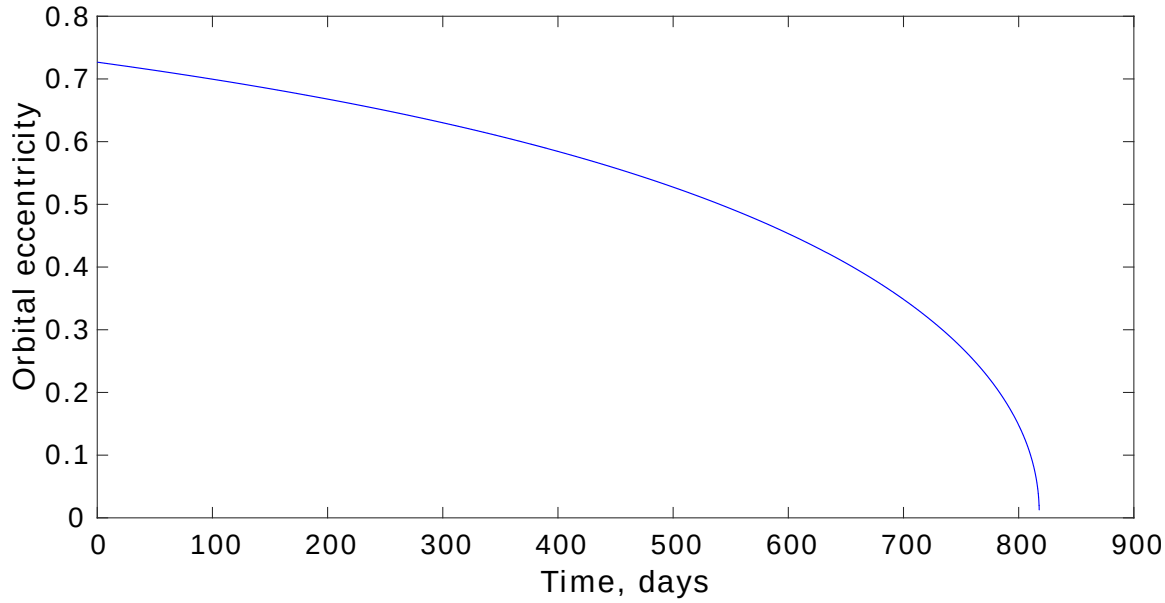

Figure 2.12: *Profile of orbital eccentricity during the entire deorbit of Sylda from the initial GTO orbit.*

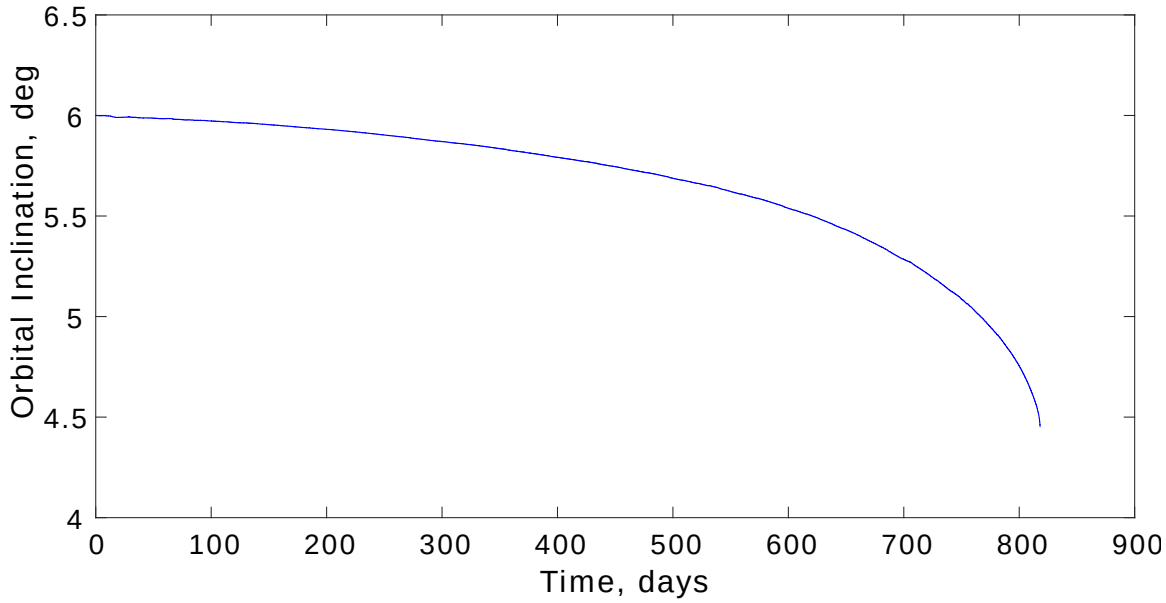

Figure 2.13: *Profile of orbital inclination during the entire deorbit of Sylda from the initial GTO orbit.*

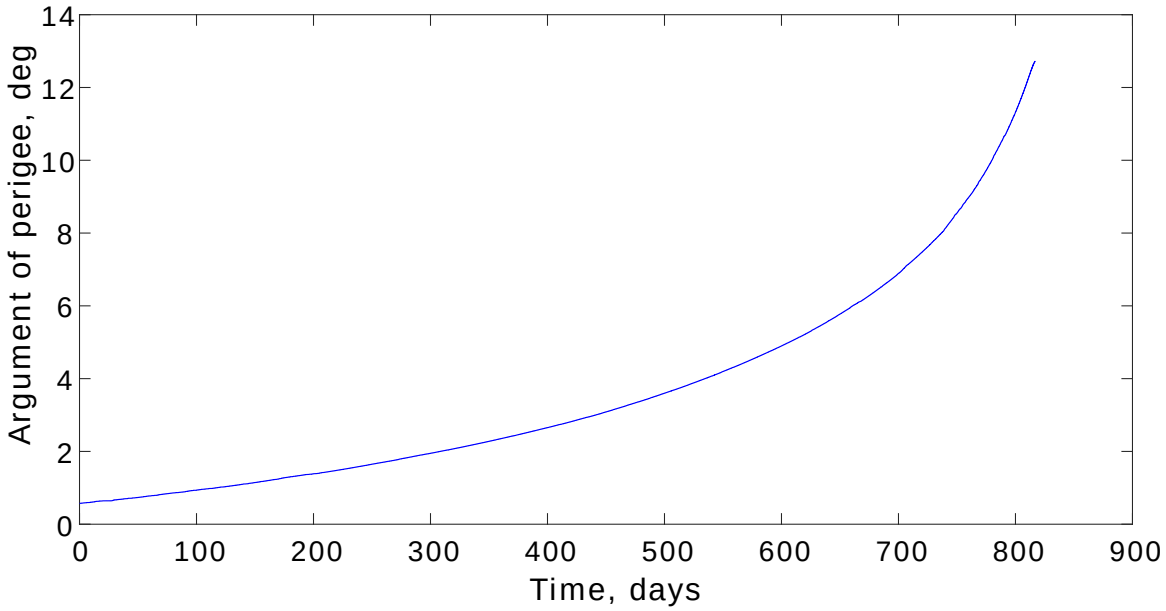

Figure 2.14: *Profile of argument of perigee during the entire deorbit of Sylda from the initial GTO orbit.*

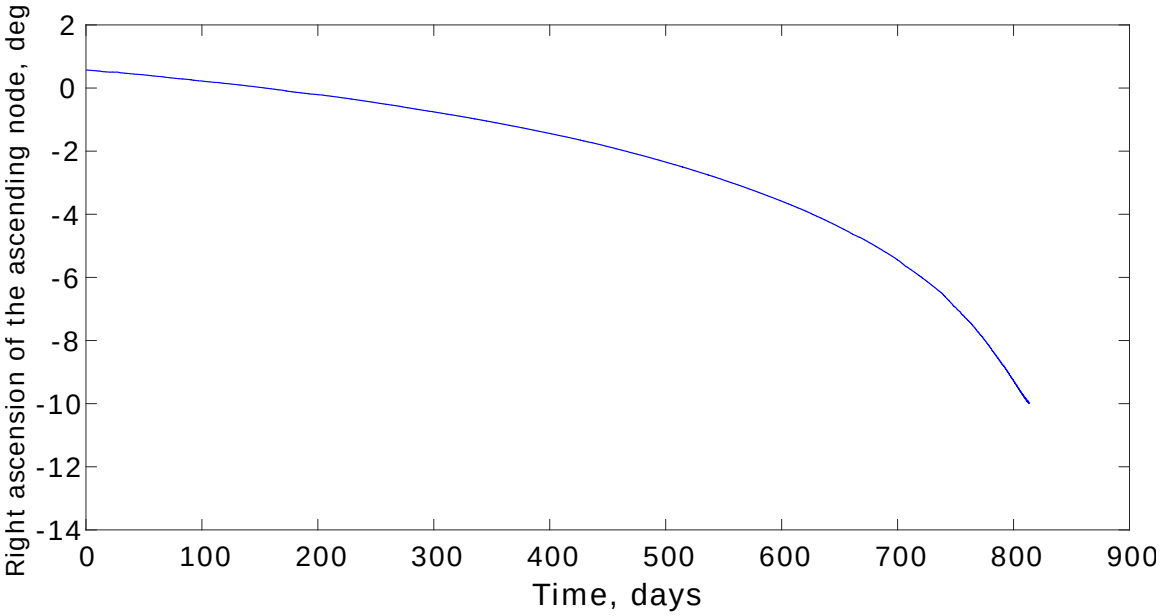

Figure 2.15: *Profile of right-ascension of the ascending node during the entire deorbit of Sylda from the initial GTO orbit.*

The system during deorbit is continuously rotating on the orbital plane, as expected from what reported in literature (e.g. Ref.[44]), and as demonstrated by the profile of the in-plane angle of the system, that is always increasing in magnitude over the entire deorbit as shown in the top Fig.2.16. The final angle, in magnitude, is about $4e+7$ degrees, which means that during the entire deorbit time, the system experienced an average of about 5–6 full rotations per hour. The bottom Fig.2.16 displays the profile of the out-of-plane angle of the tethered system during the entire deorbit, showing that this angle continuously oscillates but never exceeds a magnitude of 5 degrees: this is fundamental for the stability of the system, and demonstrates the fact that the out-of-plane dynamics is present but less relevant than the in-plane dynamics. This is then a confirmation that the analyses presented in Sec. 2.1, that were neclecting the out-of-plane dynamics in order to have a faster computational model to provide a set of information necessary to implement this second more accurate campaign of analyses, were relying on a reasonable assumption.

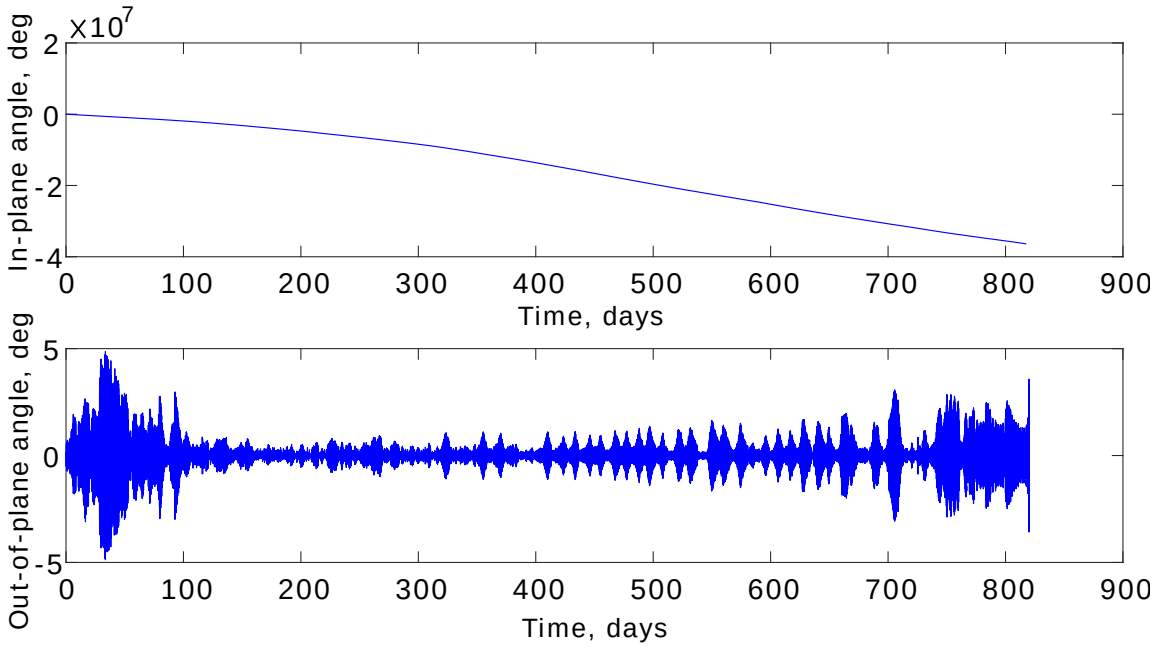

Figure 2.16: *Profile showing the evolution of the in-plane angle (on the top) and out-of-plane angle (on the bottom) of the tethered system during the entire deorbit.*

Another very important profile is the angular velocity on the orbital plane: as shown in Fig. 2.17, the angular velocity oscillates and varies in magnitude, reaching a maximum magnitude of approximately $0.013\,\mathrm{rad/s} \approx 0.7\,\mathrm{deg/s}$. It is important to note that this maximum angular velocity on the orbital plane is absolutely comparable with the angular velocity reached after 818 days with the analysis presented in Sec.2.1 and shown in Fig.2.4. In the present analysis, with respect to the previous nondimensional analysis, the out-of-plane dynamics interferes with the in-plane dynamics making the profile of in-plane angular velocity non-monotonically increasing, as it was in the case portrayed in Fig.2.4. Once again, the fact that the angular velocity does not change in sign over the entire deorbit ensures the avoidance of tether slackness and consequent instability. The tether can be then considered as always taut due to a positive tension created by the in-plane rotation around the system's center of mass. The value of maximum angular velocity is also lower than the maximum reached in the simulation presented in Sections 2.1.3 and 2.1.3, and therefore the results regarding tether tension presented in those Sections are still applicable. It is then possible to state that the maximum tension along the tether, also thanks to the butterfly configuration, is always below, and with a good safety margin, than the maximum allowed tension by tether material, especially when using a Fiber-Reinforced Aluminum. The tether segments are then demonstrated not to break during the entire deorbit.

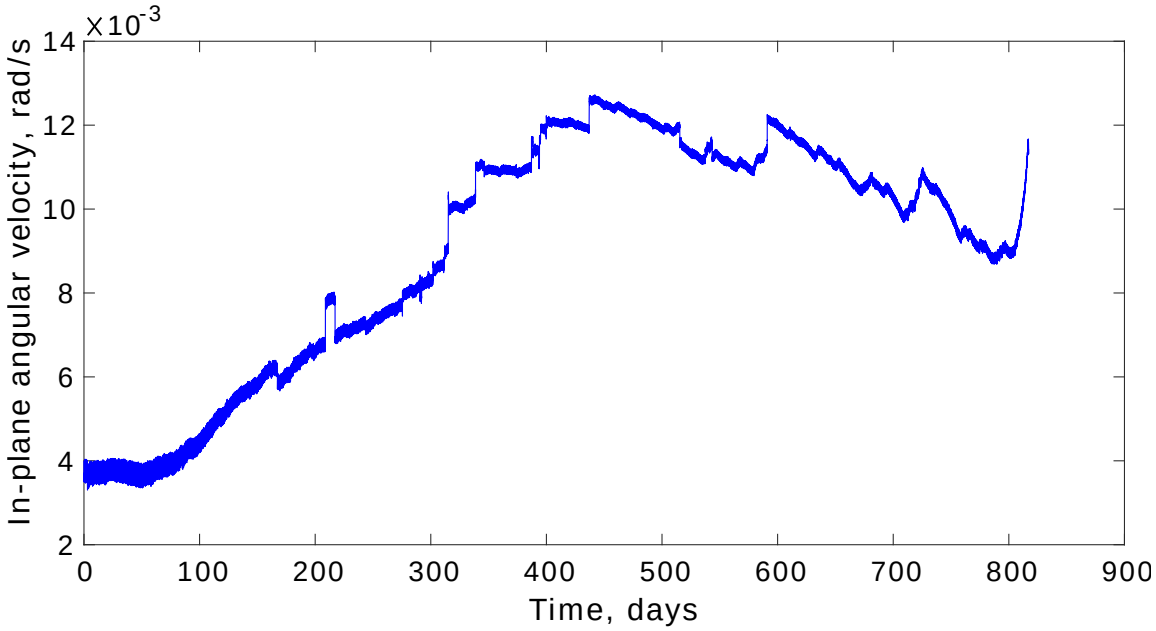

Figure 2.17: *Profile showing the evolution of the angular velocity of rotation of the tethered system around its center of mass, on the orbital plane, during the entire deorbit.*

The total time to deorbit Sylda, with this more accurate model used for this second campaign of analyses, turns out to be, as displayed in all the previous plots, about 818 days, i.e. about 2.24 years. This time is even lower than the deorbit time computed in the previous campaign of analyses, presented in Sec. 2.1.

Chapter 3

Analysis of Pre-Deorbit procedures

The present Chapter is focused on the analysis of the procedures to be performed between the release of Sylda in GTO and the actual start of deorbit, presented in Chapter 2, with fully deployed tethers. The deorbit system considered in this Chapter is the *butterfly* system, presented in Chapter 2, with a single tape-like bare electrodynamic tether (BET), divided in two segments deployed on opposite directions. Each segment of tether has a tip-mass at its end. The pre-deorbit procedures that are investigated here are:

1. *Detumbling* of Sylda: this is a procedure that must be performed before deploying the tethers, and has the aim of zeroing or minimizing the residual angular velocities of rotation of Sylda. At the end of this procedure, Sylda is inertially still and the subsequent phase of deployment can start.
2. *Deployment* of the two tether segments: deployment is performed on the orbital plane, and different analyses are presented in this Chapter, with the objective of finding optimal deployment parameters, such as the location along the orbit where it is most convenient to perform it.

3.1 Tether storage and deployment hardware

At first, a brief overview at the necessary hardware for the deorbit system is presented in this Section.

The most promising solution for the storage of the tape tether used in this research, it is to have each segment of tether stored in a dedicated box, with the tether reeled up around a drum wheel, similarly to what shown in Fig. 3.1. The two boxes are then electrically connected in order to create a single electrodynamic tether, but subdivided in two segment deployed on opposite directions.

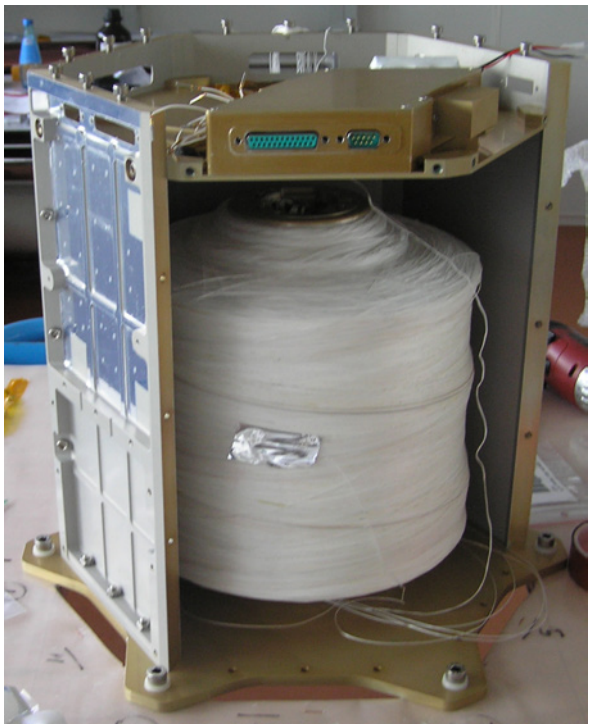

Figure 3.1: *The tether storage box and deployer used in YES2 mission, where a tether of length* 30 km *and* 0.5 mm *diameter was used. In the case presented in this thesis, a tether of length on the order of* 1 km *is used, and with tape-like shape (width of* 3 cm *and thickness of* 100 μm*): therefore, the spool is surely much smaller than this one. Photo courtesy of ESA.*

The two boxes, each one storing one of the two segments of bare electrodynamic tether, are mounted on the upper tronco-conical part of Sylda, where there is the largest clearance between Sylda and the walls of the fairing of the launch system where Sylda is used. In order to minimize the displacements of the launch system's center of mass along the radial direction, the two storage boxes must be placed in axialsymmetrically opposite locations, and have a mass as equal as possible. Fig. 3.2 shows the mounting of a single storage box on Sylda, whereas the other box is mounted in the simmetrically opposite location (hidden in the picture by Sylda's body).

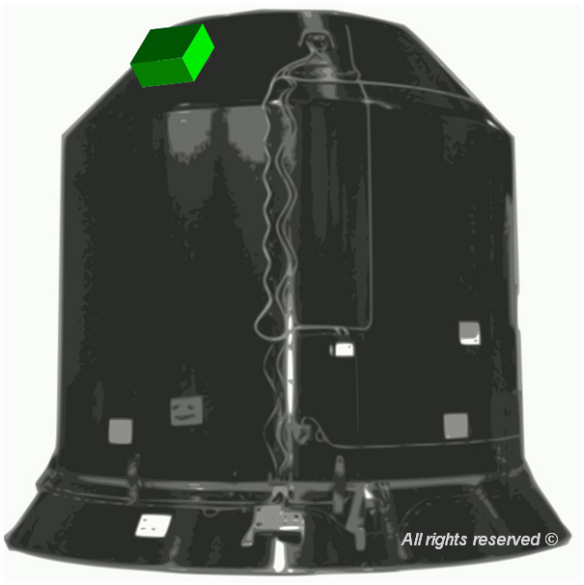

Figure 3.2: *Sylda with tetherbox mounted*

Each storage box also contains the tip-mass attached to the tether end that goes towards space, and a dedicated electrical motor powered by a small primary battery to be used only for deployment. The electrical motor is used to control the rotation of the reel and to follow a prescribed tether release velocity profile, as will be discussed in the following Sections.

The tip-mass of one tether segment, the shorter one, is made of a hollow cathode equipped with a small tank of ionization propellant, to be used for ejecting electrons back to space, such as the one shown in Fig.1.11. The tip-mass of the other tether segment is a ballast mass, possibly housing components that are needed during the deployment or the orbit procedure.

3.2 Detumbling of Sylda

In order for the deployment to take place correctly, without risk of interference between the tether and Sylda's body, Sylda must be detumbled, i.e. the residual rotation of Sylda must be zeroed or consistently attenuated. In fact, Sylda, after its release in GTO, it rotates around its center of mass on the three body-frame axes. This is due to the error of Sylda's release system, before the insertion of the dual payload in GEO, e.g. from disalignment or different separation impulses of the release springs or pyros. An estimate of this angular velocity of rotation, along the three axes, is $\pm 0.35\,\mathrm{deg/s} \approx 0.006\,\mathrm{rad/s}$ (Ref.[5]). This can be regarded as the error rate on Sylda's attitude on the three axes.

The detumbling procedure consists then in decreasing to zero these angular velocities along the three body axes. Detumbling can be implemented, in a robust manner, by using *magnetic torquers*, placed on Sylda's outer walls, in order to create a torque

that compensates and zeroes the rotational velocity around the three body axes, i.e. the transversal axes $\hat{u}_\xi$ and $\hat{u}_\eta$, and the longitudinal axis of Sylda $\hat{u}_\zeta$ (see Appendix B). The detumbling is performed such that, when deployment starts, the tethers are deployed on the orbital plane, and Sylda's longitudinal axis is tangential to the orbit. This attitude at which deployment can start is shown in Fig. 3.7.

Active magnetic torquers are an effective candidate for detumbling: essentially, they are slender cylinders of small diameters (on the order of 2-3 cm and various lengths depending on the torque that is needed. They have a very low mass with respect to Sylda, they are simple (and relatively cheap), and require only a very low amount of power that can be supplied by dedicated small primary batteries embedded inside. These torquers are made of a cylindrical coil that creates a magnetic moment along its axis: the interaction of this magnetic moment with the Earth's magnetic field generates a torque acting on the magnetic torquer and then transmitted to the body where the torquer is mounted. Due to their shape, magnetic torquers can be easily integrated on the outer walls of Sylda.
For example, the company *Cayuga Astronautics* manufactures torquers of various sizes, with the largest and most powerful one being approximately 1.5 m long, very slender (very low diameter), and requiring a power of about 6 W. Such torquer is capable of generating, at LEO altitudes where the Earth's B-field ranges from 0.2 to 0.5 Gauss (20 to 50 micro-Tesla) a magnetic moment of 800 Am^2 and torques between approximately 0.016 to 0.040 Nm. Some torquers manufactured by *Cayuga Astronautics* are shown below.

Figure 3.3: *Magnetic torquers of different lengths for space applications. Photo courtesy of* Cayuga Astronautics.

The active coil of the torquer is powered by a very small current, used to generate a magnetic moment $\boldsymbol{m}_m$, that can be then controlled by regulating the current supplied to the coil. The resulting magnetic moment is calculated as follows:

$$\boldsymbol{m}_m = i_c \Sigma N \hat{\boldsymbol{n}} \tag{3.1}$$

where i_c is the current circulating along the coil, N the number of turns along the coil, Σ the area enclosed by a single turn of coil. The magnetic moment is directed along $\hat{\boldsymbol{n}}$

that is the unit vector along the longitudinal axis of the cylindrical coil, i.e. orthogonal to the plane of the single turn of coil. The mechanical torque that is generated, and transmitted to Sylda, can be computed as (Ref.[26]):

$$\boldsymbol{M_m} = \boldsymbol{m_m} \times \boldsymbol{B} \tag{3.2}$$

where $\boldsymbol{B}$ is the external magnetic induction in *tesla* (in this case, the Earth's magnetic induction). This means that the torque created on Sylda is orthogonal to both the longitudinal axis of the magnetic torquer, and to the local magnetic field vector $\boldsymbol{B}$.

For detumbling the satellite along the X_B and Y_B body axes (of unit vectors respectively $\hat{u}_\xi$ and $\hat{u}_\eta$, a pair of magnetic torquers can be mounted on the outer walls of the cylindrical part of Sylda, with axis parallel to the longitudinal axis of Sylda. This means that the magnetic moment will be always directed along the third axis Z_B of the body frame (unit vector $\hat{u}_\zeta$). Each torquer is mounted in correspondence of the intersection of the body axes X_B and Y_B with the cylindrical body of Sylda, as shown in Fig.3.4. The torquers for detumbling along Z_B are discussed later.

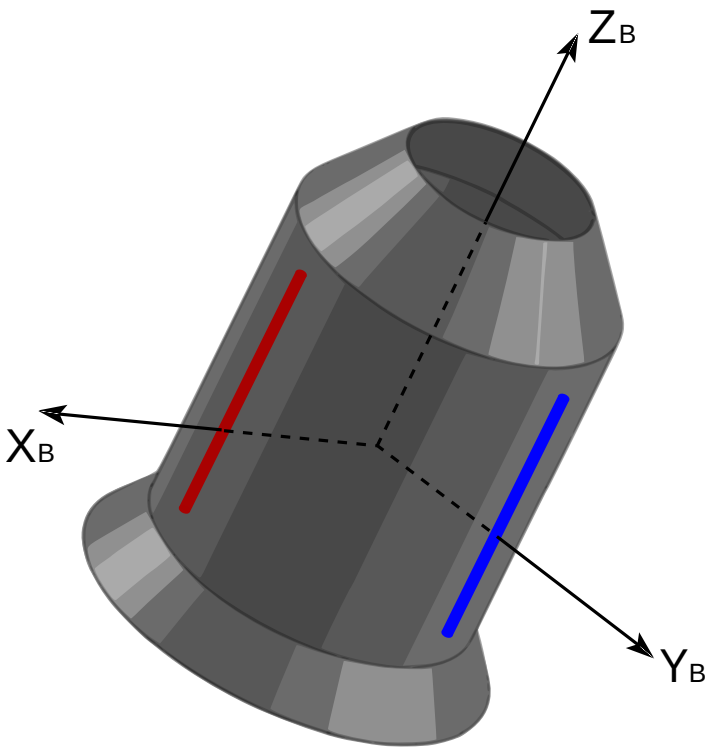

Figure 3.4: *View of Sylda with magnetic torquers mounted with axis along the longitudinal axis of Sylda, and in quadrature between each other. The mounting points are taken in correspondence to the body axes X_B and Y_B.*

Figure 3.5 represents the action of the magnetic torquer mounted in correspondence to the body axis X_B, when Sylda is at the perigee of the initial GTO orbit. For a simpler visualization, the geomagnetic field is approximated here as a dipolar field.

The dipolar geomagnetic field has its North pole nearby the geographic South pole, as portrayed in Fig.D.1 in Appendix D.1, and the axis of the dipolar geomagnetic field is tilted of about 11° with respect to the spin (geographical) axis of the Earth. Sylda is released on a prograde GTO orbit of inclination about 6°. It is then reasonable to approximate the $\boldsymbol{B}$ vector as orthogonal to the orbital plane during the detumbling phase. Consequently, when viewing the orbital plane from the top (i.e. from magnetic south towards the magnetic north) the vectors would be as displayed in Fig.3.5.

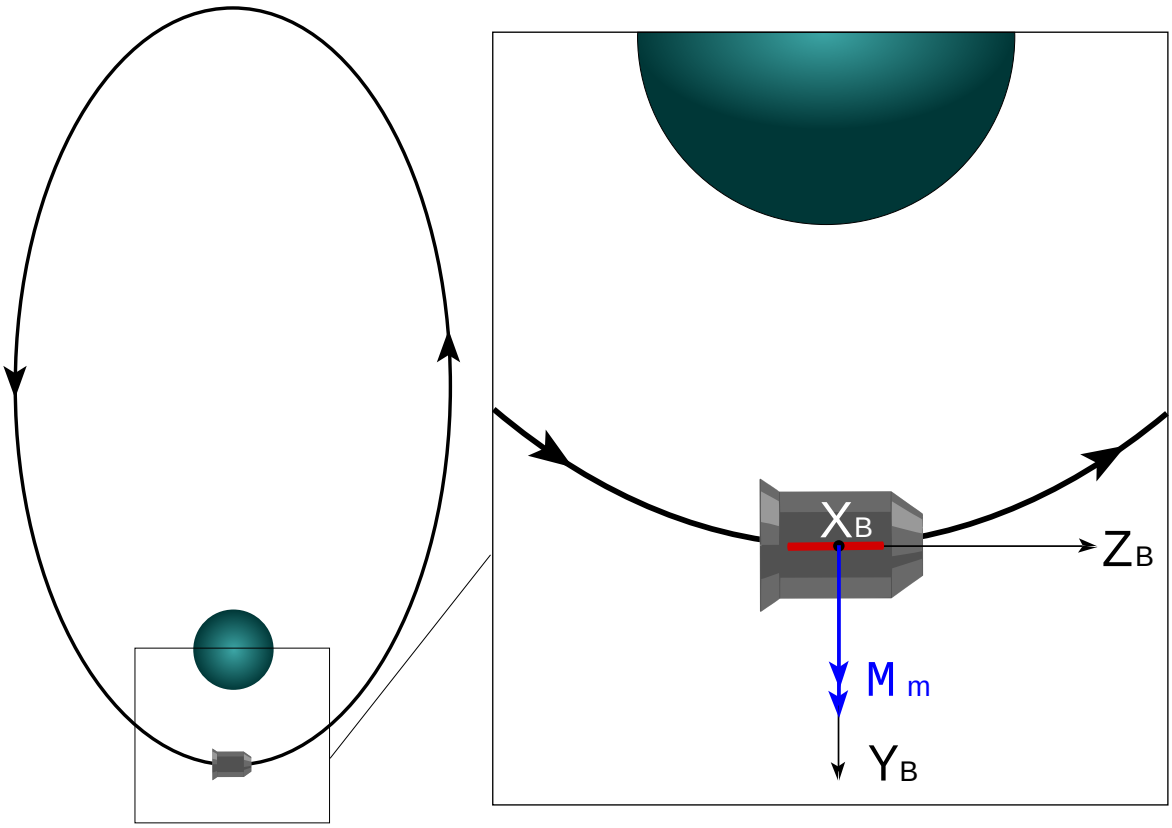

Figure 3.5: *One the left: view of Sylda at the perigee of the initial GTO. On the right: close view showing the torque $\boldsymbol{M}_m$ along the axis Y_B created by the magnetic torquer placed in correspondence of the X_B axis exiting from the plane, as well as the geomagnetic induction $\boldsymbol{B}$. The magnetic moment $\boldsymbol{m}_m$ of this torquer is directed along Z_B.*

The selection of the torquer is dependent on the time of duration of the detumbling procedure. The designer can set the time to detumble and then find out the size of the torquer that is needed to detumble Sylda in that prescribed time. The opposite approach can be followed too: a torquer of a certain size is chosen, and how many to mount on Sylda. Once this is set, the time to detumble is calculated. Hereby, this second approach is followed, using the torquer model described before, i.e. the torquer of length 1.5 m and magnetic moment of 800 Am^2.
The moment of inertia of the system is constant over time, since the tethers are not being deployed yet. The three body axes can be treated as principal axes of inertia, and the Euler equations can then be adopted for simulating the detumbling.

The inertia matrix of Sylda is:

$$[I_S] = \begin{bmatrix} A & 0 & 0 \\ 0 & B & 0 \\ 0 & 0 & C \end{bmatrix} \tag{3.3}$$

and the system of Euler equations, on the body-frame axes, is:

$$M_{m,\xi} = A\ddot{\alpha}_\xi + (C - B)\dot{\alpha}_\xi^2 \tag{3.4}$$
$$M_{m,\eta} = B\ddot{\alpha}_\eta + (A - C)\dot{\alpha}_\eta^2 \tag{3.5}$$
$$M_{m,\zeta} = C\ddot{\alpha}_\zeta \tag{3.6}$$

where $\ddot{\alpha}_\xi$, $\ddot{\alpha}_\eta$, $\ddot{\alpha}_\zeta$ are the angular accelerations of Sylda around the three body axes, and $\dot{\alpha}_\xi$, $\dot{\alpha}_\eta$, $\dot{\alpha}_\zeta$ the angular velocities. $M_{m,\xi}$ and $M_{m,\eta}$ are the moments created by the magnetic torquers on the two transversal axes. $M_{m,\zeta}$ is the moment about the longitudinal axis. The initial condition on angular velocities is: $\dot{\alpha}_{0,\xi} = \dot{\alpha}_{0,\eta} = \dot{\alpha}_{0,\zeta} = 0.006\,\text{rad/s}$. The moments of inertia about the transversal axes are the same, i.e. $A = B$, but C is different from A and B. The first two equations are simplified by approximating $C \approx A = B$ and called J_S, becoming:

$$M_{m,\xi} = J_S\ddot{\alpha}_\xi \tag{3.7}$$
$$M_{m,\eta} = J_S\ddot{\alpha}_\eta \tag{3.8}$$

The torque created by the magnetic torquers is variable over time, depending on the local geomagnetic induction $\boldsymbol{B}$, but an average value can be used considering the torquers to be activated on at LEO altitudes where the magnetic field is stronger. This value is averaged over the time of passage below 1500 km, between a maximum and minimum value of torque (data provided by the manufacturer's brochure) in that range. This average value is kept constant over the time spent below 1500 km and denoted as $M_{m,av}$. The 1.5 m long torquer manufactured by *Cayuga Astronautics*, reports values of torque, generated at LEO altitudes, in the range between a minimum of 0.016 Nm and a maximum of 0.040 Nm. The average value is then estimated as $M_{m,av} = 0.028\,\text{Nm}$.
The moments of inertia are constant over time and on all axes. Therefore, with all the assumptions that are made, only one equation needs to be solved in order to find the time it takes for the magnetic torquer to zero the angular velocity on each axis:

$$\ddot{\alpha} = \frac{0 - \dot{\alpha}_0}{\Delta t} = \frac{M_{m,av}}{J_S} \tag{3.9}$$

leading to the time to detumble:

$$\Delta t = \frac{-J_S\dot{\alpha}_0}{M_{m,av}} \tag{3.10}$$

where $M_{m,av}$ is negative (the torque by the magnetic torque must counteract the rotation).

Being magnetic torquers most effective at low altitudes, the detumbling procedure is activated during the first passage of Sylda across the perigee zone after its release in GTO. From calculations, it turns out that the time spent by Sylda, in its initial GTO orbit, below 1500 km of altitude is about 22 minutes. Using a single magnetic torquer presented earlier, it turns out from calculations that a time of about 12 minutes is needed to detumble along a transversal axis and about 9 minutes to detumble about the longitudinal axis, about which the moment of inertia is lower. This means that during the first passage through perigee, Sylda can be completely detumbled.

Given that the action of magnetic torquers depends on the attitude of the torquers with respect to magnetic field lines, two 1.5 m torquers are used for detumbling about transversal axes, as stated earlier and shown in Fig.3.4. Instead, for detumbling about the longitudinal axis Z_B, the torquers must be placed on the upper conical part of Sylda, with their axis that is orthogonal to Z_B as shown in Fig.3.6. In this case, using a 1.5 m long torquer might pose problems due to the restricted available space for mounting. It is then preferable, instead of a couple of 1.5 m long torquers, to have four smaller torquers, of length 0.75 m each, that are mounted axial-symmetrically.

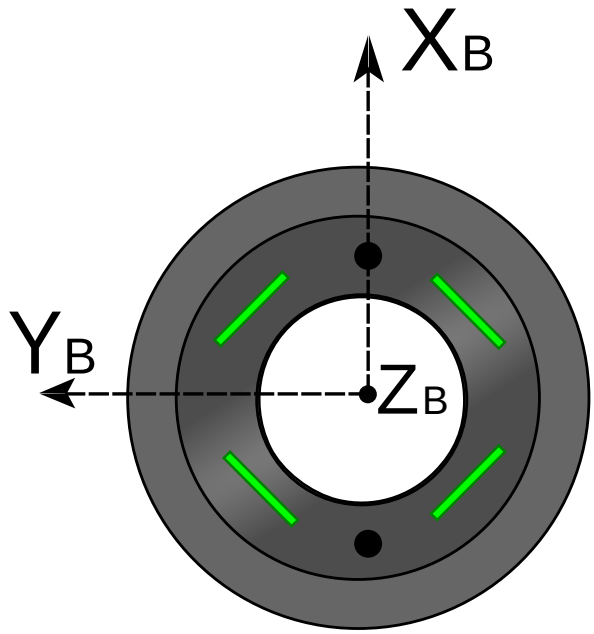

Figure 3.6: *Sylda viewed from the top showing the four magnetic torquers, of length* 0.75 m *each, used to despin Sylda around the longitudinal axis Z_B. The torquers are placed axial-symmetrically, in order to minimize the displacement of center of mass of the launch system where Sylda is mounted.*

At last, it is important to note that, after detumbling with the magnetic torquers during the first passage in the perigee zone, an additional residual detumbling, only

along the longitudinal axis Z_B could be provided by the tethers themselves with their tip-masses at each end, in the very first stage of deployment.
In fact, the tethers projection on the plane orthogonal to the longitudinal axis creates a *yo-yo despin* configuration, that is often employed in space applications (Ref.[16]). The only difference from the usual *yo-yo despin* is that in this case the tethers are of course not seized after the despinning process is complete.

As deployment starts, the two tethers are released with a certain angle with respect to first body frame axis X_B, as shown in Fig. 3.7. The projection of the two tethers along X_B is responsible of an increase the total moment of inertia of the system about the Z_B axis, determining a decrease in angular velocity of Sylda about that same axis. The deployment of the two tethers takes place nominally on the orbital plane: in order to achieve this the magnetic torquers that detumble Sylda about Z_B must be programmed such that the zero angular velocity about Z_B is achieved when X_B lies on the orbital plane. This goal can be helped by the yo-yo despin, that zeroes any residual angular velocity due to the possible error in the action of magnetic torquers, leading to a robust detumbling system.

In any *yo-yo despin* process, the released length of the two tethers after which despin is complete, it is independent from the initial angular velocity, as reported in Ref.[16]. From calculations, it turns out that after approximately 14.13 m of released length of tethers projected along X_B, with tip-masses of 5 kg at each end, Sylda is completely despun along the longitudinal axis. This required length for complete despin is computed as (Ref.[16]):

$$L_{yy} = R(\sqrt{K} - 1) \tag{3.11}$$

where $R = 2.25\,\text{m}$ is the radius of Sylda's cylindrical body, and K is defined as:

$$K = 1 + \frac{C}{m_{yy}R^2} \tag{3.12}$$

where C is the moment of inertia of Sylda around the longitudinal axis Z_B, and $m_{yy} = m_A + m_C$ the sum of the two masses at the end of each yo-yo segment (i.e. the two BET tether segments, and the two masses being the anodic and cathodic tip-mass). Accounting that tethers are generally released with an angle of 30°–45° with respect to X_B, the projection of the tether along X_B is responsible for the yo-yo despin, as already stated. Consequently, the actual tether length to despin is about 20 m, for each of the two tethers, when using a deployment angle of 45°.

Any deployment simulation described in the following sections is performed as starting after this first stage of tether release, where residual yo-yo despin an take place, i.e. with the system completely detumbled an initial length of 20 m of both tethers. In order to be conservative, an initial nonzero angular velocity for Sylda is kept only around the axis orthogonal to the orbital plane (i.e. the body axis Y_B), i.e. a residual angular

velocity of 0.0006 rad/s, that is 1/10 of the pre-detumling angular velocity of Sylda (that is 0.006 rad/s). For the reasons described before, the out-of-plane motion can be assumed negligible during deployment: thus, all deployment simulations account only for the motion of the system on the orbital plane.

3.3 Deployment strategy and control

Sylda is released at the apogee of the GTO orbit and it rotates about the three body frame axes with the angular velocity estimated as 0.006 rad/s, as reported earlier. Then, as it approaches for the first time the perigee of the GTO, the magnetic torquers start to work most efficiently below 1500 km, and they are used, during the time of first passage through the perigee to detumble Sylda around the three body-frame axes, as described in Sec.3.2.

The deployment can theoretically take place anywhere along the initial GTO orbit of Sylda, anytime after detumbling is complete, i.e. not before the first passage through the perigee zone. In the following sections different analyses of deployment are performed in order to understand the dynamics during the deployment of the two tether segments, and to estimate, from the results obtained, the most convenient location along the initial GTO orbit where to start deploying.

In any case of deployment presented in this Chapter, a *quasi-uniform* tether release velocity profile is used for the two tethers: this means to have a constant tether release velocity $\dot{l} = \dot{l_0}$ until a certain released length L_{unif} and then a decreasing release velocity, with zero tangent (i.e. zero release acceleration) both at the beginning of the decrease, and at the end of tether release.
The release velocity reaches zero, and with zero tangent, at the end of deployment, in order to prevent a mechanical shock that could break the tether. The release velocity should not be too high in order to avoid losing tether tension, with consequent instability and slackness of the tether. Generally, tether release velocities lower than 2 m/s are used, as reported for example in Ref.[51].

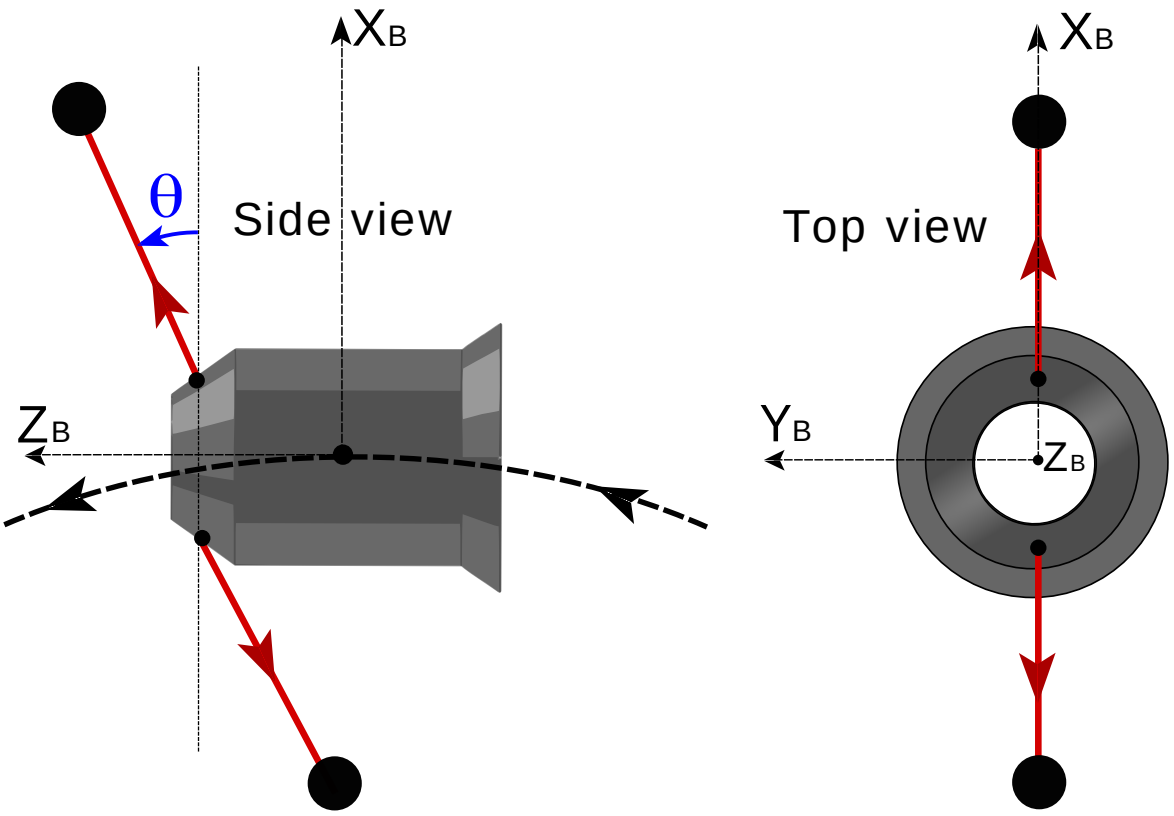

Figure 3.7: *Sylda during the first instants of deployment on the orbital plane. The longitudinal axis Z_B should be possibly aligned with the tangent to the orbit, and the tethers are deployed with a prescribed initial angle with respect to the axis X_B.*

The control of the tether dynamics during deployment is implemented by regulating the tether release velocity with the electrical motor that rotates the spool around which the tether is reeled. It is then a rate control on tether release that ensures a positive tension along the tethers throughout deployment, in order to avoid instability and slackness. The electrical motor, powered with a small primary battery, is programmed with the nominal release velocity profile, but also capable of error compensation by using the feedback from a vision system used for tether's attitude detection (described in detail in Chapter 4). This vision system is designed to track each tip-mass: an error in the position of the tip-mass is then used by the electrical motor to accordingly modify the release velocity. The aim is to reach, at the end of deployment, or soon after the end of deployment, a taut stable configuration for the two tethers segments. In this configurations the tethers are straight and aligned with the first boxy axis X_B, that is also the optical axis of the vision system, and the system of Sylda and the two tethers would eventually move as a whole, approximately as a single rigid body.
After this stabilized configuration is reached, with tethers fully deployed, the deorbit procedure, presented in Chapter 2, can start with the system reasonably modeled as a dumbbell, since it moves approximately as a single rigid body.
In order to achieve this condition, Sylda's rotation angle α and velocity $\dot{\alpha}$ must respectively tend towards being equal to the angle $\theta_1 = \theta_2 - \pi$ and angular velocity $\dot{\theta}_1 = \dot{\theta}_2$ of the two tethers. More details will be provided in the following sections.

3.4 Simulation of BET deployment from Sylda nearby its apogee

In this Section, an analysis of deployment of the two tether segments is presented, starting from the apogee of the initial GTO orbit. This means that Sylda, after its release, is detumbled during the first passage in the perigee zone, and then travels back to the apogee where the deployment is started. At apogee of the GTO, the altitude is so high that electrodynamic and aerodynamic drag perturbations are absent; the deployment can be then simulated without the contribution of drag perturbations. The dynamics of the system is then only affected by the gravitational field, not by other external perturbations. It is desidered to achieve, at the end of the deployment a sufficient angular velocity of rotation of the system as a whole, in order to prevent tether instability. At the same time, this angular velocity should not be too high in order to avoid excessive increases in tether tension and related risk of tether breaking, as described in Sec.2.1.

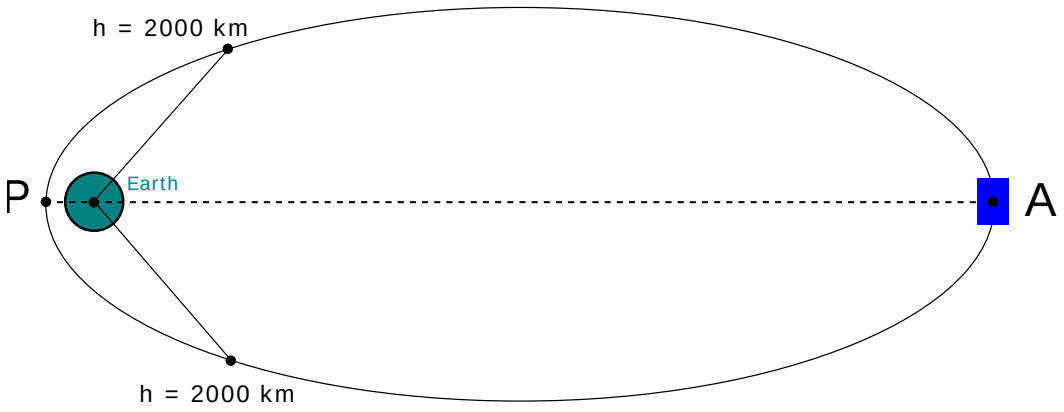

Figure 3.8: *Sylda in GTO orbit at apogee when deployment starts*

3.4.1 Description of the model

The model simulates a double-tether deployment that takes place only on the orbital plane. Such type of deployment was actually performed in previous missions with tethers, such as TSS-1, TSS-1R, SEDS1, SEDS2 and YES2 [23]. Out-of-plane motion is then neglected in this analysis as irrelevant. The deorbit system used for deployment simulation is made of *Sylda*, i.e. the deorbit target, and two bare electrodynamic tethers (BETs) as deorbit device, in *butterfly* configuration. The tethers are stored in separate boxes attached to the upper conical part of Sylda, as described in Sec.3.1. In numerical simulations, the dynamics of the two tethers is separated from the dynamics of Sylda. There is a hollow cathode attached to Sylda for ejections of electrons captured by the electrodynamic tethers; at the free end of each tether, there is a tip-mass of 10 kg. The two tethers used for deployment simulation are identical and have a length of 1 km, width of 3 cm, thickness of 100 μm. The material used for both tethers is *Metpreg* fiber reinforced Aluminum, with density of 3320 kg/m^3.

The deployment starts at the apogee of the GTO orbit, with apogee altitude equal to

GEO altitude; perigee altitude of 300 km; resulting eccentricity of 0.727. The inclination of the initial orbit is roughly 6°. The deployment takes a time lower than the orbital time needed for the object to arrive below 2000 km above the Earth's surface. At such high altitudes, the main perturbation forces, i.e. electrodynamic and aerodynamic drag, are negligible. Other minor perturbing forces, such as solar pressure or gravitational perturbations from higher order terms, they are neglected in this analysis. Therefore, in deployment simulations, the system's center of mass is reasonably assumed to move along an unperturbed GTO orbit throughout the deployment, with Keplerian motion. Consequently, the equations used in the model do not include external perturbation forces. The Coriolis forces create a deflection of the tether, that is not modeled here.

The specific configuration of *Sylda* used in computations has these features: diameter of 4.5 m, height of 6.8 m, and wall thickness of 3 cm; its mass is approximately $m_s = 536$ kg. Refer to 1.3.1 for more details about Sylda.

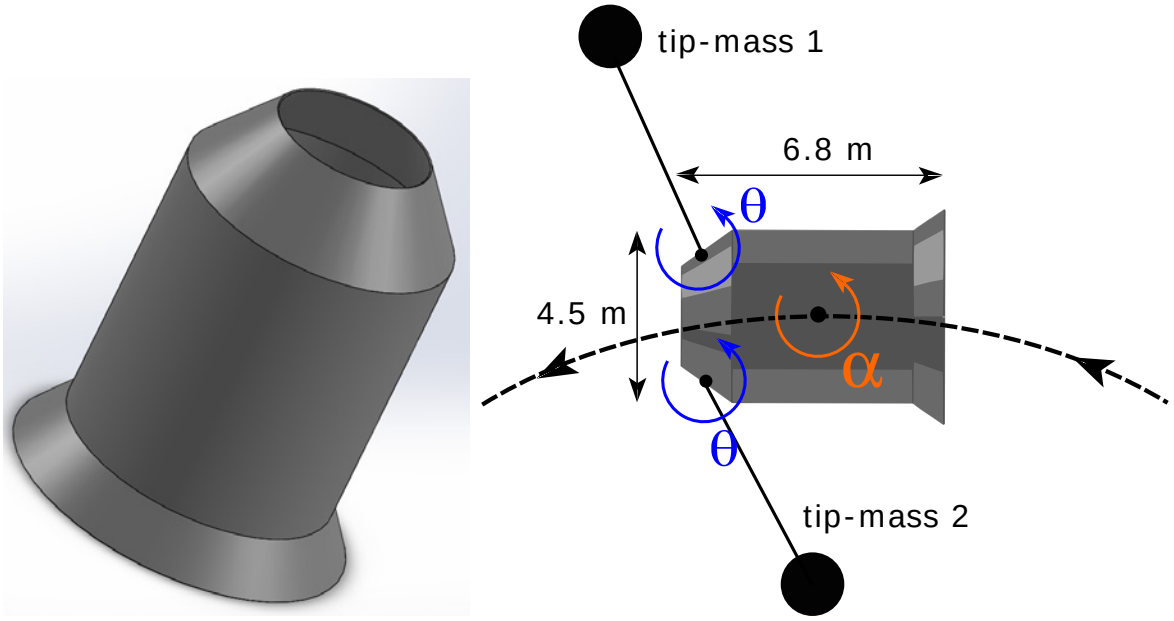

(a) Sylda *3D model in* Solidworks **(b)** Sylda *with deorbit system*

Figure 3.9: *Views of Sylda and deorbit system*

Each tether is modeled as a single dumbbell with a point mass at each end: at one end there is Sylda point mass m_S; at the other end, for the first tether the tip-mass m_1, and for the second the tip-mass m_2. The tethers are considered rigid and inextensible. Hence, the tethers in this model can have only a pendulum motion about Sylda, that in turn can rotate with respect to the tethers.

In order to comply with requirements at the end of deployment the two tethers can have different lengths and different deployment velocity. However, for a first analysis, the two tethers can be assumed identical and with the same release velocity profile. With

this assumption, the two tip-masses show the same motion profile during deployment, with the only difference of being symmetrically opposite. Consequently, only the profile for one tip-mass is needed to provide all the necessary information. The spatial coordinates of the tip-mass are computed relative to the body frame fixed to *Sylda*, and the vision system discussed in Chapter 4, and co-moving with it. Equations for the numerical model are developed starting from equations reported by Ref. [8]. The mass of Sylda is much higher than the mass of the two tether segments and of the respective tip-masses. The system's center of mass, in this case of symmetrical system of identical tethers, can be then considered coincident with the center of mass of Sylda, or with Sylda point mass m_S.

3.4.2 Tether release velocity profile

Deployment simulations start with a nonzero separation between the tip mass and Sylda, in order to prevent singularities, and with a nonzero relative velocity between them. The tethers are both deployed with constant release velocity $\dot{l} = \dot{l_0}$ (a value of 1.8 m/s is used) until a certain time t_{unif}, and then following a decreasing profile with zero tangent both at t_{unif} and at the end of deployment, terminating with zero release velocity in order to prevent a mechanical shock. Refer to Fig.4.1.

The Matlab code builds the deployment velocity profile in two steps. The user sets the total length of the tether, the value of $\dot{l_0}$, and a coefficient k that sets the ratio between the total time of deployment t_{tot} and time of deployment with uniform release velocity t_{unif}. From the beginning of deployment simulation until time t_{unif} the tether is deployed from the initial released length $L_0 = 0.1\,\mathrm{m}$ (a nonzero value is used to avoid singularities) until L_{unif}:

$$k = \frac{t_{tot}}{t_{unif}} \tag{3.13}$$

The code then computes, given k and $\dot{l}_{unif}$, the deployed length at which the release velocity starts to be decreased, in order to finish the deployment with zero release velocity.

After the tether surpassed this released length threshold, i.e. for $l > L_{unif}$ the deployment velocity is computed as:

$$\dot{l} = \dot{l_0}\frac{(cos(\zeta) + 1)}{2} \tag{3.14}$$

where

$$\zeta = \pi\frac{t - t_{unif}}{t_{tot} - t_{unif}} \tag{3.15}$$

The resulting profile of tether release velocity throughout deployment is shown in Fig.4.1.

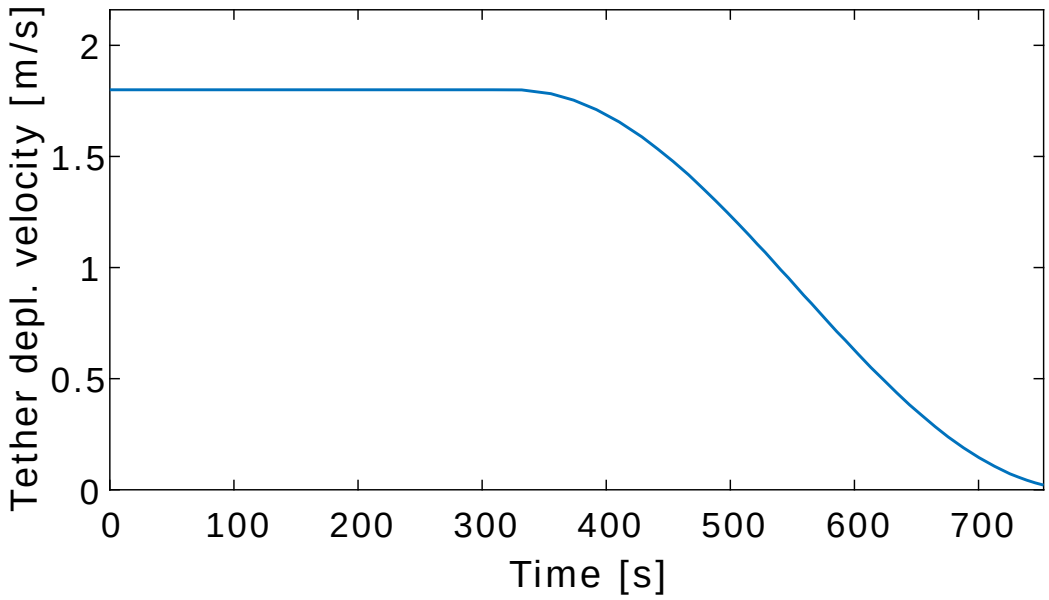

Figure 3.10: *Profile of tether release velocity*

3.4.3 Equations of numerical model and outputs

In order to accurately simulate the deployment, the tethers rotation is separated from the local rotation of *Sylda*. Both rotations of tethers and Sylda are measured with respect to the orbital frame centered on the system's center of mass. The unit vectors of the orbital frame are: $\hat{u}_r$, i.e. the radial direction pointing spaceward; $\hat{u}_w$ is the direction orthogonal to the orbital plane and directed as the orbital angular velocity, and $\hat{u}_v$ completes the right-hand orthonormal triad. In-plane angles are measured as positive when following the prograde orbital motion, otherwise negative.

The two tethers, treated as rigid oscillating dumbbells, rotate about their attachment hinge to Sylda with angles θ_1 and θ_2 with respect to $\hat{u}_r$. When considering also out-of-plane dynamics, the two tethers have also independent out-of-plane angles. Here, the deployment is assumed to take place on the orbital plane and the tethers are considered identical and deployed along symmetrically opposite directions: therefore, only one tether is considered for deployment analysis, computing the profile $\theta_1 = \theta$, and then obtaining also the profile for the second tether as $\theta_2 = \theta + \pi$. The initial angle of the tether, θ_0, is set to a very low nonzero value to prevent singularities.

The rotation of Sylda is described by the angle α, that is the angle of rotation of the body frame moving with Sylda with respect to the orbital frame. As described in Sec. 3.3, after its release, Sylda has a nonzero angular velocity around its center of mass, that is lower or equal to 0.006 rad/s. The deployment is simulated as taking place after a de-tumbling procedure (discussed in Sec.3.2) that significantly attenuates the angular velocity of Sylda on the three axes of the body frame, achieving a quasi-stabilization on the three axes. Additionally, the deployment is designed to take place on the orbital plane, and therefore the out-of plane motion is assumed negligible and not considered here. In the codes the initial angular velocity of Sylda on the orbital plane, after detumbling, is taken as $\dot{\alpha}_0 = 0.0006\,\text{rad/s}$, i.e. 1/10 of the pre-detumbling angular

velocity about the axis orthogonal to the orbital plane. By starting the deployment at apogee, right after Sylda's release, the attitude of Sylda can be assumed as in the picture below. At the start of deployment at apogee, right after Sylda's release from the dual-payload, *Sylda*'s projection on the orbital plane is expected to be as shown in Fig.3.11.

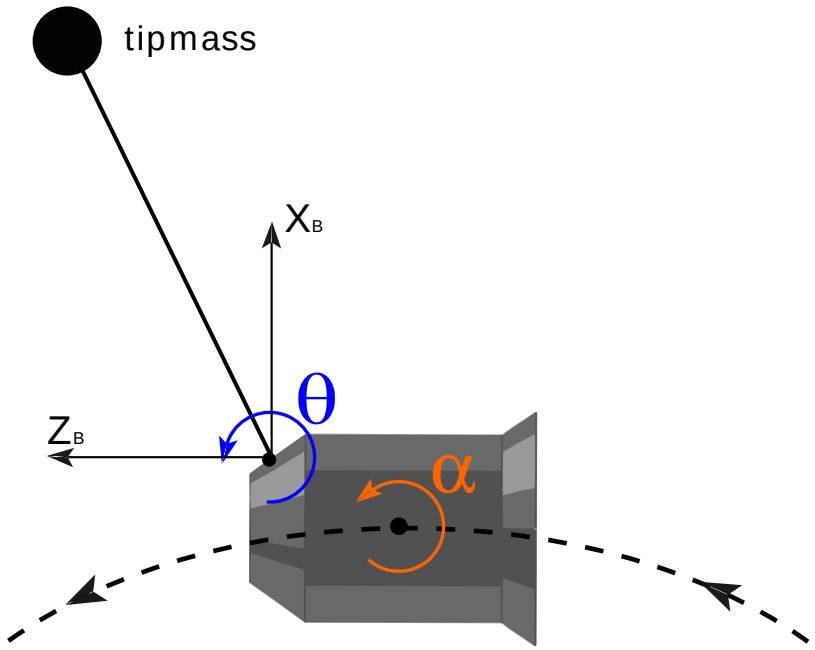

Figure 3.11: *Sylda with one tether and respective rotation angles.*

The moment of inertia of Sylda about the $\hat{u}_w$ direction orthogonal to the orbital plane, and passing through its center of mass, is calculated using *Solidworks* implementing the features provided in Sec.1.3.1. The resulting moment of inertia is $J_{S,w} = 3459.44\,\text{kg m}^2$.

The profile of θ is obtained by doubly integrating the equation with an ODE45:

$$\ddot{\psi} + \dot{\psi}\frac{\dot{J}_t}{J_t} + \frac{3}{2}\frac{\mu}{r_G^3} sin(2(\psi - \nu)) = 0 \tag{3.16}$$

where $\psi = \theta + \nu$, being ν the true anomaly; the dot represents a derivative with respect to time; r_G is the radial location of the system's center of mass; $J_t = m_{tip} l^2 + \frac{1}{3}\tilde{\rho}_t l^3$ is the moment of inertia of each tether and respective tip-mass m_{tip} with respect to an axis orthogonal to the orbital plane and passing through the system's center of mass G (the distance between G and tether attachment point can be neglected in the dynamics of the tether librations, being much lower than tether length scales); $\tilde{\rho}_t$ is the linear density of tether material (i.e. mass per unit length of tether, that is homogeneous along its length); $l(t)$ is the deployed tether length that is changing over time, according to a law of tether release velocity $\dot{l}$; $\dot{J}_t = l\dot{l}(2m_{tip} + \tilde{\rho}_t\, l)$ is the variation of moment of inertia over time.

The tether tension at the attachment point is computed as $T = u\ \omega^2 P_c$ (based on what reported in Ref. [8]), where $\omega = \dot{\nu}$ is the orbital rate, and

$$u = (\dot{\theta} + 1)^2 + \frac{1}{1 + e\cos\nu}(3\cos^2\theta - 1) \tag{3.17}$$

$$P_c = l\frac{(m_{tip} + \frac{1}{2}m_t)(m_s + \frac{1}{2}m_t)}{m_{tot}}\left(1 - \frac{m_t}{2m_{tot}}\right) \tag{3.18}$$

The term P_c varies over time, due to change of released tether mass m_t, and of the deployed tether length l. m_{tot} is the total mass of the system.

The angle α of Sylda (and co-moving body frame) with respect to the radial direction along the orbit, is then computed by doubly-integrating with an ODE45 the following differential equation:

$$\ddot{\delta} + \frac{3}{2}\frac{\mu}{r^3}\sin 2(\delta - \nu) = 10^{-3}\dot{\nu}^2 + \frac{\tilde{M}_w}{J_{S,w}} \tag{3.19}$$

where $\delta = \alpha + \nu$; $J_{S,w}$ is the moment of inertia of Sylda about the axis $\hat{u}_w$ orthogonal to the orbital plane, and passing through its center of mass; $\tilde{M}_w = \tilde{M}_{w,1} + \tilde{M}_{w,2}$ is the total moment about $\hat{u}_w$, neglecting all perturbation forces other than tension exerted by the two tethers. The main component of gravitational torque is also accounted for, but separated from the term $\tilde{M}_w$, and approximated as $10^{-3}\dot{\nu}^2$, as from Ref.[8].

The tethers exert two separate moments at the respective attachment points to Sylda, related to the value of tension at those points and the respective moment arms.

$$\tilde{M}_{w,1} = \overline{GA} \cdot T\left[\cos(\alpha + \epsilon)\sin\theta - \sin(\alpha + \epsilon)\cos\theta\right] \tag{3.20}$$

$$\tilde{M}_{w,2} = \overline{GB} \cdot T\left[\cos(\alpha + \lambda)\sin(\theta + \pi) - \sin(\alpha + \lambda)\cos(\theta + \pi)\right] \tag{3.21}$$

where $\overline{GA}$ and $\overline{GB}$ the moment arms, i.e. the distance from the attachment point of the tethers with respect to Sylda's center of mass, constant over time; ϵ and λ are the angles between the moment arms and the first body-frame unit vector $\hat{u_{b1}} = \hat{u}_\xi$ co-rotating with Sylda, defined as

$$\epsilon = \tan^{-1}(H_s/D_s) \tag{3.22}$$

$$\lambda = \pi - \epsilon \tag{3.23}$$

being H_s the height of Sylda modeled as a hollow cylinder, and D_s its external diameter. These angles are shown in Fig. 3.12.

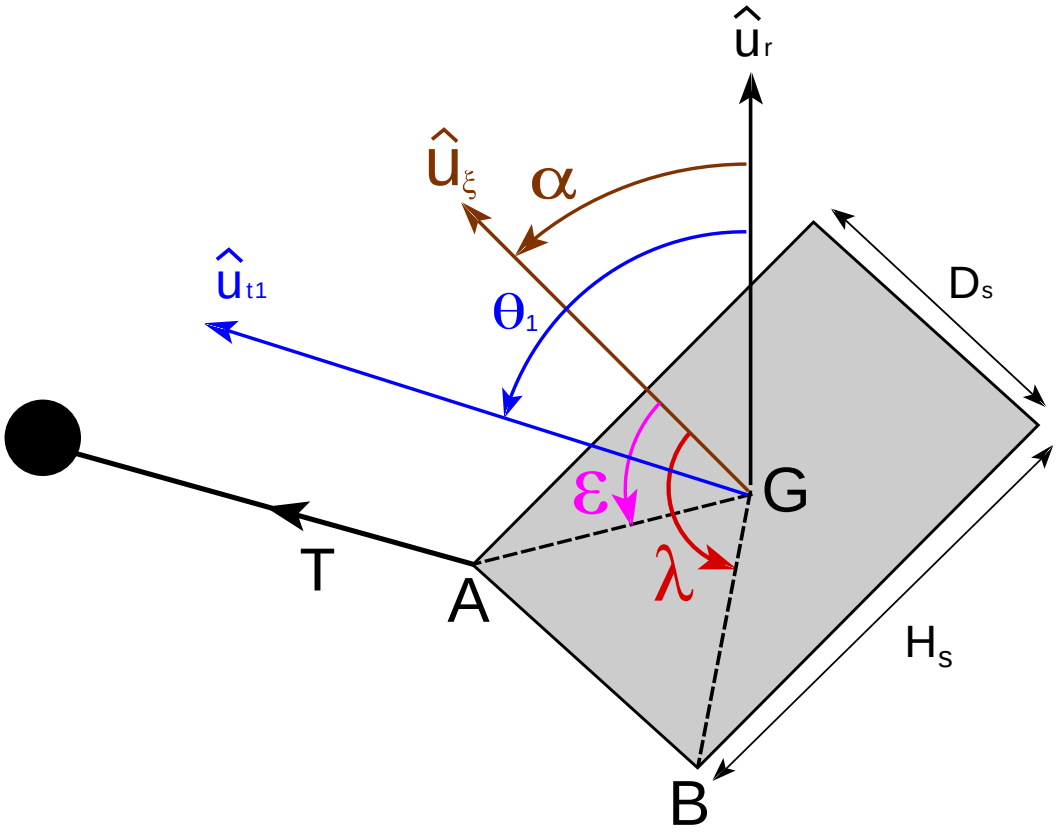

Figure 3.12: *Sylda, here simplified to a cilinder, with one tether segment. The unit vector $\hat{u}_{t1}$ is parallel to the tether. This picture shows the constant angles ϵ and δ, that are related to the geometry of Sylda. These angles are measured with respect to the first axis X_B of the body frame (unit vector $\boldsymbol{u}_\xi$). Other angles displayed are: the angle of Sylda's body with respect to the radial direction (α); the angle θ of the tether, rotating about the attachment point on Sylda, with respect to the radial direction $\hat{u}_r$. The positive tension $\boldsymbol{T}$ acting along the tether, and keeping it taut, is shown too.*

Numerical computations lead to the profiles of in-plane angles of the tether and of Sylda's body. A useful information is the profile of motion of the tip-mass, at the end of the tether, during deployment and with respect to the body frame. The body frame is corotating with Sylda, with the same angle α with respect to the orbital frame (after detumbling of Sylda, i.e. when only in-plane motion takes place). Therefore the relative motion of the tether with respect to the body frame can be obtained from the difference between α and θ that are both angle on the orbital plane, and measured with respect to the radial vector. The spatial coordinates with respect to the body frame are then computed as:

$$X_B = L_t \ \cos(\theta - \alpha) \tag{3.24}$$

$$Z_B = L_t \ \sin(\theta - \alpha) \tag{3.25}$$

where the horizontal displacement from Sylda is X_B and the vertical displacement is

Z_B. X_B is the axis directed along the first unit vector of the body frame $\hat{u}_\xi$ and Z_B along the third unit vector of the body frame $\hat{u}_\zeta$. The tether length $L_t(t)$ is variable over time since the tether is being deployed. The tip-mass profile during the entire deployment is then plot and posted below.

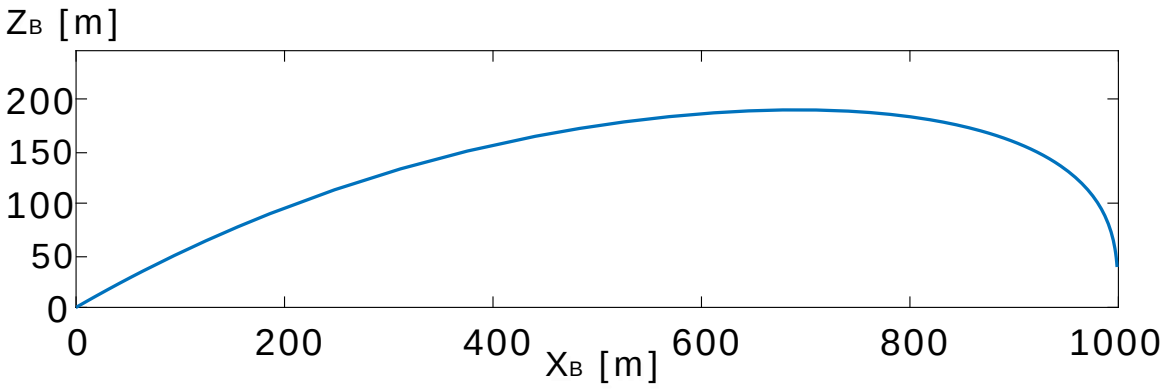

Figure 3.13: *Spatial deviation Z_B, throughout deployment, of the tip-mass with respect to the optical axis of the vision system, i.e. the X_B axis of the body frame.*

This profile is subsequently employed for the vision system analysis presented in Chapter 4.

3.4.4 Analysis with two tethers deployed differently

A subsequent analysis is performed with the two tethers of different lengths, different release velocities and profiles, in order to evaluate the tip-mass profiles.

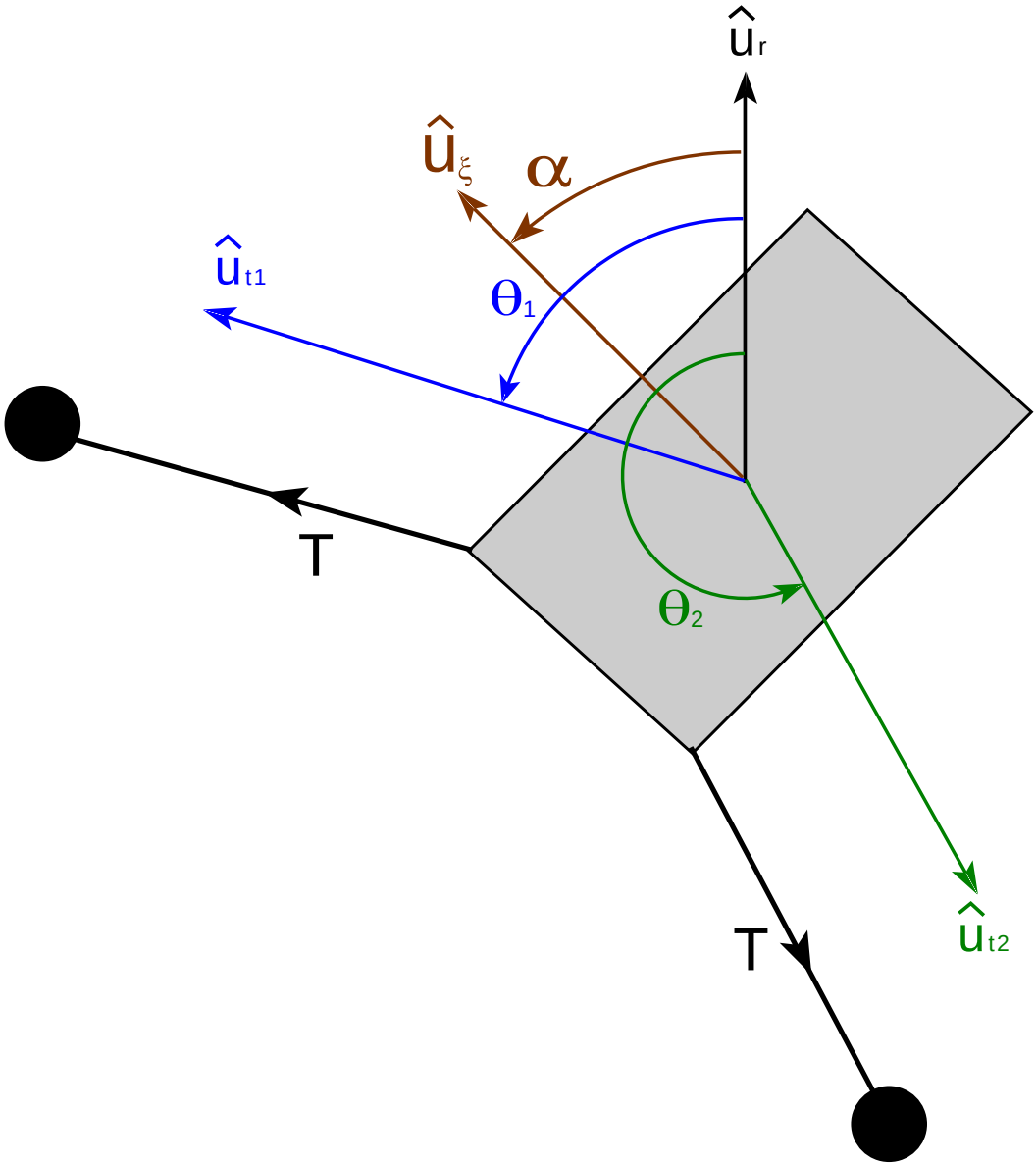

Figure 3.14: *Sylda, here simplified to a cilinder, with two tether segments (butterfly configuration). The unit vectors $\hat{u}_{t1}$ and $\hat{u}_{t2}$ are parallel respectively to the first and second tether segments. This picture shows: the angle of Sylda's body with respect to the radial direction (α); the angles of the first and second tether segment (θ_1 and θ_2 respectively), rotating around their respective attachment points on Sylda, with respect to the radial direction $\hat{u}_r$. The positive tension $\boldsymbol{T}$ acting along the two tether segments, keeping them taut, is shown too.*

For the first tether and related tip mass, the equation describing its local rotational motion on the orbital plane is:

$$\ddot{\psi}_1 + \dot{\psi}_1 \frac{\dot{J}_1}{J_1} + \frac{3}{2}\frac{\mu}{r^3} sin(2(\psi_1 - \nu)) = 0 \tag{3.26}$$

and for the second tether and related tip mass m_2:

$$\ddot{\psi}_2 + \dot{\psi}_2 \frac{\dot{J}_2}{J_2} + \frac{3}{2}\frac{\mu}{r^3} sin(2(\psi_2 - \nu)) = 0 \tag{3.27}$$

where ν is the true anomaly; $\psi_1 = \theta_1 + \nu$ and $\psi_2 = \theta_2 + \nu$; the dot represents a derivative with respect to time; r is the radial location of the system's center of mass (assumed coincident with Sylda, as point mass m_S); $J_1 = m_{tip} l_1^2 + \frac{1}{3}\tilde{\rho}_t l_1^3$ and $J_2 = m_{tip} l_2^2 + \frac{1}{3}\tilde{\rho}_t l_2^3$ are the moments of inertia of the first and second tethers and respective tip-mass with respect to an axis orthogonal to the orbital plane (i.e. the plane of deployment) and passing through the point mass of Sylda. $\tilde{\rho}_t$ is the linear density of tether material (tether is homogeneous along its length); $l_1(t)$ and $l_2(t)$ is the deployed tether length that is changing over time, according to a law of tether release velocity set by design ($\dot{l_1}$ and $\dot{l_2}$). With all this it is possible to compute the variation of moment of inertia over time:

$$\dot{J}_1 = l_1 \dot{l_1} (2 m_{tip} + \tilde{\rho}_t \; l_1) \tag{3.28}$$

$$\dot{J}_2 = l_2 \dot{l_2} (2 m_{tip} + \tilde{\rho}_t \; l_2) \tag{3.29}$$

With all this it is possible to integrate Eqns. 3.26, 3.16 over time and obtain a profile of θ_1 and θ_2 over time by subtracting the orbital rate $\dot{\nu}$ to the computed profiles of ψ_1 and ψ_2.

3.5 Simulation of BET deployment from Sylda nearby its perigee

In this section, a deployment occurring when Sylda is nearby its perigee is simulated. As in the previous section, deployment can be reasonably assumed to take place only on the orbital plane. However, in this case, there are two main external perturbation forces that are present, that were instead absent when deploying nearby the apogee: the aerodynamic drag and electrodynamic drag due to the Lorentz force created by the portion of electrodynamic tether already deployed.
Moreover, in this analysis, the two tethers are assumed to have different lengths and deployment profiles: this means that the code implements separate degrees of freedom for the two tethers. Each tether can oscillate on the orbital plane independently from the other. In the previous section, it was instead assumed to have identical tethers, deployed with the same profile, just on opposite directions. That assumption allowed to consider only one tether in the simulation. In the present case, two tethers are simulated but they are considered as part of a single electrodynamic tether. This means that there is a single tether divided in two electrically connected segments, deployed on opposite directions. At the end of one segment there is a hollow cathode, part of the cathodic tip-mass, and at the other end there is an anodic mass. The current increases going from the anodic tip towards the cathode, with a maximum at the zero-bias point

B, and a light decrease from B to the cathode C. The butterfly configuration, and the lengths of each segment of tether, are tailored in order to maintain the electrodynamic center of pressure as close as possible to the system's center of mass, as already discussed in Sec. 2.2.
The tape-tether employed in this analysis has the same geometric features as previous analyses, i.e. width of $w_t = 3\,\text{cm}$, thickness of $h_t = 100\,\mu\text{m}$ and total length when fully deployed of $L_t = 2\,\text{km}$. This total length is subdivided in a segment from Sylda to the anodic tip-mass of length $L_{t1} = 1200\,\text{m}$, and another from Sylda to the cathodic tip-mass of length $L_{t2} = 800\,\text{m}$.
During the deployment of the two tether segments, the center of mass of the system can vary due to different tether release velocities. The distance of the system's center of mass from the cathodic tip C is computed as:

$$x_{CG} = \frac{(m_S + m_t - m_{t,dep})L_{t2} + m_A(L_{t1} + L_{t2}) + m_{t,dep}\frac{L_{t1}+L_{t2}}{2}}{m_{tot}} \tag{3.30}$$

the value of center of mass changes during deployment, with the variation of L_{t1}, L_{t2} and $m_{t,dep} = \tilde{\rho}_t(L_{t1} + L_{t2})$ that is the mass of tether already deployed. The moment of inertia of Sylda about its center of mass, and with respect to the axis orthogonal to the orbital plane, it is computed with a Solidworks model, resulting as $J_{S,w} = 3459\,\text{kgm}^2$. $m_{tot} = m_A + m_S + m_C + m_t$ is the total mass of the system.

In this case, since the in-plane local rotation only is considered the numerical model is based on these dimensional equations, that are a simplification of what seen in Section 2.2.1. The orbital inclination is considered fixed and equal to zero: this allows to introduce the variable $\psi = \nu + \theta$, that simplifies computations. After computing the profiles of ψ and ν over time, the profile of the in-plane angle θ can be derived. Out-of-plane motion is neglected: consequently, the right-ascension of the ascending node is fixed, and the argument of perigee varies only due to in-plane perturbations. Moreover, the out-of-plane angle seen in Sec.2.2 is zero ($\varphi = 0$), and therefore the equation 2.47 can be simplified to the form seen below in equation 3.35 ($tan\varphi = 0$ and $\dot{\varphi} = 0$).

$$\frac{da}{dt} = \dot{a} = \frac{2a^{3/2}}{\sqrt{\mu(1-e^2)}}\left[e\ \sin\nu f_r + (1 + e\ \cos\nu)f_s\right] \tag{3.31}$$

$$\frac{de}{dt} = \dot{e} = \sqrt{\frac{a(1-e^2)}{\mu}}\left[\sin\nu f_r + \frac{2\cos\nu + e(1+\cos^2\nu)}{1 + e\ \cos\nu}f_s\right] \tag{3.32}$$

$$\frac{d\nu}{dt} = \dot{\nu} = \frac{\sqrt{\mu a(1-e^2)}}{r_G^2} - \sqrt{\frac{a(1-e^2)}{\mu}}\left[-\frac{\cos\nu}{e}f_r + \frac{\sin\nu}{e}\left(1 + \frac{1}{1+e\cos\nu}\right)f_s\right] \tag{3.33}$$

$$\frac{d\omega}{dt} = \dot{\omega} = \sqrt{\frac{a(1-e^2)}{\mu}}\left[-\frac{\cos\nu}{e}f_r + \frac{\sin\nu}{e}\left(1 + \frac{1}{1+e\cos\nu}\right)f_s\right] \tag{3.34}$$

$$\ddot{\psi} = -\dot{\psi}\frac{\dot{J}_t}{J_t} - \frac{3\mu}{2\ r_G^3}\sin 2(\psi - \nu) + 10^{-3}\ \dot{\nu}^2 + \frac{M_{t,w}}{J_t} \tag{3.35}$$

where all the variables are defined as in Sec.2.2.1. $J_t = m_{tip}l^2 + \frac{1}{3}\tilde{\rho}_t l^3$ and $\dot{J}_t = l\dot{l}(2m_{tip} + \tilde{\rho}_t\ l)$ are identical to what already defined in Sec.3.4.3, i.e. the moment of inertia of each tether and respective tip-mass m_{tip}, and its variation over time, with respect to an axis orthogonal to the orbital plane and passing through the system's center of mass G; $\tilde{\rho}_t$ is the linear density of tether material (i.e. mass per unit length, with tether homogeneous along its length); $l(t)$ is the deployed tether length changing over time, according to a prescribed law of tether release velocity $\dot{l}$.

The aerodynamic drag is computed assuming a constant drag coefficient $c_d = 2.2$ and by taking a drag area for all the components of the system averaged along a full rotation of the system. This average drag area is computed as:

$$S_{avg} = \frac{2S_{max}}{\pi} \tag{3.36}$$

where S_{max} is the maximum drag area of each component.
The same data described in Sec. 2.1 is used for the air density, plasma electron density and for the computation of electrodynamic quantities (average tether current, electrodynamic center of pressure). The initial semi-major axis and eccentricity are computed assuming a GTO orbit with altitude of perigee of 300 km. The initial true anomaly is very low, such that the deployment simulation starts very close to the perigee. All the other orbital parameters are initially set to zero (inclination and right-ascension of the ascending node do not vary during the simulation).
The same initial values used in Sec.3.4 are used for the initial Sylda in-plane angular velocity, and the tethers are assumed to be released with an initial angle of $\theta_1 = 30°$ and $\theta_2 = \theta_1 + \pi$, and with zero initial angular velocity around the attachment points to Sylda.
Two different profiles of tether release velocity are used for the two tether segments: they are both released with a constant velocity in the first part of deployment, and then the velocity decreases following the profile described in Sec.3.4.2. However, the initial constant release velocity is different for the two tethers. As already stated, the two tether segments rotate independently each from the other.
The entire tether length $L_{t1} + L_{t2}$ is considered for the computation of the average current and consequent Lorentz drag force acting on the system's center of mass, with the nondimensional method already described in Sec. 2.1. A total torque is computed using the total Lorentz force and the moment arm between the system's center of mass G and the electrodynamic center of pressure CP. This total torque is then distributed between the two tether segments depending on their respective lengths. The torques acting on each tether generate independent in-plane rotations of the two tethers.

The tether with its respective tip-mass, in this analysis, are rotating on the orbital plane with respect to Sylda as a rigid body, and are subjected to external pertubations that create the torque $M_{t,w}$.
Instead, Sylda is subjected to a torque created by the tether pulling at the attachment point. This torque is much greater than the torque created on Sylda by the aerodynamic drag (since the moment arm is extremely low, differently from what happens with the tether). Moreover, the electrodynamic force acts on the tether and is

transmitted from this one to Sylda. In conclusion, it is reasonable to approximate the total torque exterted upon Sylda as the torque created by the two BET tethers at the attachment points. Hence, Eq. 3.19 can be used again also here to simulate the rotation of Sylda, defined by the angle α. Also in this analysis, as done in Sec.3.4, the initial angular velocity of Sylda on the orbital plane, after detumbling, is taken as $\dot{\alpha}_0 = 0.0006\,\mathrm{rad/s}$.

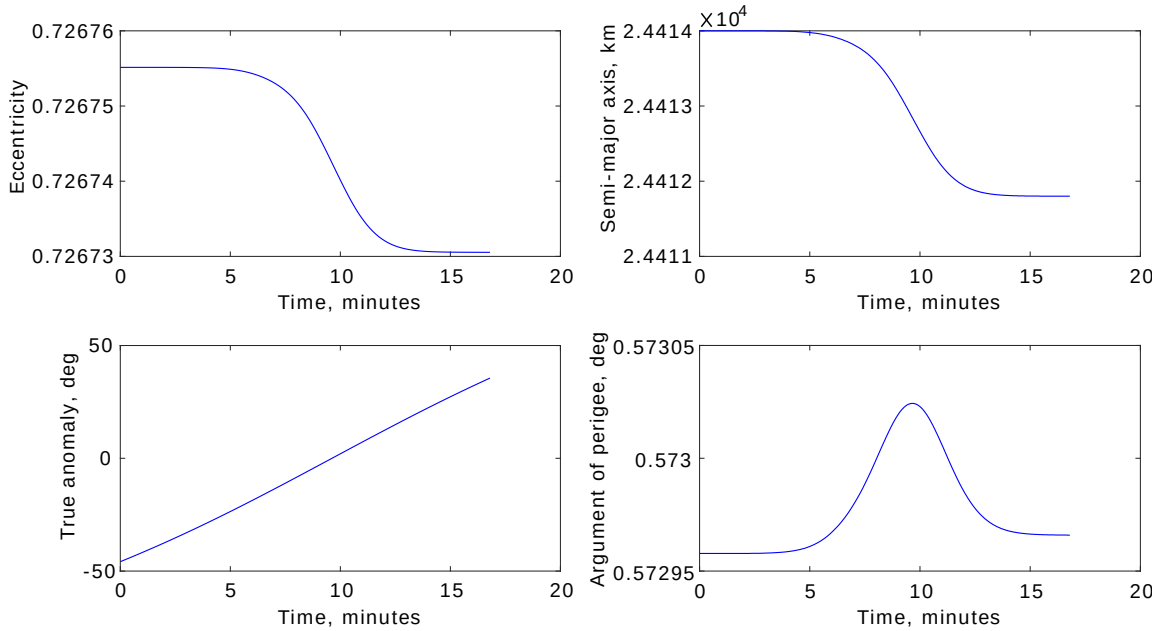

Figure 3.15: *Profiles of Keplerian orbital parameters during deployment nearby the perigee. As shown in the plots, the presence of perturbation forces below the altitude of* 2000 km *creates a variation in the orbital parameters.*

The first segment of tether of length 1200 m is deployed with an initial release velocity of 1.6 m/s, and the second of length 800 m with an initial release velocity of 1.3 m/s. The initial in-plane angle of the tethers with respect to the radial vector are $\theta_1 = \pi/4 = 45°$ and $\theta_2 = \theta_1 + \pi$. Then, as done in previous Section, the release velocity decreases at a certain prescribed point, and goes to zero with a zero-tangent both at the beginning and at the end of the decreasing part of the profile. The code recognizes when one of the two tethers is completely deployed (in this case the second tether segment is fully deployed when the first segment is still under deployment) and zeroes the release velocity as deployment is over. The entire deployment process lasts about 17 minutes. All of this is shown in Fig. 3.16.

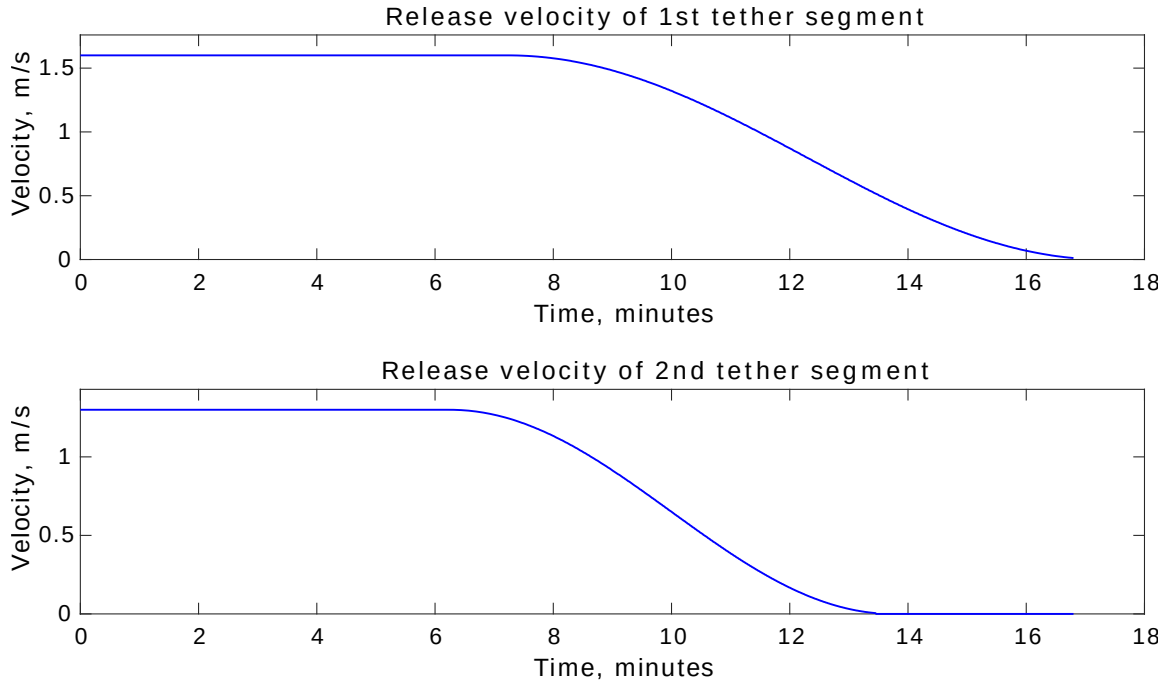

Figure 3.16: *Release velocity profiles for first and second segments of tether.*

The tip-mass coordinates with respect to the body frame, resulting from the simulation, are reported in Figs. 3.17 and 3.18. These plots show that deploying nearby the perigee of the initial GTO would lead to an excessive oscillation of the tethers with respect to the body frame causing possible interference between the tether under deployment and Sylda's body. Therefore, it is preferable to have instead a deployment of the two tether segments during the time spent above 2000 km, in order to avoid perturbations that cause these intense oscillations. The following section reports the simulation of deployment in a zone between apogee and perigee, as the satellite is leaving the perigee towards the apogee.

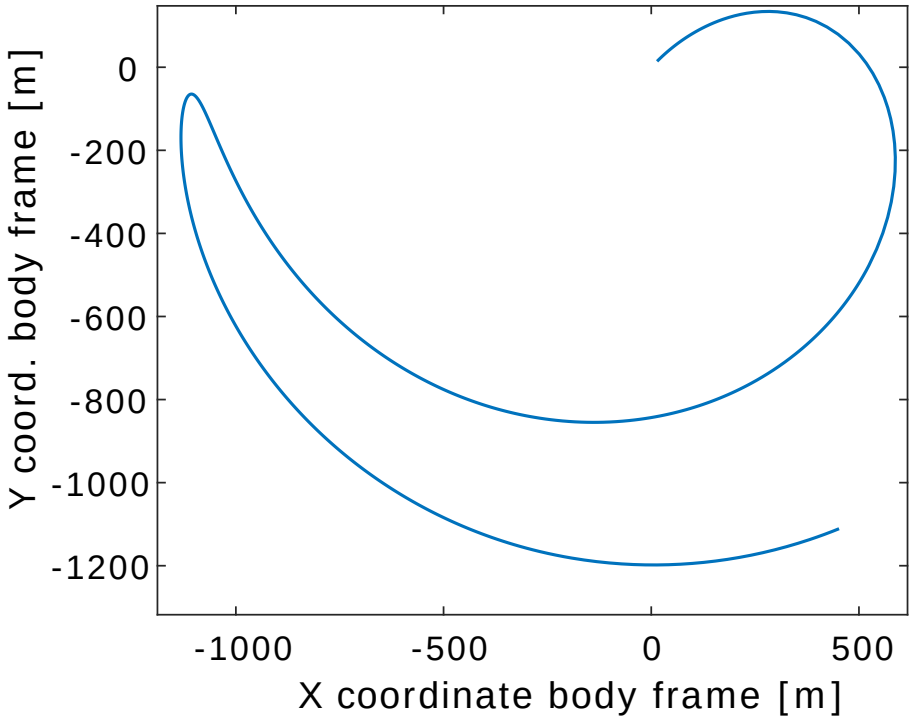

Figure 3.17: *Profile of anodic tip-mass during deployment, in the body frame of reference.*

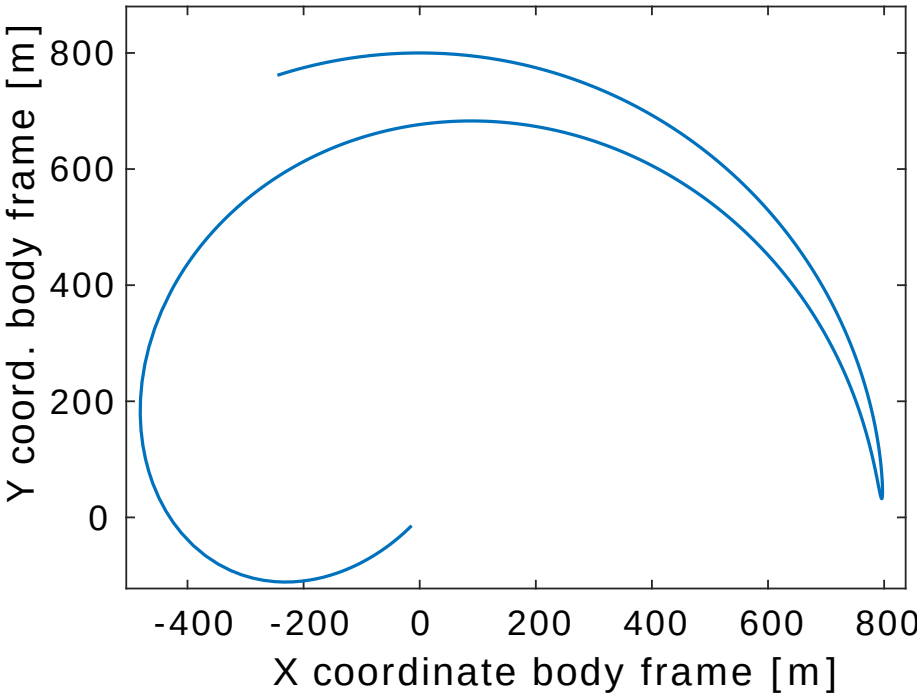

Figure 3.18: *Profile of cathodic tip-mass during deployment, in the body frame of reference.*

3.6 Deployment of two tether segments at mid-way of the orbit

A third option for deployment is when the spacecraft, after detumbling during the first passage across the perigee region, it goes back towards the apogee. The deployment should start right after the system surpasses an altitude of about 2000 km, after leaving the perigee: this means that drag perturbations become negligible, and the system was just detumbled. These are ideal conditions to start the deployment. in the first instants of deployment, there is a yo-yo stabilization, that zeroes the angular velocity along the third body-frame axis, and then the deployment goes on with minimum risk of interference between the tethers and Sylda.

The deployment takes about 14 minutes to complete and diagrams of deployment profile for this case are posted below. Optimal values for deployment are release velocities of 1.9 m/s in the constant part for the first tether segment and 1.7 m/s in the constant part for the second tether segment, as shown in Fig.3.20. The initial in-plane angle of the tethers with respect to the radial vector are $\theta_1 = \pi/4 = 45°$ and $\theta_2 = \theta_1 + \pi$. The true anomaly of the initial Sylda's orbit corresponding to an altitude of 2000 km is about 58.8°: therefore, it is chosen as initial true anomaly the value of 60°, making sure that it starts when the system surpassed that altitude threshold. After the tethers are deployed the system gradually stabilizes itself with all its components rotating together as a dumbbell system. Parameters of the system and of deployment are designed to provide the system, by the time it reaches again the perigee zone, a sufficient in-plane angular velocity in order to prevent tether slackness and consequent instability, and not too high to prevent tether breaking during deorbit.

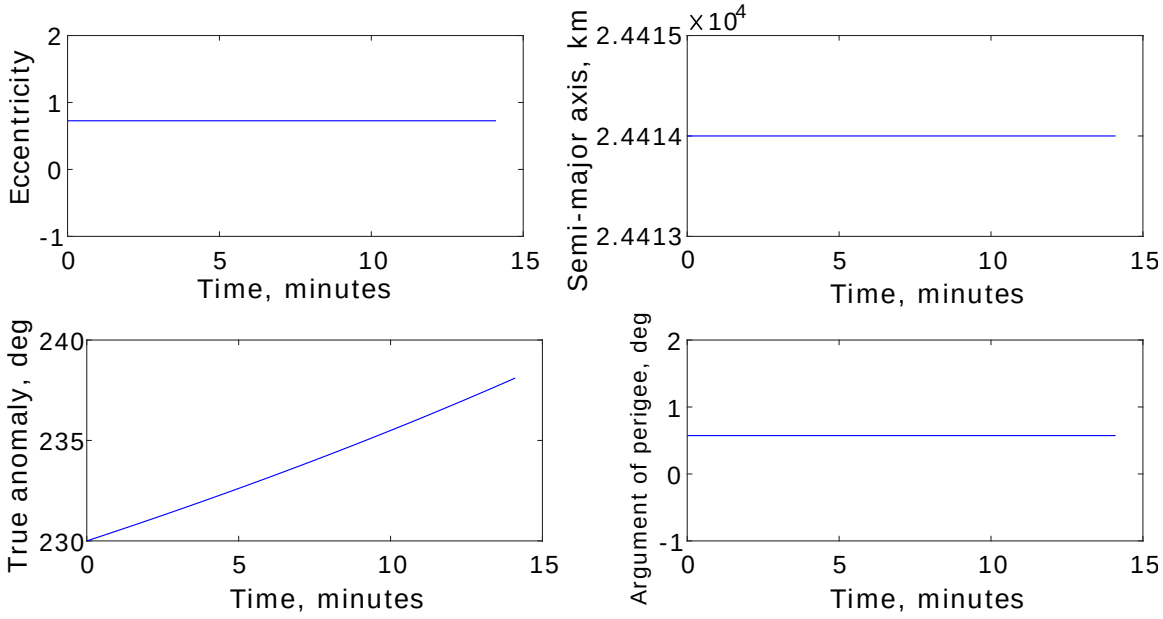

Figure 3.19: *Profiles of Keplerian orbital parameters during deployment at mid-way. As shown in the plots, perturbation forces are absent at these altitudes, so orbital parameters of semi-major axis, eccentricity, and argument of perigee do not vary during deployment time.*

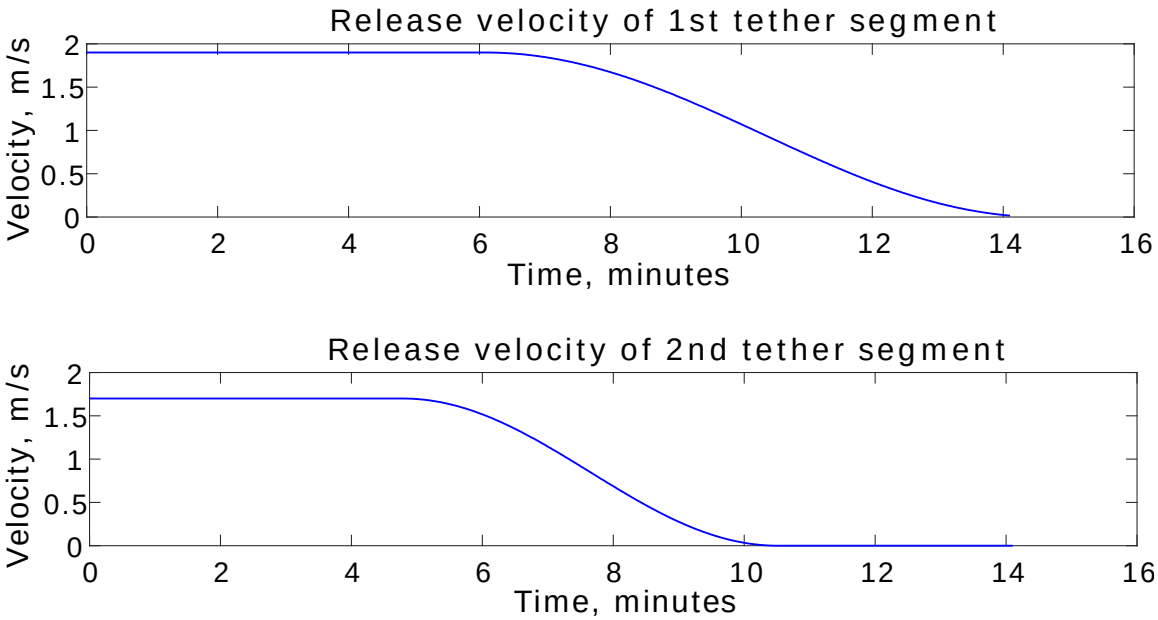

Figure 3.20: *Release velocity profiles for first and second segments of tether with deployment at mid-way.*

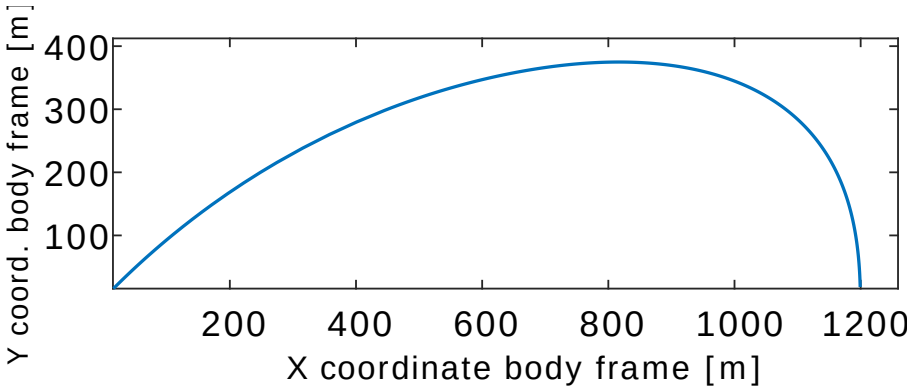

Figure 3.21: *Profile of anodic tip-mass during deployment in the body frame, for deployment at mid-way.*

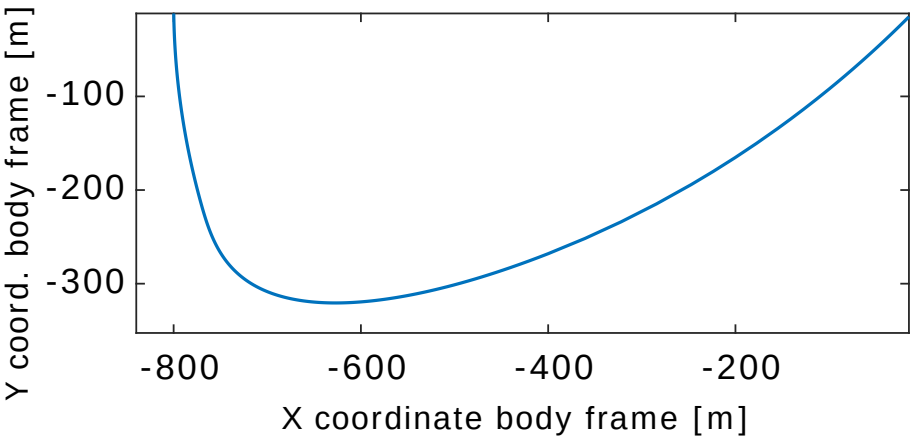

Figure 3.22: *Profile of cathodic tip-mass during deployment in the body frame, for deployment at mid-way.*

Chapter 4

Analysis of Vision System for Tethers Attitude Detection

As previously stated, an unconstrained tethered system in GTO, such as the *butterfly* system mounted on Sylda, undergoes full rotations around its center of mass, primarily on the orbital plane. However, this local rotation is null at the start of tether deployment after detumbling Sylda, and it increases with the increasing deployed length of the two tether segments. Therefore, the stabilizing effect due to centrifugal force becomes significant only after the tether is at least partially deployed. Consequently, the deployment is the most critical phase in terms of system's stability.

This is the reason why a branch of this PhD research, presented in this Chapter, focuses on the analysis of a vision system, used for tether's attitude detection, to be mounted on the upper part of *Sylda*. The vision system has the specific aim of tracking the tip-masses during deployment in order to provide the information on the attitude of the two tether segments. The tether segments are treated again as dumbbells, that is reasonable since they are kept taut and straight by means of a positive tension, created by controlling the tether release velocity. In fact, the output from the vision system is employed by feedback control system to force the tip-mass to follow a nominal deployment profile. This profile is properly designed in order to avoid both instabilities (tether slackness) and interference between the tethers and Sylda during deployment.

The design of the vision system relies upon the evaluation of the uncertainty affecting visual measurements on the position of the tip-mass, in a certain range of interest. A representative tether's deployment velocity profile is given as input to simulate the measurement performance of different configurations of vision system. This profile is similar to the profiles presented in Chapter 3, and it is shown in Fig. 4.1.

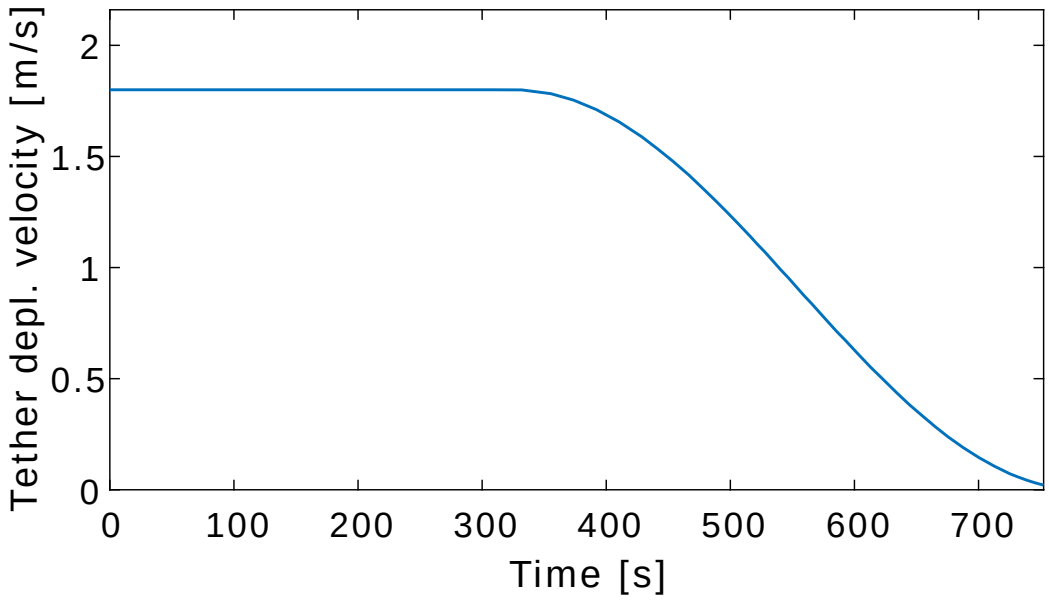

Figure 4.1: *Profile of tether deployment velocity*

For the vision system analysis presented in this Chapter, only one segment of tether is considered, with length of 1 km. The optical axis of the camera is considered coincident with the body-frame axis X_B used in previous Chapters, as described in Appendix B. Throughout this Chapter, the distance of the tip-mass from Sylda, along the optical axis X_B, is called X, and the deviation from this axis, on the orbital plane, is called Z (that is in the direction of the body-frame axis Z_B used in previous Chapters, and defined in Appendix B). The angle between X_B and the line of sight of the tip-mass, during deployment, is called $\beta = \theta - \alpha$, where θ is the angle of the tether with respect to the unit vector $\hat{u}_r$ of the orbital radius, and α is the angle of Sylda's body with respect to $\hat{u}_r$. These angles comply with the notation used in the previous Chapters. All of this is depicted in Fig. 4.2.

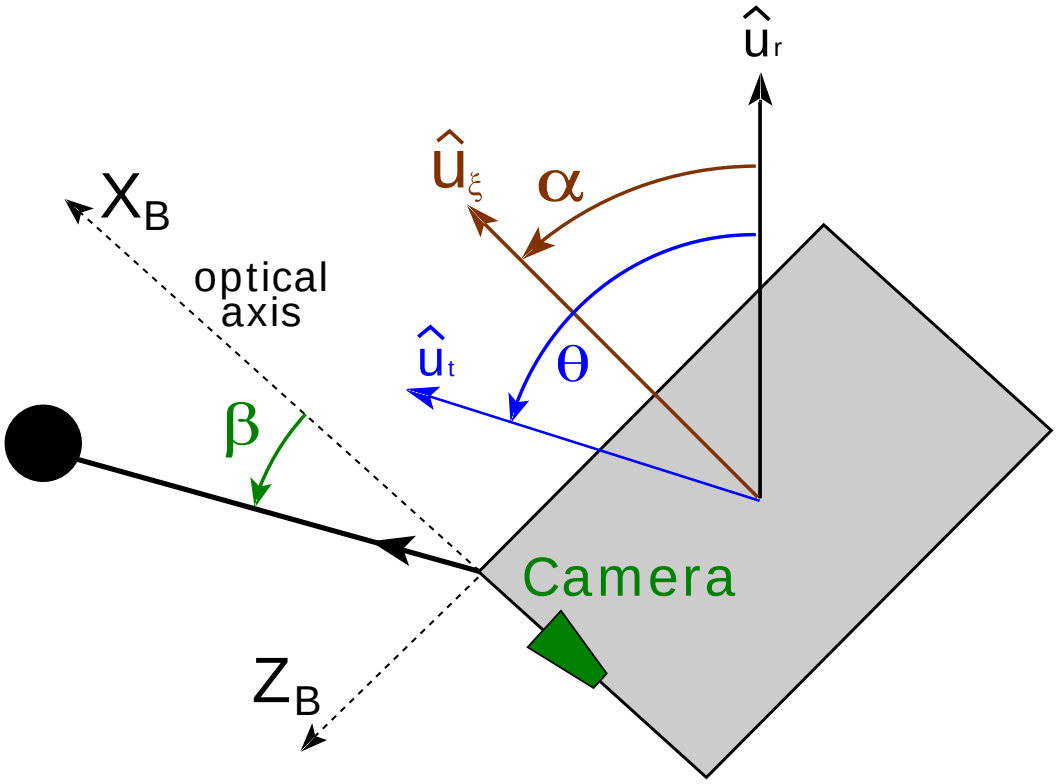

Figure 4.2: *Sylda, projected here as a cylinder on the orbital plane, at the start of deployment. Only one tether segment is considered and the camera to track its tip-mass. The body frame axes are represented, and the angle β of the tip-mass line of sight with respect to the optical axis of the camera.*

From the tether deployment velocity profile the position of the tip-mass is computed, throughout deployment and with respect to the *body-frame*. The tip-mass profile is shown in Fig. 4.3.

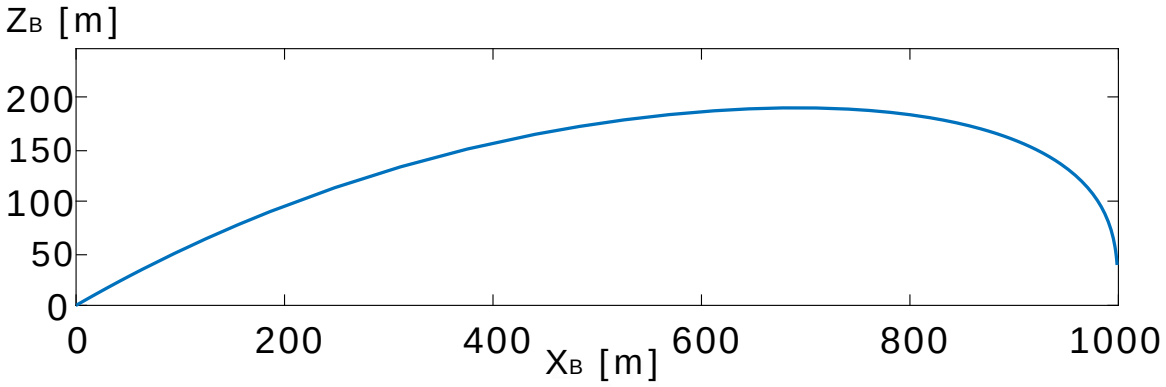

Figure 4.3: *Spatial deviation Z, throughout deployment, of the tip-mass with respect to its distance from Sylda X, along the optical axis of the vision system.*

The vision system is designed with a field of view such that the tip-mass always lies

inside it during the tether deployment. In the last part of deployment, the system tends towards a stable configuration with Sylda and the two tether segments approximately rotating together as a single rigid body, i.e. with the same angular velocity with respect to the orbital frame. The vision system is then optimized to provide the information on tether attitude, by detecting the location of the tip-mass, for the deployment phase until the system reaches a stable configuration. The vision system analysis ultimately provides a framework for selecting the optimal focal length, and number of cameras, to efficiently track the two tip-masses during deployment, using the *butterfly* configuration with two tether segments (refer to Sec. 2.2 for description of this configuration).

4.1 Description of the measurement system

The measurement system for tracking the tip-mass during deployment is made of one or two cameras, for each tip-mass. Using the butterfly configuration with two tether segments and respective tip-masses, this leads to two or four cameras in total, to be mounted on the upper part of Sylda near the storage boxes for the tether segments, described in Sec.3.1.
The optimal selection of the vision system is performed taking into account two possible measurement scenarios:

- A first scenario in which only the angular position, or direction, of the tip-mass is measured, i.e. the angle on the orbital plane from the optical axis of the camera to the line of sight of the tip-mass. Only one angle is necessary, since the deployment takes place on the orbital plane, and the out-of-plane motion is negligible. In this measurement scenario, no information about the distance between Sylda and the tip-mass is provided directly by the vision system. This measure can be obtained indirectly by combining the information of angular position with the released length of the tether, that is controlled by an electrical motor programmed with a prescribed tether release velocity profile.
- A second scenario in which both the angular position (i.e. direction) and the distance of the tip-mass from Sylda are directly evaluated by the vision system.

4.1.1 First measurement scenario: only direction

In order to detect only the angular position, or direction, of the tip-mass, the measurement system can be made of only one camera. The selection of the camera is performed by selecting the intrinsic parameters, defined by the sensor resolution, sensor or pixel size, and field of view or focal length of the lens. During deployment of the tether the distance of the observed tip-mass can vary from few meters to the order of 1-1.5 km and, as shown in Fig.4.6, the angle between the line of sight of the tip-mass and the optical axis is maximum at the beginning of deployment, and it monotonically decrease during deployment, with a steeper decrease at the end of it.

The camera selection is performed according to the following procedure:

1. the camera Field-of View (FOV) is defined from the maximum angle β_{max} of the tip-mass line of sight from the optical axis, i.e. when the tip-mass is at the lower limit X_{min} of the desired observable distance range:

$$FOV = 2\beta_{max}\left(X_{min}\right) \tag{4.1}$$

2. in order to minimize the uncertainty on the measure of the tip-mass angular position, the angular resolution $\Delta\beta$ is minimized. Hence, from a technical point of view, the optimal resolution (number of pixels N_p) is the highest one:

$$\Delta\beta \approx \frac{FOV}{N_p} \tag{4.2}$$

   N_p and the sensor size L are selected considering the best available commercial sensors, at reasonable cost. The selected cameras used in this analysis have a resolution of 2588×1940 pixels and a sensor size of $5.70 \times 4.28\,\text{mm}$.

3. After the number of pixels N_p, the sensor size L and the FOV are selected, the other intrinsic parameter can be calculated. For example, the focal length of the lens is computed as:

$$f = \frac{L}{2\tan\left(\frac{FOV}{2}\right)} \tag{4.3}$$

The contribution of the angular resolution $\Delta\beta$ to the standard uncertainty of the angular position of the tip-mass, is evaluated assuming a uniform Probability Density Function (PDF) with total amplitude $\Delta\beta$:

$$\sigma = \frac{\Delta\beta}{2\sqrt{3}} \tag{4.4}$$

This uncertainty contribution can be reduced by employing sub-pixels approaches.
Using one camera, and taking into account only the uncertainty from angular resolution, the limiting factor that drives the camera selection is substantially the maximum angle $\beta_{max}(X_{min})$ of the tip-mass line of sight. A second camera can be employed to measure the angular position of the tip-mass when it is between the distances $X^{'}$, where $(X^{'} > X_{min})$, and X_{max}. $X^{'}$ is an optimization parameter, and represents the tip-mass distance along the optical axis after which a second camera is used. Given that the maximum angular position of the tip-mass $\beta_{max}(X)$ decreases with the distance X, the field of view FOV_2 of the second camera can be reduced. Consequently, also the angular resolution $\Delta\beta_2$ and its contribution to the angular uncertainty σ_2 decrease:

$$\sigma_2 = \frac{\beta_{max}(X^{'})}{\sqrt{3}N_p} < \frac{\beta_{max}(X_{min})}{\sqrt{3}N_p} = \sigma_1 \tag{4.5}$$

In this way, the angular position of the tip-mass is measured by camera 1 (and with standard uncertainty σ_1) from X_{min} to $X^{'}$, and by camera 2 (and with standard uncertainty σ_2) from $X^{'}$ to X_{max}. Fig.4.7 shows the uncertainty versus tip-mass distance X using camera 1 and camera 2, for three different values of $X^{'}$.

Kalman filter with no correlation

In the range $X^{'} < X < X_{max}$, a further reduction in the uncertainty can be achieved by employing a Kalman filter to optimally fuse the measurements from the two cameras. These static system and measurement equations are considered:

$$\begin{cases} x_k = x_{k-1} \\ z_k = x_k + \nu_k \end{cases} \tag{4.6}$$

where x is the angle that locates the line of sight of the tip-mass; z_1 is the angular measure from the first camera, affected by a random noise with variance σ_1^2 ; z_2 is the angular measure from the first camera, affected by a random noise with variance σ_2^2 . The static system model assumes that the two measurements are performed by the two cameras at the same instant of time, such that the position of the tip-mass does not change. Before the two measurements are performed, the angle x_0 is unknown and its uncertainty σ_0 is large ($\sigma_0 \to \infty$). By implementing the Kalman filter described in Ref.[20], after two iterations ($k = 1$ for the measurement of the first camera and $k = 2$ for the measurement of the second one), the following fused angular position x and related variance (or standard uncertainty) are obtained:

$$\begin{cases} x = \frac{\sigma_2^2}{\sigma_1^2+\sigma_2^2} z_1 + \frac{\sigma_1^2}{\sigma_1^2+\sigma_2^2} z_2 \\ \sigma^2 = \frac{\sigma_1^2 \cdot \sigma_2^2}{\sigma_1^2+\sigma_2^2} \end{cases} \tag{4.7}$$

The fundamental assumption in the implementation of this Kalman filter is that the covariance between the random noise υ_1 of camera 1 and υ_2 of camera 2 is zero or near zero.

The computed standard uncertainty σ is lower or equal to σ_2. Fig.4.7 shows with dashed lines, the improvement in uncertainty obtained in the range $X^{'} < X < X_{max}$, when the measurements of the two cameras are fused by the Kalman filter. In Sec.4.2, two cases are analyzed: a first case in which only the measure from camera 2 is used in the range $X^{'} < X < X_{max}$; a second case in which the measures from camera 1 and 2 are both used, and fused together, in the same range $X^{'} < X < X_{max}$.

For the second camera, the resolution N_p and the sensor size L are chosen equal to the first camera. The field of view of the second camera (FOV_2) depends on the angle $\beta(X^{'})$ corresponding to the tip-mass distance ($X^{'}$). Consequently, in order to characterize the second camera the optimal distance $X^{'}$ must be selected. The value of $X^{'}$ is selected by minimizing the standard uncertainty averaged in the range between $X_{2,min}$ and X_{max}, with $X_{2,min} > X_{min}$. X_{min} and $X_{2,min}$ are the minimum tip-mass

distances from Sylda at which respectively camera 1, and camera 2, start to measure. In this analysis, $X_{min} = 0.08\,\text{m}$, and $X_{2,min} = 350\,\text{m}$. In this way, a monodimensional and non-linear optimization is obtained, since both $\beta(X^{'})$ and σ_2 depend on $X^{'}$.

Kalman filter with correlation

The diagram in Fig. 4.8 was created assuming no correlation between the two cameras when implementing the Kalman filter (black line). This diagram has the aim of providing the optimal $X^{'}$, i.e. the value of $X^{'}$ at which there is the minimum average uncertainty. However, the lower is the value of $X^{'}$, the less accurate is the assumption of no correlation. In fact, for the limit case of $X^{'} = 0$, the measures would be completely correlated. This is the reason why a subsequent analysis with correlation is performed.

In this case, instead of Eq.4.6, the following system is used:

$$\begin{cases} x_k = x_{k-1} \\ \boldsymbol{z}_k = \begin{bmatrix} z_{1,k} \\ z_{2,k} \end{bmatrix} = \begin{bmatrix} 1 \\ 1 \end{bmatrix} x_k + \begin{bmatrix} \upsilon_{1,k} \\ \upsilon_{2,k} \end{bmatrix} = \boldsymbol{H}\ x_k + \boldsymbol{\upsilon}_k \end{cases} \tag{4.8}$$

Where x is the angle of the tip-mass line of sight from the optical axis, z_1 is the angular measurement of the first camera affected by random error υ_1 with variance σ_1^2, z_2 is the angular measurement of the second camera affected by random error υ_2 with variance σ_2^2. In the previous analysis, the Kalman filter is applied using a monodimensional measurement equation, while in the present analysis, in order to account for the correlation between the two measurements, the measurement equation is bidimensional. In this case the covariance σ_{12} between the measurements of the two cameras is not zero and, consequently, the covariance matrix of the vector υ_k becomes:

$$R = \begin{bmatrix} \sigma_1^2 & \sigma_{12} \\ \sigma_{12} & \sigma_2^2 \end{bmatrix} \tag{4.9}$$

As in Sec.4.1.1, the model assumes that the two measurement are performed by the two cameras at the same instant of time, such that the position of the tip-mass does not change. By applying the Kalman filter as described in Ref.[20], the prediction step becomes:

$$\hat{x}_k(-) = \hat{x}_{k-1}(+) \tag{4.10}$$

$$P_k(-) = P_{k-1}(+) \tag{4.11}$$

Where $\hat{x}_k(-)$ is the estimated angular value and $P_k(-)$ its variance at step k before the measurements of the two cameras are performed, while $\hat{x}_{k-1}(+)$ and $P_{k-1}(+)$ denote the same quantities at the previous step $k-1$ after the two measurements are

considered.

The Kalman gain $\boldsymbol{K}_k$ and update step are:

$$\boldsymbol{K}_k = P_k(-) \cdot \boldsymbol{H}^T \cdot \left[\boldsymbol{H} \cdot P_k(-) \cdot \boldsymbol{H}^T + \boldsymbol{R}\right]^{-1} \tag{4.12}$$

$$\hat{x}_k(+) = \hat{x}_k(-) + \boldsymbol{K}_k \cdot [\boldsymbol{z}_k - \boldsymbol{H} \cdot \hat{x}_k(-)] \tag{4.13}$$

$$P_k(+) = [1 - \boldsymbol{K}_k \cdot \boldsymbol{H}] \cdot P_k(-) \tag{4.14}$$

Where $\hat{x}_k(+)$ is the estimated angular value and $P_k(+)$ its variance at step k after the two measurement are considered.

In this application of the Kalman filter, since there is only one iteration ($k = 0, 1$) and the system is static (see Eq. 4.8), the expressions in Eq.4.10 become:

$$\hat{x}_1(-) = x_0 \tag{4.15}$$

$$P_1(-) = P_0 = \sigma_0^2 \tag{4.16}$$

Where x_0 is the initial angular value, that is considered unknown before the two measurements are performed, and σ_0^2 is its variance. The Kalman gain becomes:

$$\boldsymbol{K}_1 = \frac{\sigma_0^2}{\sigma_1^2 \cdot \sigma_2^2 - \sigma_{12}^2 + \sigma_0^2 \cdot (\sigma_1^2 + \sigma_2^2 - 2\sigma_{12})} \cdot \begin{bmatrix} \sigma_2^2 - \sigma_{12} \\ \sigma_1^2 - \sigma_{12} \end{bmatrix}^T \tag{4.17}$$

Considering that the variance σ_0^2 is very large (σ_2^2), the Kalman gain can be simplified as:

$$\boldsymbol{K}_1 = \frac{1}{\sigma_1^2 + \sigma_2^2 - 2\sigma_{12}} \cdot \begin{bmatrix} \sigma_2^2 - \sigma_{12} \\ \sigma_1^2 - \sigma_{12} \end{bmatrix}^T \tag{4.18}$$

With the same hypotheses and considering Eq. 4.9, the update step of Eq. 4.12 becomes:

$$\hat{x}_1(+) = x = x_0 + \frac{1}{\sigma_1^2 + \sigma_2^2 - 2\sigma_{12}} \cdot \begin{bmatrix} \sigma_2^2 - \sigma_{12} \\ \sigma_1^2 - \sigma_{12} \end{bmatrix}^T \cdot \begin{bmatrix} z_1 - x_0 \\ z_2 - x_0 \end{bmatrix} = \tag{4.19}$$

$$= \frac{(\sigma_2^2 - \sigma_{12}) \cdot z_1 + (\sigma_1^2 - \sigma_{12}) \cdot z_2}{\sigma_1^2 + \sigma_2^2 - 2\sigma_{12}} = \tag{4.20}$$

$$= \frac{\sigma_2^2 - c_{corr}\sigma_1\sigma_2}{\sigma_1^2 + \sigma_2^2 - 2c_{corr}\sigma_1\sigma_2} z_1 + \frac{\sigma_1^2 - c_{corr}\sigma_1\sigma_2}{\sigma_1^2 + \sigma_2^2 - 2c_{corr}\sigma_1\sigma_2} z_2 \tag{4.21}$$

Where $z_{1,1} = z_1$ and $z_{2,1} = z_2$ are the measurements from the two cameras, x is the evaluated angle after the two measurements are considered, and c_{corr} is the correlation coefficient defined by:

$$c_{corr} = \frac{\sigma_{12}}{\sigma_1 \sigma_2} \tag{4.22}$$

The estimated variance becomes:

$$P_1(+) = \sigma^2 = \frac{\sigma_1^2 \sigma_2^2 - \sigma_{12}^2}{\sigma_1^2 + \sigma_2^2 - 2\sigma_{12} + \frac{\sigma_1^2 \sigma_2^2 - \sigma_{12}^2}{\sigma_0^2}} = \tag{4.23}$$

$$= \frac{\sigma_1^2 \sigma_2^2 - \sigma_{12}^2}{\sigma_1^2 + \sigma_2^2 - 2\sigma_{12}} = \tag{4.24}$$

$$= \frac{\sigma_1^2 \sigma_2^2 (1 - c_{corr}^2)}{\sigma_1^2 + \sigma_2^2 - 2c_{corr}\sigma_1 \sigma_2} \tag{4.25}$$

If the correlation coefficient c_{corr} between the measurements of the two cameras is equal to zero, then the Equations 4.19 and 4.23, can be simplified to the form showed in Sec.4.1.1, which ignores the correlation:

$$\begin{cases} x = \frac{\sigma_2^2}{\sigma_1^2 + \sigma_2^2} z_1 + \frac{\sigma_1^2}{\sigma_1^2 + \sigma_2^2} z_2 \\ \sigma^2 = \frac{\sigma_1^2 \sigma_2^2}{\sigma_1^2 + \sigma_2^2} \end{cases} \tag{4.26}$$

When using the general equations 4.19 and 4.23, the correlation coefficient c_{corr} is needed. The two cameras are assumed perfectly aligned (or any offset is assumed compensated). The coefficient c_{corr} depends on the angular resolutions $\Delta\beta_1$ and $\Delta\beta_2$ of the two cameras, and on the position of the observed tip-mass on the image plane. The deployment profile of the tip-mass is known, as depicted in Fig.4.3. Therefore, for each distance X the corresponding angle β of the tip-mass line of sight from the optical axis is known and can be used in the evaluation of the correlation coefficient c_{corr}. The angular resolution $\Delta\beta_1$ is constant, while $\Delta\beta_2$ of camera 2 depends on $X^{'}$. Thus, for each value of the parameter $X^{'}$ the angular resolutions $\Delta\beta_1$ and $\Delta\beta_2$ are constant, but the correlation coefficient varies with the distance X, since it depends on the observed position on the image plane.
In order to evaluate c_{corr}, a uniform PDF of amplitude equal to the camera 1 resolution $\Delta\beta_1$ is centered on the observed tip-mass position at distance X, and a Monte Carlo simulation is employed to evaluate the errors v_1 and v_2 (see Eq.4.8), and then their correlation coefficient. The following Figures 4.4 and 4.5 show the correlation coefficient c_{corr} versus the distance X, for the cases of $X^{'} = 200\,\text{m}$ and $X^{'} = 600\,\text{m}$.

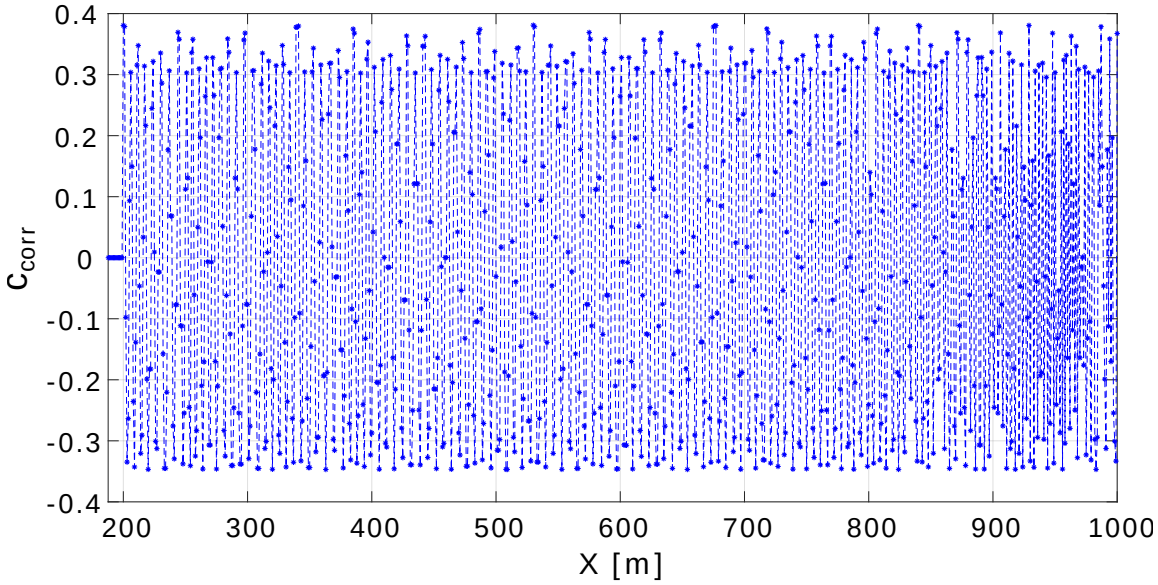

Figure 4.4: *Profile of correlation coefficient c_{corr} with respect to the tip-mass distance X along the optical axis, when using the parameter $X' = 200\,\mathrm{m}$.*

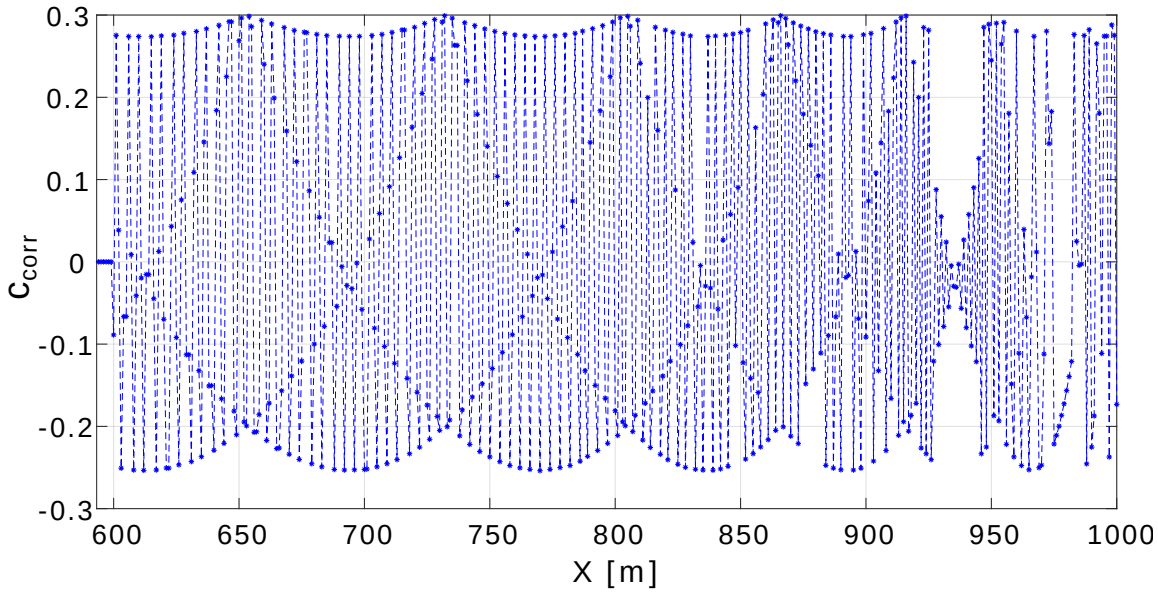

Figure 4.5: *Profile of correlation coefficient c_{corr} with respect to the tip-mass distance X along the optical axis, when using the parameter $X' = 600\,\mathrm{m}$.*

4.1.2 Second measurement scenario: direction and distance

In this second scenario, the measure of the tip-mass distance X along the optical axis is studied, combined with the measure of the angle β, already discussed in the previous scenario. In fact, the angular position β is measured here as described in Section 4.1.1.

Each camera is assumed with the intrinsic parameters of the first camera of Subsection 4.1.1 and the focal length is chosen such that the tip-mass always lies inside the camera's FOV throughout deployment.

This second analysis then focuses on the evaluation of the uncertainties obtained with two different methods of distance measurement. The two approaches, and related configurations, are:

1. A *stereo* vision system, with two cameras used to evaluate the tip-mass distance using triangulation.
2. A *monocular* vision system, measuring the tip-mass distance by means of fiducial markers placed on its surface.

Stereo system

The tip-mass distance can be measured by a stereo system relying on two cameras, mounted on Sylda, with parallel optical axes pointing towards the nominal direction of the tether at the end of deployment, i.e. the first body-frame axis X_B. Taking into account the geometry of Sylda, the baseline is considered as $b = 4\,\text{m}$. In this case of analysis, the tip-mass is modeled as a zero-dimensional point moving in the 3D space. The tip-mass is assumed to be always detectable by the stereo system.

The distance of the tip-mass along the optical axis of the stereo system can be computed as:

$$X = \frac{bf}{d} \tag{4.27}$$

where b is the stereo baseline, f is the focal length of the cameras and d is the disparity (i.e. distance in image coordinates between the projection of the tip-mass in left and right camera).
The standard uncertainty σ_f of the focal length f is evaluated considering an uniform PDF with amplitude 0.01 f (type B); the standard uncertainty σ_b of the baseline b comes from a uniform PDF of amplitude 5 mm (Type B, considering thermal expansion of materials); the standard uncertainty σ_r of the feature positions on the image plane comes from the sensor resolution. A uniform PDF is assumed for all the contribution to the uncertainty: consequently, the standard uncertainty of each contribution can be evaluated by means of Eq.4.4.

The overall uncertainty on the measured distance X is determined by means of the Kline-McClintock propagation formula:

$$\sigma_X = \sqrt{\left(\frac{\partial X}{\partial f}\sigma_f\right)^2 + \left(\frac{\partial X}{\partial b}\sigma_b\right)^2 + \left(\frac{\partial X}{\partial r}\sigma_r\right)^2} \tag{4.28}$$

Monocular system

In case of a *monocular* system used to measure the tip-mass distance, a single camera is used for each tip-mass, and mounted on Sylda. The optical axis is taken once again parallel to the X_B axis, that is the nominal direction of the tether when the deployment is finished.
In this measurement case, the tip-mass must be equipped with a planar pattern that consists of four features always detectable by the camera: three features are placed on a circumference of radius $\rho = 0.5\,\mathrm{m}$ to form an equilateral triangle, while a fourth is placed at the orthocenter. The coordinates of the feature points are known with respect to the tip-mass reference frame. In order to estimate the distance X from the detection of these features over time, the P3P solver proposed by Kneip et al. is employed (Ref. [22]). The uncertainty on the measured distance takes into account only the contribution of the sensor resolution σ_r. The Kline-McKlintock propagation formula is used to estimate the overall uncertainty on the measure: the partial derivatives of the distance with respect to the projections of the feature points on the image plane are computed.

Although the main objective is to estimate the tip-mass distance, the P3P solver returns an estimation of both the distance and the attitude of the tip-mass with respect to the body frame of the camera and Sylda, where it is mounted. Since the distance estimation accuracy is dependent on the attitude of the tip-mass, a parametric analysis is performed to evaluate the extent at which the attitude of the tip-mass affects the measurement performance of the vision system. The tip-mass attitude is assumed to be constant throughout deployment: this is reasonable assuming that the tether is connected to the tip-mass at its center of mass, and given that the deployment takes place above 2000 km, as described in Sec.3.6, where major perturbations are negligible.

4.2 Results from the vision system analysis

4.2.1 First measurement scenario: only direction

From the tip-mass nominal path during tether deployment, shown in Fig. 4.3, the profile of the angle $\beta(X)$ of the tip-mass during deployment can be computed. This profile is shown in Fig.4.6.

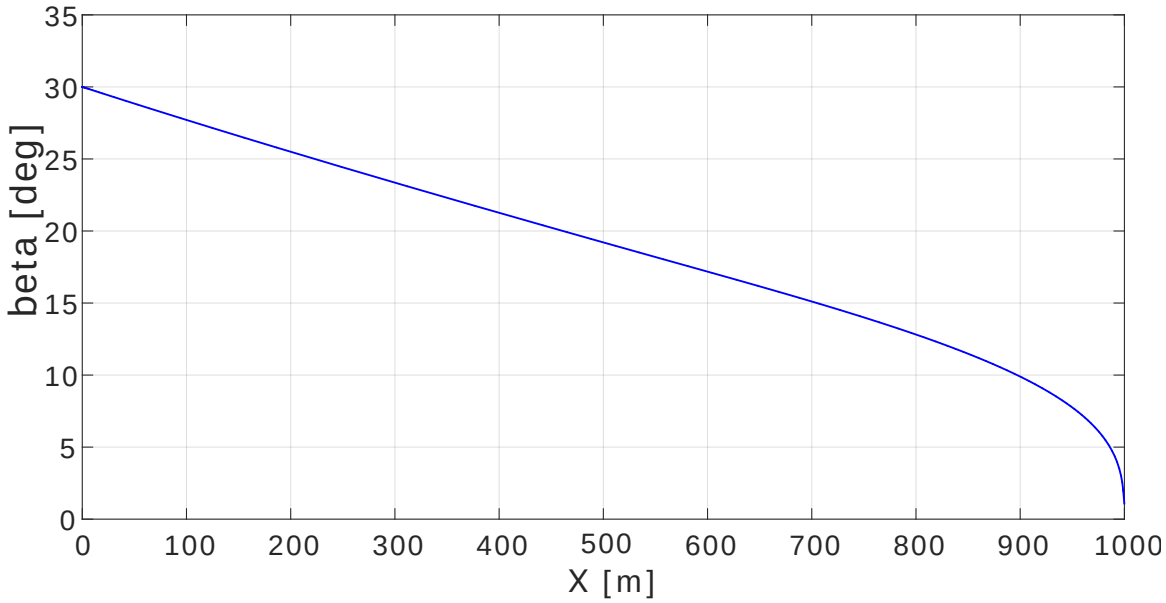

Figure 4.6: *Angular position β versus tip-mass distance X*

For $X_{min} < X < X^{'}$ only camera 1 measures the tip-mass angular position β, while for $X^{'} < X < X_{max}$ both cameras 1 and 2 can perform the measure. The final measurement can be obtained in two ways:

- considering the measure of only camera 2 for $X^{'} < X < X_{max}$ (continuous lines in Fig.4.7).
- considering both measures from cameras 1 and 2, and fusing them with the Kalman filter previously described (dashed lines in Fig.4.7).

The FOV of camera 1 is fixed by selecting X_{min}, and its measurement uncertainty is constant since it does not depend on $Z^{'}$ (see Fig. 4.7). Instead, the FOV of camera 2 and its measurement uncertainty, for $X > X^{'}$, depends on the distance $X^{'}$.

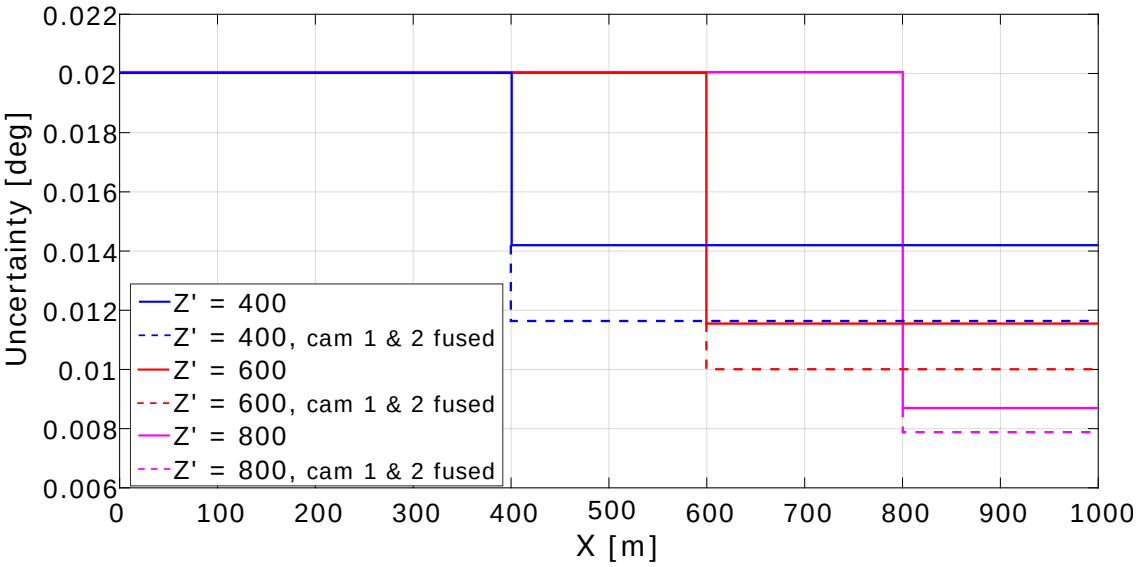

Figure 4.7: *Uncertainty in the measure of angle β (with level of confidence 99.7%), by camera 1 and camera 2, as function of the tip-mass distance X, and for different values of the optimization parameter $X^{'}$ (400 m, 600 m, 800 m); with dashed lines, it is shown the uncertainty, for $X > X^{'}$, when the measures from camera 1 and 2 are fused by using a Kalman filter.*

As shown in Fig. 4.7, by increasing $X^{'}$, both the uncertainty of camera 2 and that obtained from the fused measurements decrease, for $X > X^{'}$. However, at the same time, there is an increase in the measurement range where only camera 1 is used, i.e. for $X_{min} < X < X^{'}$. Camera 1 has a higher uncertainty than camera 2, and even higher than camera 1 and 2 fused together.
Therefore, the effect of changing $X^{'}$ must be evaluated considering the mean uncertainty, averaged in the entire distance range between X_{min} and X_{max}. The numerical results are illustrated in Fig.4.9, as a function of the optimization parameter $X^{'}$.

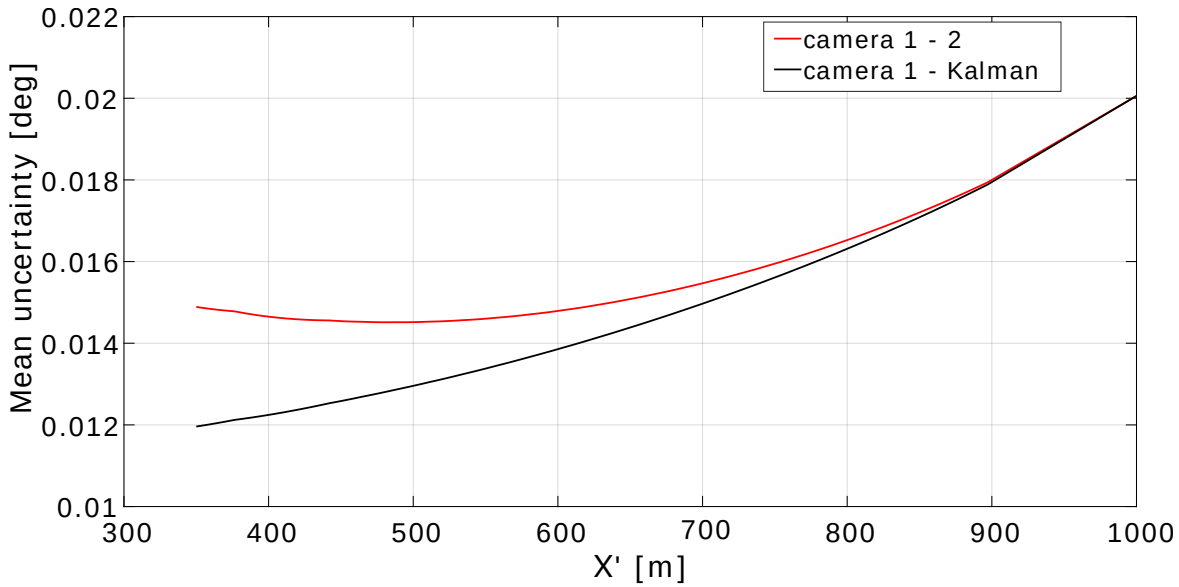

Figure 4.8: *Mean angular uncertainty (with level of confidence* 99.7%*), averaged on the tip-mass distance range between* X_{min} *and* X_{max}*, as function of the optimization parameter* $X^{'}$*. Two curves are plot: the red curve shows the case of camera 1 used for* $X_{min} < X < X^{'}$*, and camera 2 only for* $X^{'} < X < X_{max}$*; the black curve shows the case of camera 1 used for* $X_{min} < X < X^{'}$*, and both measures from camera 1 and 2, fused by a Kalman filter, for* $X^{'} < X < X_{max}$*.*

Following the procedure described in Sec.4.1.1, the intrinsic parameters of camera 1 and 2 are computed, as well as the optimal values of $X^{'}$, and the optimal uncertainties. These data are summarized in Table 4.1.
Comparing the results in the last column of Table 4.1, it is clear that the employment of a second camera improves the measurement performance by decreasing the mean uncertainty; additionally, there is a further improvement by using the Kalman filter to fuse the measurements from the two cameras, for $X > X^{'}$, and by selecting the optimal $X^{'}$.

Case	Intrinsic parameters and uncertainties					
	f_1	f_2	X'	σ_1	σ_2	σ_{mean}
X-range	-	-	-	X_{min}, X'	X', X_{max}	-
Cam 1	4.9	-	-	0.020	-	0.020
Cam 2	4.9	8.0	482	0.020	0.013	0.015
Cam 1-2 fused	4.9	7.0	350	0.020	0.012	0.012
Unit	mm	mm	m	deg	deg	deg

Table 4.1: *Optimization results*

When the correlation coefficient c_{corr} is taken into account, the angular uncertainties showed in the following figures are obtained. Two particular cases are depicted, corresponding to $X^{'} = 200\,\mathrm{m}$ (Fig.4.9) and $X^{'} = 600\,\mathrm{m}$ (Fig.4.10).

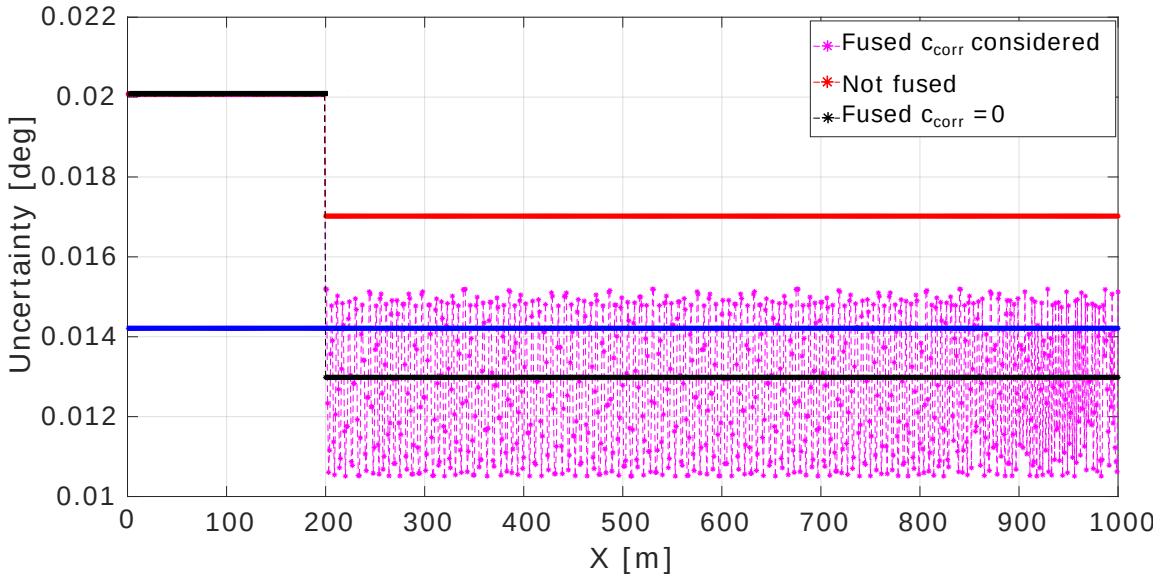

Figure 4.9: *Uncertainty in the measure of angular position with respect to distance X, when fusing the measures from the two cameras by means of a Kalman filter, after the distance $X^{'} = 200\,\mathrm{m}$.*

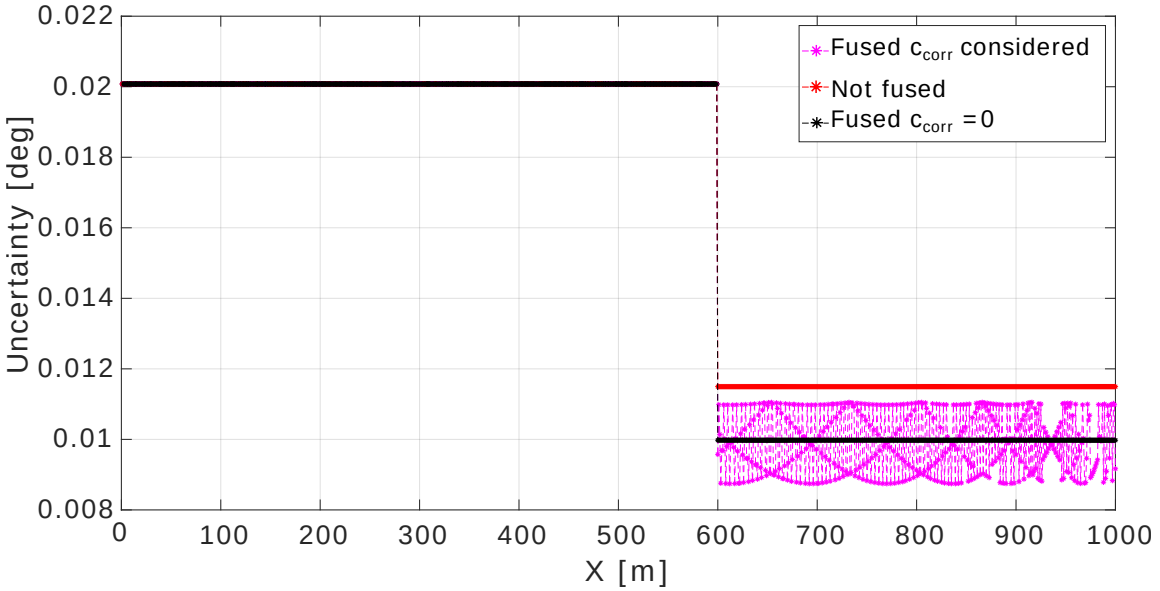

Figure 4.10: *Uncertainty in the measure of angular position with respect to distance X, when fusing the measures from the two cameras by means of a Kalman filter, after the distance $X^{'} = 600\,\mathrm{m}$.*

Performing the same analysis for all the values of $X^{'}$, and evaluating the mean angular uncertainty averaged on the entire range of X between X_{min} and X_{max}, the result showed in Fig.4.11 is obtained.

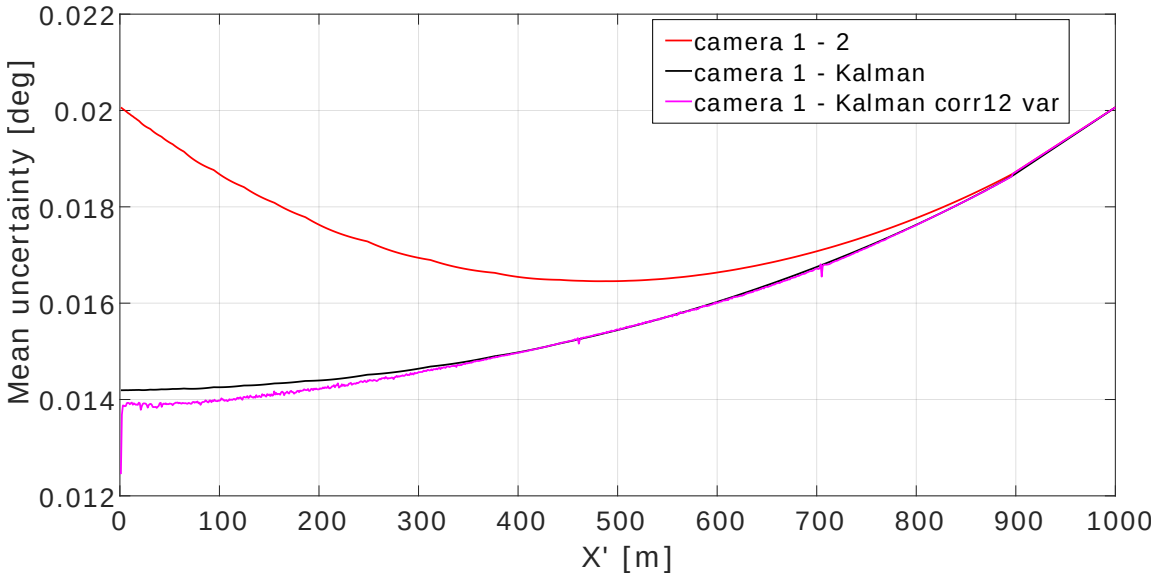

Figure 4.11: *Mean uncertainty on the measure of angle β with respect to the parameter X'. The black and red curves are the same as in Fig.4.8. The magenta-colored curve is the one accounting for the correlation between the two measures.*

Figure 4.11 shows only a marginal difference in mean uncertainty between the Kalman filter curve without correlation ($c_{corr} = 0$, black curve), and the curve accounting for correlation (in magenta). This means that considering the correlation coefficient c_{corr} yields only a little improvement with respect to the Kalman solution with c_{corr} always equal to zero. The optimization results of the parameter X' are similar too.

4.2.2 Second measurement scenario: direction and distance

All the results regarding the measure of the angle β of the tip-mass line of sight, described in Sec.4.2.1, are applicable to this case too.

This section focuses then on the uncertainty in the measurement of tip-mass distance X. Figure 4.12 shows the standard uncertainty σ_X on this measure, with respect to the actual tip-mass distance X. The black lines refer to the uncertainty associated with the *stereo* system: more specifically, the solid black line includes all the contributions to the standard uncertainty, while the dashed black line includes only the uncertainty σ_r due to the sensor resolution.
The red, green and blue lines refer to the uncertainty in distance measurements by the *monocular* vision system. The three curves refer to different, but constant, orientations of the tip-mass with respect to the camera frame (i.e. body frame): the roll angle Φ and yaw angle Ψ are both set to zero, while the pitch angle (Θ), that defines the rotation around the normal to the orbital plane, is switched between values of 0°, 30° and 60°.

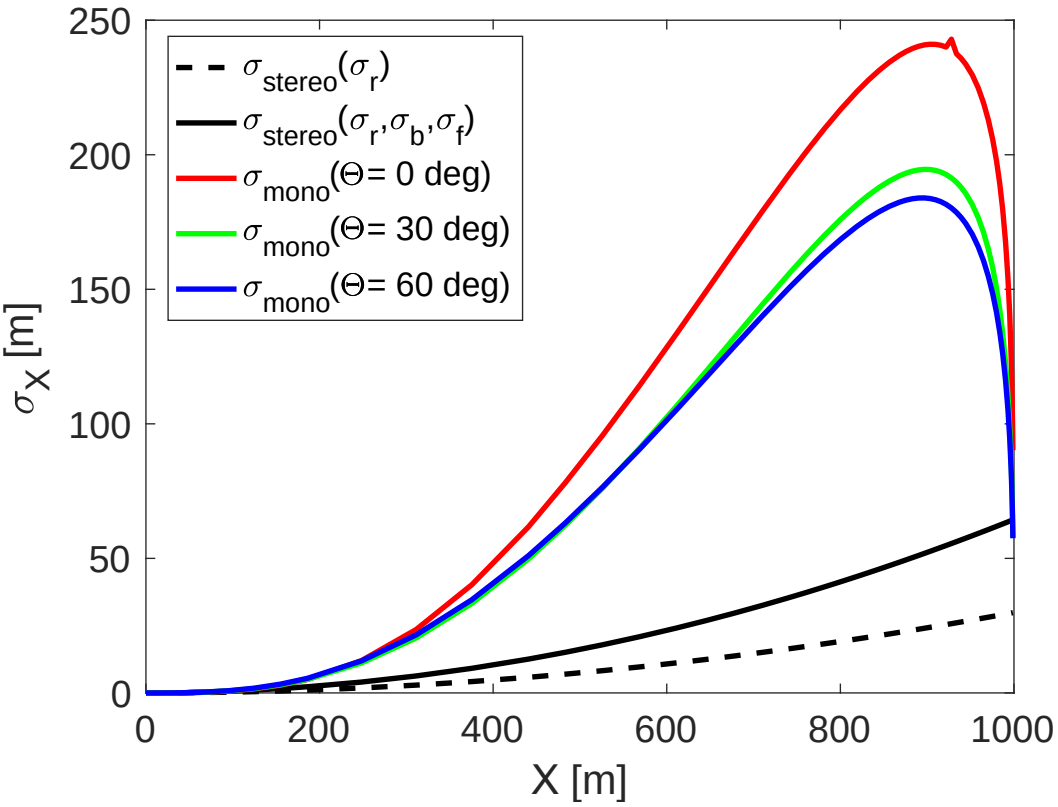

Figure 4.12: *Standard uncertainty on the measure of tip-mass distance X from Sylda. The solid black line corresponds to the* stereo *system taking into account all contributions to uncertainty; the dashed black line corresponds to the stereo system, considering only the contribution given by the sensor resolution. The colored lines show the uncertainties when using the* monocular *system, at various tip-mass orientations around the normal to the orbital plane: $\Theta = 0°$ (red), $\Theta = 30°$ (green) and $\Theta = 60°$ (blue).*

The uncertainty associated with the stereo system increases with the distance, while the uncertainty associated with the monocular system reveals to be highly dependent on the actual pose of the tip-mass. This behavior is summarized in Tab.4.2 where the peak values of uncertainty are reported for different values of roll and pitch angles of the tip-mass: the results also highlight that the uncertainty increases with the increase of the roll angle.

$\sigma_{\mathbf{max}}(\mathbf{\Phi}, \mathbf{\Theta})$ [m]	$\Theta = 0$ deg	$\Theta = 30$ deg	$\Theta = 60$ deg
$\Phi = 0$ deg	242.96	194.57	183.95
$\Phi = 15$ deg	248.09	230.51	213.97
$\Phi = 30$ deg	247.83	250.00	238.40
$\Phi = 45$ deg	256.39	265.25	259.58

Table 4.2: *Peak values of uncertainty on the measured tip-mass distance X, for different roll and pitch angles of the tip-mass, with respect to the camera-fixed reference frame (coincident with Sylda's body-frame).*

Figure 4.12 shows that the stereo system always outperforms the monocular system, i.e. it provides a lower uncertainty in the measure of all distances over the entire X range. Therefore, the stereo system results to be the optimal candidate, in the measure of the tip-mass distance X. Using the butterfly configuration on Sylda leads to using two stereo vision systems, one for each tip-mass at the end of each tether segment. Consequently, the total number of cameras mounted on Sylda is four cameras, with a baseline of about 4 m between the two cameras of each couple. The cameras can be mounted on the upper truncated-conical part of Sylda, in quadrature with respect to the two storage boxes for the tether segments, as shown in Fig. 4.13.

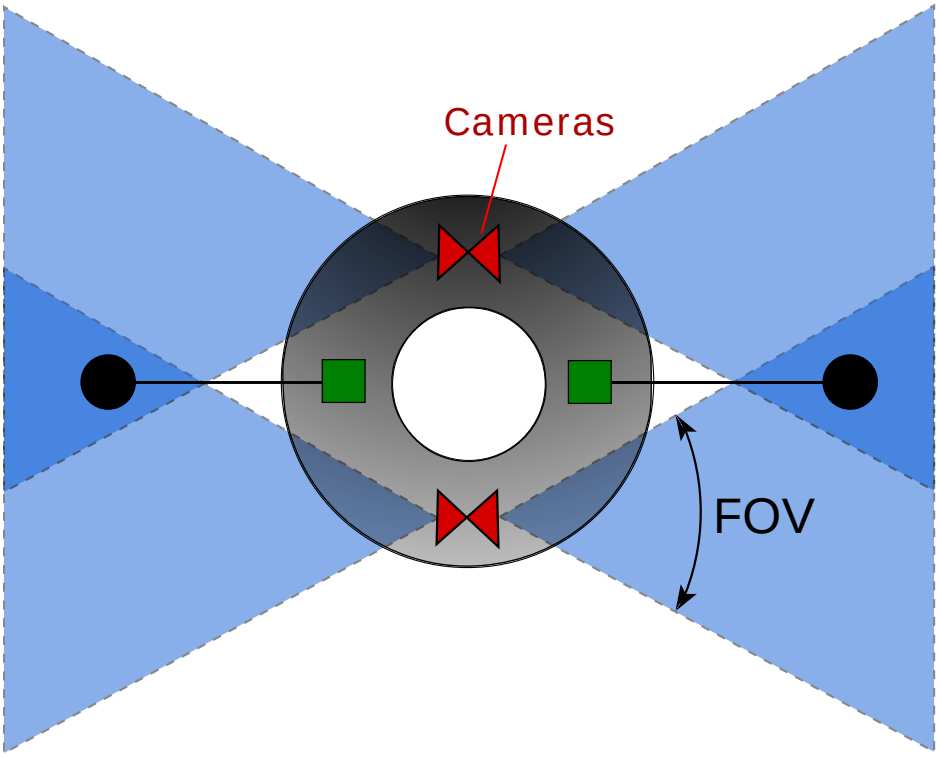

Figure 4.13: *View showing the two tether segments, and respective tip-masses, of the butterfly configuration being deployed on the orbital plane, released from their storage boxes. A stereo couple of camera is mounted, one for each tip-mass, on the upper part of Sylda, in quadrature with respect to the tether boxes, and with optical axis on the orbital plane.*

Chapter 5

Conclusions

The research is focused on the removal from orbit (i.e. deorbit), with a Bare Electrodynamic Tether (BET) system, of *Sylda*, a large dual-payload adapter that is released in Geostationary Transfer Orbit, during the launches of double-payloads to GEO with the *Ariane 5*. Deorbit is performed by dissipating the orbital energy of the object to remove, in this case Sylda, and consequently lowering the orbit until the object naturally degrades in the atmosphere during reentry. The dissipation is obtained with two drag forces: the Lorentz force, of electrodynamic origin, created by the interaction between the current running along the tether, made of electrons collected from the space plasma, and the geomagnetic field, thanks to the relative motion of the tether with respect to this field; the other drag contribution is the atmospheric drag, that is significantly increased by the presence of the tether due to its large exposed area. The tether that is considered in all the analyses presented in this research is 2 km long, 3 cm wide, and $100\mu m$ thick. The tether material must be conductive in order to enable the generation of an electrical current. Two materials are considered: pure Aluminum, or a Fiber-Reinforced Aluminum. The electrons collected by the tether from ambient plasma are ejected back to space, once arriving at the cathodic end, by using a *hollow cathode*, i.e. a small cylindrical device that only needs a very low mass of ionization propellant to work. Other technologies for the cathode, without need of ionization propellant, are under study, but they are not mature yet, and therefore they are not considered in this research.

The research is essentially subdivided into three main branches, that are: the analysis of deorbit with fully deployed tether, presented in Chapter 2; the analysis of predeorbit procedures, including tether deployment, presented in Chapter 3; the analysis of tether attitude detection with a vision system, presented in Chapter 4.

The deorbit is simulated using a dumbbell model where the tether and the body to which it is attached are co-moving together as a single rigid body, with tether straight and taut. This assumption is justified by the fact that the dynamics of a tethered system in a high eccentricity orbit, such as the Geostationary Transfer Orbit where Sylda is placed, is characterized by a *local* rotation of the system (tether plus Sylda) around its center of mass. This rotation increases over time during the deployment

of the two tether segments of the butterfly configuration, and then further increases during the following deorbit phase. This rotational motion creates, under certain initial conditions and design of the system, a positive tension that maintains the tether, subdivided in two segments, on a taut and straight configuration. The dynamics of the tethers tends to gradually force Sylda, that is detumbled before starting the deployment, to move together with the tether segments towards the end of deployment. This leads to a system made of Sylda plus the two tether segments that, at the start of deorbit, is already approximately rotating as a single rigid body. This fact allows the reasonable assumption of dumbbell model for all the deorbit simulations.

More in detail, the conclusive remarks that can be outlined from the analyses of deorbit, with fully deployed tether, are described below:

- a first campaign of deorbit analyses is performed with a *nondimensional* model, considering only the dynamics on the orbital plane, given their prominence with respect to the out-of-plane dynamics, and zero orbital inclination, given that Sylda is left on a GTO with very low inclination. The magnetic field is modeled as a dipole, and two perturbation forces are considered: the atmospheric drag, below 900 km, and the electrodynamic Lorentz drag created by the tether, below 2000 km, where the electron density of ambient plasma becomes significant. The aim of this first campaign of analyses is to get first information about the deorbit with a fast model, under reasonable assumptions. In particular, a focus is cast on the analysis of the tension created along the tether during deorbit, in order to evaluate the optimal design of the system, and optimal initial conditions to perform deorbit. The analyses highlighted that it is fundamental to start deorbit with a minimum angular velocity of the system of about 0.004 rad/s, in order to prevent tether slackness and instability during deorbit; at the same time, the initial angular velocity must not be too high, in order to avoid excessive tension and consequent tether breaking during deorbit. In order to minimize the risk of tether breaking, it is crucial to design the system with a *butterfly* configuration, i.e. to have the single electrodynamic tether subdivided in two segments that are deployed along opposite directions from Sylda. The lengths of each segment are calculated in order to minimize the displacement between the system's center of mass, and the *electrodynamic center of pressure*, during the entire deorbit. The *electrodynamic center of pressure* is the point where the resultant Lorentz force created by the electrodynamic tether acts. The employment of *Fiber-Reinforced Aluminum*, instead of pure Aluminum, is preferable inasmuch as it provides a larger safety margin against tether breaking, due to its higher mechanical properties, while still ensuring a high electrical conductivity.
  Furthermore, during this first batch of analyses, the profiles of various orbital parameters and the total deorbit time are computed: the orbital parameters evolve as expected, with an orbital eccentricity, apogee altitude, and perigee altitude always decreasing during deorbit, with a steep decrease in the last part of deorbit when the system is always orbiting below 2000 km, where dissipation forces are active. The total time to deorbit Sylda from its initial GTO results to be about 2.6–2.7 years, that is a time much lower than the 25 years prescribed by the main international guidelines as maximum time for removal of inactive

objects in Earth orbits.

- a second campaign of analyses is then performed, with a different model, called *hybrid*, since it combines part of the previous *nondimensional* model with parts of the former *dimensional* model. This new model includes the out-of-plane dynamics of the system, in order to have a more accurate analysis, and employs the *butterfly* configuration for the tethered system, as suggested from the previous campaign of analyses. An analysis is performed in order to estimate the lengths of the two tether segments to minimize the distance between the center of mass of the orbit and the electrodynamic center of pressure, resulting in about 1200 m for the first segment, and 800 m for the second. All the orbital parameters, including orbital inclination, are considered variable over time, and a more accurate model of geomagnetic field is used, with higher harmonics. The dumbbell model is kept, but given that the tether is subdivided in two segments deployed along opposite directions, it is a *double-dumbbell* model. This second analysis campaign provided more accurate profiles of all the variable orbital parameters during deorbit, and a more accurate estimate of the total time to deorbit Sylda, that results to be approximately 818 days, i.e. about 2.24 years. Once again, a time much lower than the 25 years prescribed by the main international guidelines for debris removal.

Another part of research is dedicated to the study of the storage and mounting on Sylda of the deorbit system, and to all the procedures to be performed before starting the deorbit. In summary, this analysis returned the following conclusions:

- The storage of the two tether segments of the butterfly system is discussed, opting for a storage on separate spools for the two segments, but electrically connected on Sylda. Each tether segment is deployed independently from the other, with a dedicated small electrical motor mounted inside the spool. The two tether reels are stored in protective boxes and are mounted symmetrically with respect to Sylda's longitudinal axis, in order to minimize the displacement of the center of mass with respect to the default configuration of Sylda mounted inside the Ariane 5 without a deorbit system.
- In order to achieve a correct deployment, without risk of interference between the tethers and the body of Sylda, the residual angular velocity of Sylda, must be minimized. Sylda, after its release in GTO, rotates around the three axes of the body frame, with an angular velocity that is reported to be around 0.006 rad/s. This angular velocity is due to the unavoidable error in the release system that separates Sylda from the dual-payload. In order to zero this angular velocity, a set of *magnetic torquers* is proposed as devices to be mounted on Sylda, in order to completely detumble it around the three axes. Magnetic torquers attached to Sylda are slender cylinders of diameter of 2-3 cm and length of 0.75-1.5 m, with very low mass with respect to Sylda, and requiring only few watts of power, that could be provided by a small primary battery. These torquers create a magnetic moment by exploiting the current running on the cylindrical coil; this magnetic moment interacts with the geomagnetic field and creates a torque that counteracts the rotational motion of Sylda. Computations return that a complete detumbling can be achieved already during the first passage of Sylda across the

perigee region, after its release at the apogee of the GTO; in fact, magnetic torquers are most effective at low altitudes, where the geomagnetic induction is stronger.

- The deployment of the two tether segments is then studied, considering it to take place only on the orbital plane. The tethers are deployed with an angle of about 30–45° with respect to the first axis of the body frame, coincident by assumption with the optical axis of the vision system to track the tip-mass at the end of each tether. This angle is selected in order to have, at the end of deployment, the tethers aligned as much as possible to the first axis of the body frame, and co-rotating together with Sylda. The deployment is simulated considering the rotation of Sylda as related to, but not coincident, to the rotation of the two tether segments. Moreover, the two tether segments can rotate with different angles around their attachment point on Sylda, with respect to the radial direction taken as reference. Three different simulations are run for three cases of deployment along the initial GTO orbit of Sylda: deployment at apogee; deployment at perigee; deployment at mid-way between perigee and apogee, at altitudes such that drag forces are negligible. In all cases, the tether release velocity profile is a quasi-uniform profile, i.e. the tether is released at a constant velocity until a point at which the velocity gradually decreases until reaching zero at the end of deployment, with zero acceleration too, in order to prevent a mechanical shock on the tether that could break it.
  Deployment at perigee turns out to be the worst case, due to the presence of perturbations that cause an excessive oscillation between the tethers and Sylda's body, with the risk of the tether to wrap around Sylda instead of being deployed correctly. Deployment at apogee and at mid-way are both viable, since Sylda and the tethers do not interfere, and tend to align the end of deployment. Afterwards, they gradually start to co-rotate together approximately as a single rigid body, which is the optimal condition at which to start deorbiting. At last, the optimal location where to start the deployment, that only takes a few minutes to complete (the tether release velocities are around 1.2-1.8 m/s), is at mid-way along the orbit, i.e. after first crossing the perigee zone (where complete detumbling takes place) and while going back towards the apogee, at altitudes always above 2000 km. In this way, perturbations forces of atmospheric and Lorentz drag during deployment are negligible, and at the same time Sylda is more stable at the start of deployment, having just been detumbled.

Lastly, a study is performed regarding the tether's attitude detection and control, with two tether segments in *butterfly* configuration. In fact, during deployment, the attitude of the tethers is not fully stable yet, so it is fundamental to provide the deorbit system with a sufficient detection and control capability. These are the conclusions that this analysis returned:

- The control of tethers attitude can be accomplished by regulating the tether release velocity with a small electrical motor that rotates the spool around which each tether segment is reeled. The control of tether attitude is also improved by the feedback coming from a vision system that detects the attitude of the tether by tracking the tip-mass. From the error in tether's attitude with respect to a

nominal profile, the electrical motor can act upon the tether release velocity in order to compensate this error.

- The attitude detection of the tether segments can be achieved with a vision system, that measures the angular position on the orbital plane, and the distance from Sylda along the optical axis, of the tip-mass at the end of each tether segment, modeled again as a dumbbell. In fact, the tether segments can be kept straight and taut, during deployment, with an accurate control of their release velocity; thus, the dumbbell model is applicable. The deployment, as previously stated, is performed on the orbital plane.
  A typical deployment profile is employed as input for the uncertainty analysis of the measure provided by two possible configurations of vision system: a *monocular* system, and a *stereo* system.
  Two scenarios are analyzed: a first one, where only the angular position of the tip-mass is evaluated; a second one, that investigates the uncertainty in the measure of both tip-mass angular position and distance along the optical axis.
  The main outcome from the analysis of the first scenario is that the minimum uncertainty in the measure, and then the maximum accuracy, is achieved by using two cameras for each tip-mass, with zero baseline (i.e. not a stereo system) and by fusing the measures from the two cameras with a Kalman filter, starting at a certain tip-mass minimum distance until the end of deployment.
  In the second scenario, a stereo and a monocular vision systems are analyzed and compared in the tip-mass distance measurement: the main result is that the stereo system outperforms the monocular system, providing a lower uncertainty in the measure, throughout deployment.

Appendix A

Dimensional vs. normalized parameters used in the *nondimensional* model for deorbit simulations

The table posted below shows all the parameters used in Sec.2.1.1 in their dimensional and corresponding normalized form. The generic dimensional parameter x has its normalized correspondent in $\bar{x}$, i.e. with a bar over the letter. The only exceptions to this notations are the parameters Λ_t and ϕ, that are nondimensional by definition. Using a dimensional coefficient C, it is possible to restore the dimensional variable, as follows:

$$x = C\bar{x} \tag{A.1}$$

Dimensional Parameter	**Unit**	**Normalized parameter**	**Coefficient C**
Tether length L_t	m	$\overline{L}_t$	Characteristic length L_*
Tether mass m_t	kg	$\overline{m}_t$	Total mass of the system $m = m_A + m_t + m_C$
Anodic tip mass m_A	kg	$cos^2\phi - \frac{\Lambda_t}{2}$	Total mass of the system m
Cathodic tip mass m_C	kg	$sin^2\phi - \frac{\Lambda_t}{2}$	Total mass of the system m
Radial location of center of mass $\boldsymbol{r}_G$	m	$\bar{\boldsymbol{r}}_G$	Earth radius R_E
Orbital velocity of center of mass $\boldsymbol{v_G}$	$\frac{\text{m}}{\text{s}}$	$\bar{\boldsymbol{v}}_G$	$\sqrt{\frac{\mu_E}{R_E}}$
Semimajor axis of orbit a	m	$\bar{a}$	Earth radius R_E
Time t	s	τ	$\sqrt{\frac{R_E^3}{\mu_E}}$
Force **F**	N	$\overline{\boldsymbol{F}}$	$\frac{m\,\mu_E}{R_E^2}$
Torque about point P: $\boldsymbol{M}_P$	Nm	$\overline{\boldsymbol{M}}_P$	$\frac{I_P \mu_E}{R_E^3}$

Table A.1: *Parameters used in the* nondimensional *model presented in Sec.2.1.1.*

where μ_E is the Earth gravitational parameter; R_E is the Earth radius; I_P is the moment of inertia of the system about the axis orthogonal to the orbital plane and passing through the generic point P; L_* is the *characteristic length* of the tether that is defined, under the assumption of Orbital Motion Limited (OML) current collection, as:

$$L_* = \left[\frac{9\pi^2}{128}\frac{m_e \sigma_t^2 E_t h_t^2}{q_e^3 N_e^2}\right]^{1/3} \tag{A.2}$$

where m_e and q_e are electron mass and charge; N_e is the electron number density from ionospheric plasma; h_t is the thickness of tether; σ_t is the electrical conductivity of the tether; E_t is the electrical field component along the tether.

Appendix B

Reference frames

A list is presented below with all the reference systems employed throughout this PhD thesis:

1. **Spherical Geocentric Equatorial Rotating (SGER)** system. Unit vectors ($\boldsymbol{u}_r$, $\boldsymbol{u}_\delta$, $\boldsymbol{u}_\phi$). $\boldsymbol{u}_r$ is pointing from the Earth's center to the system's center of mass; $\boldsymbol{u}_\delta$ is pointing towards the co-latitude direction, tangential at the system's center of mass location, where the co-latitude angle is measured from the North Pole towards the South Pole; $\boldsymbol{u}_\phi$ is the longitude direction at the generic location of the system's center of mass, pointing Eastward from the Greenwich meridian. This is the reference system in which the coordinates of the geomagnetic induction vector $\boldsymbol{B}$ are computed from the IGRF database, as described in Appendix D.2.

2. **Perifocal frame (PQW)** with unit vectors $\boldsymbol{u}_p$, $\boldsymbol{u}_q$, $\boldsymbol{u}_w$. $\boldsymbol{u}_p$ is directed along the periapse of the orbit and pointing such that it goes from focus to periapse. $\boldsymbol{u}_w$ is directed along the normal to the orbital plane and pointing such that it creates a right-hand triad following the direction of orbital motion. $\boldsymbol{u}_q$ is such that $\boldsymbol{u}_p \times \boldsymbol{u}_q = \boldsymbol{u}_w$.

3. **Orbital frame (RSW)**, with unit vectors $\boldsymbol{u}_r$, $\boldsymbol{u}_s$, $\boldsymbol{u}_w$. $\boldsymbol{u}_r$ is pointing from the Earth's center towards the system's center of mass along the orbital path; $\boldsymbol{u_s}$ is rotated of 90° with respect to $\boldsymbol{u_r}$, on the orbital plane, and pointing in the direction of increasing true anomaly; $\boldsymbol{u}_w = \boldsymbol{w}$ is directed along the normal to the orbital plane and pointing such that it follows the right-hand rule with the other two unit vectors, i.e. $\boldsymbol{u}_r \times \boldsymbol{u}_s = \boldsymbol{u}_w$.

4. **Body frame (B)**, with unit vectors $\boldsymbol{u}_\xi$, $\boldsymbol{u}_\eta$, $\boldsymbol{u}_\zeta$. $\boldsymbol{u}_\zeta$ is aligned with the longitudinal axis of Sylda; $\boldsymbol{u}_\xi$ is aligned with the optical axis of the vision system, that lies on the orbital plane after detumbling of Sylda, and throughout the deployment of the two tether segments of the butterfly configuration; $\boldsymbol{u}_\eta$ completes the orthonormal right-hand triad.

Appendix C

Atmospheric drag computation

The *atmospheric drag* is a force opposite to the vector of relative velocity $\boldsymbol{v}_{rel}$ between the orbiting body and the atmosphere. It can be reasonably assumed that the atmosphere is co-rotating with the Earth. Therefore:

$$\boldsymbol{v}_{rel} = \boldsymbol{v} - \boldsymbol{v}_{atm}, \tag{C.1}$$

$$\boldsymbol{v}_{atm} = \boldsymbol{r} \times \boldsymbol{\Omega}_E \tag{C.2}$$

where $\boldsymbol{v}$ is the orbital velocity of the object to deorbit; $\boldsymbol{r}$ is the local radial position vector from the Earth's center; $\boldsymbol{v}_{atm}$ is the linear local velocity of the terrestrial atmosphere; $\boldsymbol{\Omega}_E$ is the spin rotational velocity of the Earth.

The atmospheric drag force $\boldsymbol{F}_{atm}$, opposite to the relative velocity vector, can be then computed as:

$$\boldsymbol{F}_{atm} = -\frac{1}{2}\rho_{atm} c_d \left(A_t + A_{sc}\right) v_{rel} \boldsymbol{v}_{rel} \tag{C.3}$$

being ρ_{atm} the local atmospheric density; A_t the frontal area of the tether (if more than one tether segment is used, this is the sum of frontal areas of each tether segment); A_{sc} is the frontal area of the deorbited body (Sylda in the specific case of this research). As *frontal area*, it is considered the *aerodynamic drag exposed area*, i.e. the surface of the object projected on the plane orthogonal to the drag force vector. It is important to point out that the system during deorbit is continuously rotating around its center of mass. Consequently, the area exposed to atmospheric drag continuously changes too. In the codes, it is decided to use a constant drag area, but averaged accounting for its variation during one full rotation of the system.

The atmospheric drag is considered to be present only for altitudes lower than 900 km. Above 900 km, the atmospheric density becomes so low that the perturbation due to atmospheric drag is negligible. At the altitudes at which deorbit takes place, before the objects reenters in the atmosphere, i.e. always above 150 km, a *free molecular flow*

takes place: this means that particles of the atmosphere interact one by one with the orbiting body, and therefore the incident flow of particles is not disturbed by the body itself. In such conditions, the aerodynamic drag coefficient can be chosen in the range between 2.0 and 2.4. In all the codes developed for this research, a mean value of $c_d = 2.2$ is used.

The profile of atmospheric density is imported using the *Jacchia-Bowman 2008 (JB-2008)* empirical model (Ref. [2]). Only the variation with orbital altitude is considered. Values are taken from Ref. [2], for altitude steps between 100 and 900 km. From this set values, shown in TableC.1, a much higher number of values is obtained using an interpolation algorithm, and imported in the codes, in the condition of moderate Solar and geomagnetic activity. The resulting atmospheric density profile is shown in Fig. 2.2.

H (km)	Low activity	Moderate activity	High activity (long term)	High activity (short term)
100	5.31E-07	5.47E-07	5.44E-07	5.43E-07
120	2.18E-08	2.40E-08	2.45E-08	2.46E-08
140	3.12E-09	3.98E-09	4.32E-09	4.45E-09
160	9.17E-10	1.36E-09	1.54E-09	1.60E-09
180	3.45E-10	6.15E-10	7.40E-10	7.77E-10
200	1.47E-10	3.17E-10	4.10E-10	4.38E-10
220	6.96E-11	1.77E-10	2.46E-10	2.70E-10
240	3.54E-11	1.05E-10	1.56E-10	1.77E-10
260	1.88E-11	6.47E-11	1.04E-10	1.21E-10
280	1.03E-11	4.12E-11	7.12E-11	8.57E-11
300	5.86E-12	2.69E-11	5.00E-11	6.22E-11
320	3.40E-12	1.80E-11	3.59E-11	4.60E-11
340	2.02E-12	1.23E-11	2.61E-11	3.45E-11
360	1.22E-12	8.48E-12	1.93E-11	2.63E-11
380	7.46E-13	5.95E-12	1.44E-11	2.02E-11
400	4.63E-13	4.22E-12	1.09E-11	1.57E-11
420	2.92E-13	3.02E-12	8.32E-12	1.23E-11
440	1.87E-13	2.18E-12	6.40E-12	9.69E-12
460	1.21E-13	1.59E-12	4.96E-12	7.70E-12
480	8.04E-14	1.17E-12	3.87E-12	6.16E-12
500	5.44E-14	8.60E-13	3.04E-12	4.95E-12
520	3.77E-14	6.39E-13	2.40E-12	4.01E-12
540	2.68E-14	4.77E-13	1.91E-12	3.25E-12
560	1.96E-14	3.58E-13	1.52E-12	2.66E-12
580	1.47E-14	2.71E-13	1.22E-12	2.18E-12
600	1.14E-14	2.06E-13	9.82E-13	1.79E-12
620	9.10E-15	1.57E-13	7.93E-13	1.48E-12
640	7.41E-15	1.20E-13	6.43E-13	1.23E-12
660	6.16E-15	9.28E-14	5.22E-13	1.02E-12
680	5.22E-15	7.19E-14	4.25E-13	8.49E-13
700	4.50E-15	5.60E-14	3.47E-13	7.09E-13
720	3.93E-15	4.40E-14	2.84E-13	5.94E-13
740	3.48E-15	3.48E-14	2.34E-13	4.98E-13
760	3.10E-15	2.79E-14	1.92E-13	4.19E-13
780	2.79E-15	2.26E-14	1.59E-13	3.54E-13
800	2.53E-15	1.85E-14	1.32E-13	2.99E-13
820	2.30E-15	1.53E-14	1.10E-13	2.54E-13
840	2.11E-15	1.28E-14	9.21E-14	2.16E-13
860	1.94E-15	1.08E-14	7.72E-14	1.84E-13
880	1.78E-15	9.27E-15	6.50E-14	1.57E-13
900	1.65E-15	8.01E-15	5.49E-14	1.35E-13

Figure C.1: *Atmospheric density in* $\mathrm{kg\,m^{-3}}$ *with respect to orbital altitude in* km. *Three columns are posted, each one respectively referring to low, moderate, and high (long term and short term) Solar and geomagnetic activity.*

Appendix D

Earth's Magnetic Field

The three components of the geomagnetic induction $\boldsymbol{B}$ are derived, for all computations presented in Sec.2.2 and 3.5, from data in the *IGRF-11* reference model. A code is written to compute the geomagnetic field vector components B_r, B_δ, B_ϕ in the SGER reference frame (r, δ, ϕ) (see Appendix B for a description of this coordinate system). B_r is the component along the local radial direction (positive if pointing outwards from the Earth's center); B_δ is the component in the co-latitude direction (positive if pointing southward); B_ϕ is the component in the longitude direction (positive if pointing eastward from the reference Greenwich meridian). A major reference regarding the geomagnetic field computation is Wertz (Ref. [48]).

These are the inputs used for the computation of the geomagnetic induction vector:

- the instantaneous radial distance $\boldsymbol{r}$ of the system's center of mass from the Earth's center
- the co-latitude δ, i.e. the angle from the Earth's spin axis to the vector $\boldsymbol{r}$. This means that the unit vector $\boldsymbol{u}_\delta$ is positive in southward direction
- the longitude angle ϕ measured eastward from the Greenwich reference meridian.
- the time (in decimal days) starting from January 1^{st}, 2010.

D.1 Dipole Model

The simplest model for the geomagnetic field is the *dipole* model, with dipole axis tilted of an angle $\delta_m \cong 11.5°$ with respect to the Earth's spin axis; the dipole model corresponds to considering only the contributions of spherical harmonics of degree 1, and orders 0 and 1, in the analytic calculation of magnetic field. It is important to remember, in order to assign the correct direction to magnetic field vectors, that the polarity of the magnetic dipole is opposite to the geographic polarity, i.e. the geomagnetic South Pole is near to the geographic North Pole, and the geomagnetic North Pole is near to the geographic South Pole. The geomagnetic field lines are oriented such that they exit from the North magnetic pole (close to the South geographic pole)

and go towards the South magnetic pole (close to the North geographic pole). Hence, the local magnetic induction vector $\boldsymbol{B}$ points as shown in Fig.D.1.

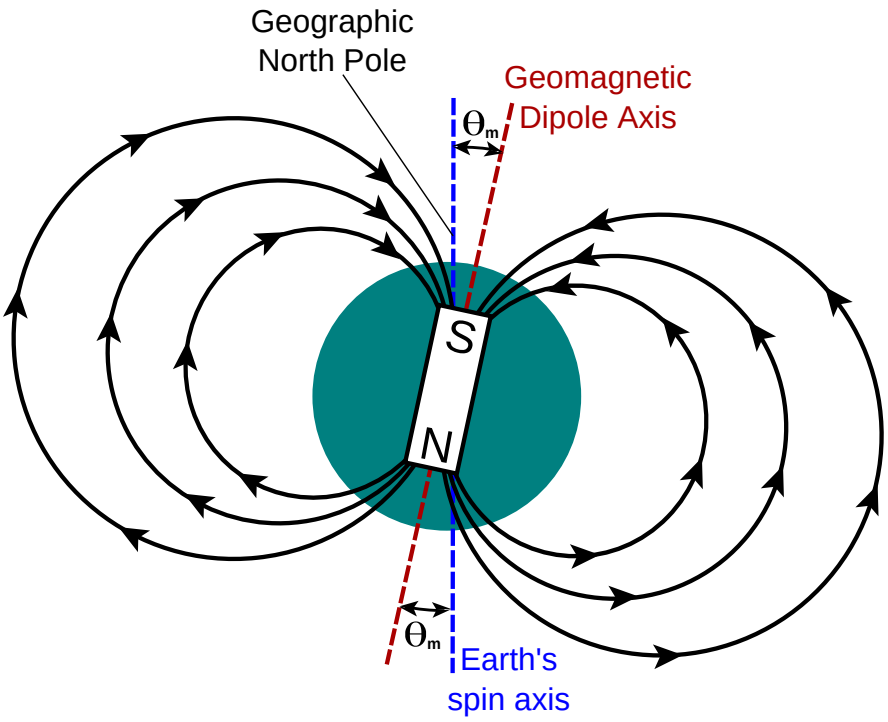

Figure D.1: *Geomagnetic dipole model*

The dipole model of geomagnetic field is used in the model presented in Sec.2.1.

D.2 Higher Harmonics model

In the analyses presented in Sec.2.2 and 3.5, a full analytical model is employed for the computation of geomagnetic induction, with all the higher harmonics available in the *IGRF-11* database.
The geomagnetic induction vector is computed as the gradient of a potential function that, in turn, is derived from a series of spherical harmonics. An infinite number of these harmonics would be required to achieve the exact value of the magnetic field components, at every location in space. The notation system from Ref. [48] is adopted for the equations presented in this section.

The magnetic field vector $\boldsymbol{B}$ is computed as:

$$\boldsymbol{B} = -\nabla V \tag{D.1}$$

i.e. $\boldsymbol{B}$ is the negative of the spatial gradient of a scalar potential function V, that can be in turn computed as:

$$V = \sum_{n=1}^{\infty} \sum_{m=0}^{n} V^{n,m} \tag{D.2}$$

where

$$V^{n,m} = a \left(\frac{a}{r}\right)^{n+1} \left[g^{n,m} cos(m\phi) + h^{n,m} sin(m\phi)\right] P^{n,m} \tag{D.3}$$

and

- $a = 6371.2\,\text{km}$ is the mean radius of the Earth
- r is the magnitude of $\boldsymbol{r}$, i.e. the position vector from the center of the Earth to the generic point in space, where the magnetic field vector is computed.
- ϕ is the geographic longitude measured Eastward from the Greenwich meridian.
- n is the degree of the specific spherical harmonic under consideration
- m is the order of the specific spherical harmonic under consideration
- $g^{n,m}$ and $h^{n,m}$ are Gauss-normalized coefficients of degree n and order m
- $P^{n,m}$ are Gauss-normalized functions, derived from Legendre polynomials. They are functions of δ, namely the co-latitude (or co-elevation) of generic point in space (i.e. $90° - latitude$)

It is defined as *spherical harmonic* of *degree* n and *order* m, the single contribution to $\boldsymbol{B}$, i.e.:

$$\boldsymbol{B^{n,m}} = -\boldsymbol{\nabla} V^{n,m} \tag{D.4}$$

Therefore:

$$\boldsymbol{B} = \sum_{n=1}^{\infty} \sum_{m=0}^{n} \boldsymbol{B^{n,m}} \tag{D.5}$$

Gauss-normalized coefficients are obtained from *Schmidt Quasi-Normalized* (or *Semi-Normalized*) coefficients, extracted from the *International Geomagnetic Reference Field (IGRF)* database. It is used the 11th Generation IGRF, with values of coefficients computed at January 1st, 2010. This data was released by the International Association of Geomagnetism and Aeronomy (IAGA) in December 2009. The values of all coefficients reported in the IGRF model are determined experimentally.

Schmidt Quasi-Normalized, (or *Semi-Normalized*), coefficients up to the 13th degree and order ($n_{max} = 13$ and $m_{max} = 13$) are used in the codes, in units of nT (nanotesla). *Schmidt quasi-normalized* coefficients are converted to *Gauss-normalized* coefficients. The *Schmidt quasi-normalized* coefficients are denoted with a tilde sign on

the top and by placing only m as superscript, and n as subscript ($\widetilde{g_n^m}$ and $\widetilde{h_n^m}$), in order to distinguish them from the *Gauss-normalized* coefficients ($g^{n,m}$ and $h^{n,m}$). The conversion from *Schmidt quasi-normalized* to *Gauss-normalized* coefficients is performed using the following equations:

$$g^{n,m} = S_{n,m}\widetilde{g_n^m} \tag{D.6}$$

$$h^{n,m} = S_{n,m}\widetilde{h_n^m} \tag{D.7}$$

where factors $S_{n,m}$ are independent of local spherical coordinates r, δ, ϕ of the generic point where the magnetic field is computed. The same is true also for the *Schimdt quasi-normalized* coefficients and, consequently, for the *Gauss-normalized* coefficients. Therefore, the code has to perform these operations, described up to now, only once in an entire simulation, i.e. not for every single location covered by the system during deorbit. This is an advantage granted by the employment of these coefficients, that enable a more efficient computational method.

$S_{n,m}$ factors are calculated using the following recursive equations:

$$S_{0,0} = 1 \tag{D.8}$$

$$S_{n,0} = S_{n-1,0}\left[\frac{2n-1}{n}\right] \qquad n \geq 1 \tag{D.9}$$

$$S_{n,m} = S_{n,m-1}\sqrt{\frac{(n-m+1)(\delta_m^1+1)}{n+m}} \qquad m \geq 1 \tag{D.10}$$

where δ_m^1 is the *Kronecker delta* defined as $\delta_i^j = 1$ if $i = j$ and $\delta_i^j = 0$ otherwise. In this equation $j = 1$; therefore, only when $m = 1$ the delta is $\delta_1^1 = 1$. In all other cases $\delta_{m\neq 1}^1 = 0$.

The Gauss functions $P^{n,m}$ can be recursively obtained too, with a similar procedure:

$$P^{0,0} = 1 \tag{D.11}$$

$$P^{n,n} = sin(\delta)P^{n-1,n-1} \tag{D.12}$$

$$P^{n,m} = cos(\delta)P^{n-1,m} - K^{n,m}P^{n-2,m} \tag{D.13}$$

where

$$K^{n,m} = 0 \qquad n = 1 \tag{D.14}$$

$$K^{n,m} = \frac{(n-1)^2 - m^2}{(2n-1)(2n-3)} \qquad n > 1 \tag{D.15}$$

It is set the maximum *degree* of contributing spherical harmonics, to be considered in the analysis, as n_{max}. In the IGRF datasheet the maximum degree is $n = 13$, but n_{max} can be even lower than 13. It is used $n_{max} = 13$, i.e. the maximum degree of spherical harmonics available. For each degree value n, there is a set of values of order m ranging from 0 to n, for g coefficients; from 1 to n for h coefficients. The maximum value of order m equals the maximum value of n considered in the calculation, i.e. $m_{max} = n_{max} = 13$.

By implementing the gradient in spherical coordinates, the magnetic field components can be eventually calculated with the following equations:

$$B_r = -\frac{\partial V}{\partial r} = \sum_{n=1}^{n_{max}} \left(\frac{a}{r}\right)^{n+2} (n+1) \sum_{m=0}^{n} \left[g^{n,m} cos(m\phi) + h^{n,m} sin(m\phi)\right] P^{n,m} \tag{D.16}$$

$$B_\delta = -\frac{1}{r}\frac{\partial V}{\partial \delta} = -\sum_{n=1}^{n_{max}} \left(\frac{a}{r}\right)^{n+2} \sum_{m=0}^{n} \left[g^{n,m} cos(m\phi) + h^{n,m} sin(m\phi)\right] \frac{\partial P^{n,m}}{\partial \delta} \tag{D.17}$$

$$B_\phi = -\frac{1}{r sin\delta}\frac{\partial V}{\partial \phi} = -\frac{1}{sin\delta} \sum_{n=1}^{n_{max}} \left(\frac{a}{r}\right)^{n+2} \sum_{m=0}^{n} m \left[-g^{n,m} sin(m\phi) + h^{n,m} cos(m\phi)\right] P^{n,m} \tag{D.18}$$

The computation is performed using a recursive method in order to improve code efficiency, and the expressions are such that singularity is avoided when the magnetic field is evaluated at points that lie on the polar axis. The components B_r, B_δ and B_ϕ are computed, using the equations described above, in the SGER system (see Appendix B).

Appendix E

Ionosphere model and electron density

For the computation of the current generated along the electrodynamic tether, it is necessary to know the value of *electron density* N_e at every location along the deorbit path. Values of N_e are extracted from the *International Reference Ionosphere (IRI) 2007* database. The *electron density* is variable over time, even on the same specific location. The major influencing factor is the *solar flux*. A higher solar flux leads to higher *electron densities*. The main input requested by the code to extract the electron density profile, is the precise Julian Day (JD) at which to compute the *electron density* data set.

A Julian Day is then chosen such that the solar flux on that day is as close as possible to an average value over one complete solar cycle. Since deorbit times, with the tethered system considered in this thesis, range between approximately 2.2 to 2.7 years, it can be reasonably assumed that the average solar flux during deorbit is equal to the mean solar flux over an entire solar cycle (lasting about 11 years).

An average value of $F10.7$ index is found from literature, i.e. $F10.7 \approx 145 s.f.u.$. The $F10.7$ index gives the measure of the solar radio flux per unit frequency at a wavelength of 10.7 cm, near the peak of the observed solar radio emission. Using this average $F10.7$, the Julian Day when the $F10.7$ was as close as possible to this mean value is determined. Once the JD is given in input, the values of electron density N_e for different altitudes, longitudes, and latitudes are computed. From this file, it is chosen to use, for all the analyses presented in this thesis, a profile averaged over latitude and longitude, i.e. keeping the variation only with the orbital altitude. In fact, the orbital altitude is the parameter that has, by far, the highest influence on the electron density. This profile of electron density versus altitude is shown in Fig.2.2.

Acknowledgments

The research I presented in this thesis was financially supported by a PhD grant provided by *Cassa di Risparmio di Padova e Rovigo (CA.RI.PA.RO.)*

I thank Dr. Gonzalo Sanchez-Arriaga for his support and supervision during the three-months period of PhD research I spent at Universidad de Carlos III in Madrid, from beginning April until the end of June 2016.

I thank Dr. Marco Pertile for his help for the vision system analysis presented in Chapter 4.

Lastly, I thank my supervisor Prof. Enrico Lorenzini for his support and important feedback throughout all the stages of my PhD research.

Guido Pastore

Bibliography

[1] Nasa safety standard: Guidelines and assessment procedures for limiting orbital debris. Technical report, August 1995. NSS 1740.14. Office of Safety and Mission Assurance, Washington D.C.

[2] Cospar international reference atmosphere (cira-2012), July 2012.

[3] E. Ahedo and J.R. Sanmartín. *Analysis of Bare-Tether Systems for Deorbiting Low-Earth-Orbit Satellites. Journal of Spacecraft and Rockets*, March-April 2002. Vol.39, No.2.

[4] A.P. Alpatov, V.V. Beletsky, V.I. Dranovskii, V.S. Khoroshilov, A.V. Pirozhenko, Troger H., and A.E. Zakrzhevskii. *Dynamics of Tethered Space Systems.* CRC Press, 1st edition, 2010.

[5] Arianespace. *Ariane 5 User's Manual.* Technical report. Issue 5, Revision 1.

[6] Vladimir S. Aslanov and Alexander S. Ledkov. *Dynamics of Tethered Satellite Systems.* Woodhead Publishing, 1st edition, 2012.

[7] Roger R. Bate, Donald D. Mueller, and Jerry E. White. *Fundamentals of Astrodynamics.* Dover Publications Inc., 1st edition, 1971.

[8] V.V. Beletsky and E.M Levin. *Dynamics of Tethered Space Systems (Advances in the Astronautical Sciences - Volume 83).* American Astronautical Society Publication, 1st edition, 1993.

[9] Paul M. Bellan. *Fundamentals of Plasma Physics.* Cambridge University Press, 1st edition, 2006. ISBN-10 0-521-82116-9.

[10] Claudio Bombardelli, Jesus Pelaez, and Manuel Sanjurio. *Asymptotic Solution for the Current Profile of Passive Bare Electrodynamic Tethers. Journal of Propulsion and Power*, 2010. Vol. 26, No. 6, pp. 1291-1304, DOI: 10.2514/1.46808.

[11] Claudio Bombardelli, Denis Zanutto, and Enrico Lorenzini. *Deorbiting Performance of Bare Electrodynamic Tethers in Inclined Orbits. Journal of Guidance, Control and Dynamics*, September-October 2013. Vol.36, No.5.

[12] X. Chen and J. R. Sanmartin. *Bare-tether cathodic contact through thermionic emission by low-work-function materials. AIP Physics of Plasmas*, July 2012.

[13] J. Corsi and L. Iess. *Stability and Control of Electrodynamic Tethers for deorbiting Applications. Acta Astronautica*, 2001. Vol. 48, No. 5, pg. 491-501.

[14] M.L. Cosmo and E.C. Lorenzini. *Tethers In Space Handbook*. Smithsonian Astrophysical Observatory, 3rd edition, 1997.

[15] National Research Council. *Orbital Debris: A Technical Assessment*. National Academies Press, 1st edition, 1995. ISBN 1558671587.

[16] Howard D. Curtis. *Orbital Mechanics for Engineering Students*. Elsevier Butterworth Heinemann, 1st edition, 2005.

[17] A C Das. *Space Plasma Physics, An Introduction*. Narosa Publishing House, 1st edition, 2004. ISBN 81-7319-575-7.

[18] J. Denzler, M. Zobel, and H. Niemann. *Information theoretic focal length selection for real-time active 3D object tracking*. Technical report. Proceedings of 9th IEEE International Conference on Computer Vision, Nice, France, 2003, pp. 400-407 Vol.1, DOI: 10.1109/ICCV.2003.1238372.

[19] S. Fisher and E. David. *Debris Creation in Geostationary Transfer Orbits: a Review of Launch Practices 2004-2012*. Technical report. 65th International Astronautical Congress, Toronto, Canada, 2014.

[20] A. Gelb. Applied Optimal Estimation. The MIT Press, 16th ed. edition, 2001.

[21] Heiner Klinkrad. *Space Debris Models and Risk Analysis*. Praxis Publishing Ltd., 1st edition, 2006.

[22] L. Kneip, D. Scaramuzza, and R. Siegwart. *A novel parametrization of the perspective-three-point problem for a direct computation of absolute camera position and orientation*. Technical report, 2011. 24th IEEE Conference on Computer Vision and Pattern Recognition, Colorado Springs, USA.

[23] M. Kruijff and E.J. Van der Heide. *Qualification and in-flight demonstration of a European tether deployment system on YES2. Acta Astronautica*, 2008.

[24] R. Mantellato, M. Pertile, G. Colombatti, A. Valmorbida, and E. Lorenzini. *Deorbiting of spacecraft at the end of life with electrodynamic tethers stabilized by passive oscillation dampers*. Technical report. 4th CEAS Air and Space Conference, 2013.

[25] P. Mantri, A. P. Mazzoleni, and D. A. Padgett. *Parametric Study of Deployment of Tethered Satellite Systems. Journal of Spacecraft and Rockets*. Vol. 44, No. 2 (2007), pp. 412-423.

[26] P. Mazzoldi, M. Nigro, and C. Voci. Elementi di Fisica - Elettromagnetismo. Edises, 2nd ed. edition, 2005.

[27] M. Mazzucato, G. Pastore, M. Pertile, and E. Lorenzini. *Vision System for Tether Tip-Mass Detection during Deployment on High-Eccentricity Orbit*. Technical report. Proc. of IEEE Workshop on Metrology for Aerospace, June 2017.

[28] Blake D. Mills. *Satellite Paradox. American Journal of Physics, 27, 115*, 1959.

[29] D. Morris, B. Gilchrist, A. Gallimore, and K. Jensen. *Developing Field Emitter Array Cathode Systems for Electrodynamic Tether Propulsion*. Technical report.

36th AIAA/ASME/SAE/ASEE Joint Propulsion Conference and Exhibit, 16-19 July 2000.

[30] Kerry T. Nock, Kim M. Aaron, and Darren McKnight. *Removing Orbital Debris with Less Risk. Journal of Spacecraft and Rockets*, March-April 2013. Vol. 50, No. 2, pp. 365-379, DOI: 10.2514/1.A32286.

[31] G. Pastore. Debris mitigation in leo orbits: Performance analysis and comparison of different deorbit systems, July 2014.

[32] G. Pastore, E. Lorenzini, and G. Sanchez-Arriaga. *Deorbit with Bare Tether System from High Eccentricity Initial Orbit: Analyses and Numerical Simulations.* Technical report. Conference *Tethers in Space 2016*, May 2016, Ann Arbor.

[33] J. Pelaez and M. Sanjurjo. *Generator Regime of Self-Balanced Electrodynamic Bare Tethers. Journal of Spacecraft and Rockets.* 43, 6, 1359-1369, 2006.

[34] Lorenzini E. C. Lopez-Rebollal O. Pelaez, J. and M. Ruiz. *A new kind of dynamic instability in electrodynamic tethers. The Journal of the Astronautical Science.* Vol. 48, No. 4, October-December, 449-476, 2000.

[35] J. Peláez and Y.N. Andrés. *Dynamic Stability of Electrodynamic Tethers in Inclined Elliptical Orbits. Journal of Guidance, Control, and Dynamics.* Vol.28, No.4, July-August 2005, Pg.611-622.

[36] M. Pertile, S. Chiodini, S. Debei, and E. Lorenzini. *Uncertainty comparison of three visual odometry systems in different operative conditions. Measurement*, 2016. Vol. 78, pp. 388–396.

[37] G. Sanchez-Arriaga, C. Bombardelli, and X. Chen. *Impact of Nonideal Effects on Bare Electrodynamic Tether Performance. Journal of Propulsion and Power.* Vol. 31, No. 3 (2015), pp. 951-955, DOI: 10.2514/1.B35393.

[38] M. Sanjurjo-Rivo, G. Sánchez-Arriaga, and J. Peláez. *Efficient Computation of Current Collection in Bare Electrodynamic Tethers in and beyond OML Regime. J. Aerosp. Eng.* 2014, 10.1061/(ASCE)AS.1943-5525.0000479.

[39] J. R. Sanmartin. *Macroscopic Motion and Gravitation in Thermodynamics. European Journal of Physics*, 1995.

[40] J. R. Sanmartin, E. C. Lorenzini, and M. Martinez-Sanchez. *Electrodynamic Tether Applications and Constraints. Journal of Spacecraft and Rockets, Vol.47, No.3*, May-June 2010.

[41] J.R. Sanmartín and R.D. Estes. *The Orbital-Motion-Limited Regime of Cylindrical Langmuir Probes. Physics of Plasmas.* Vol.6, No.1, 1999, pp.395-405.

[42] J.R. Sanmartín, M. Martínez-Sánchez, and E. Ahedo. *Bare Wire Anodes for Electrodynamic Tethers. Journal of Propulsion and Power.* Vol.9, No.3, May-June 1993.

[43] Nickolay N. Smirnov. *Space Debris Hazard Evaluation and Mitigation.* Taylor and Francis, 1st edition, 2002.

[44] Peter A. Swan. *Dynamics and Control of Tethers in Elliptical Orbits*. PhD thesis, University of California, Los Angeles, 1984.

[45] N. Takeichi. *Practical Operation Strategy for Deorbit of an Electrodynamic Tethered System. Journal of Spacecraft and Rockets*, November-December 2006.

[46] Eric J. Van der Heide and Michiel Kruijff. *Tethers and debris mitigation. Acta Astronautica, Vol.48, No.5-12, pp.503-516*, March-June 2001. Published by *Elsevier Science Ltd.*

[47] F.R. Vigneron, F. Schultz, A.M. Jablonski, and G. Tyc. *Tether Deployment and Trajectory Modeling for Space Plasma Science Missions. Journal of Spacecraft and Rockets*, 2000. Vol.37, No.1.

[48] James R. Wertz. *Spacecraft Attitude Determination and Control.* D. Reidel Publishing Company, 1st edition, 1978.

[49] James R. Wertz and Wiley J. Larson. *Space Mission Analysis and Design.* Space Technology Library, 3rd edition, 1999.

[50] Sanmartin J. R. Williams, J.R. and L. P. Rand. *Low Work-Function Coating for an Entirely Propellantless Bare Electrodynamic Tether.* Technical report. IEEE Transactions on plasma Science, 40, 5, 1441-1445, 2012.

[51] Y. Yamagiwaa, M. Nohmia, Y. Aokib, Y. Momonoia, H. Nanbaa, M. Aigaa, T. Kumaoa, and M. Watahikia. *Space experiments on basic technologies for a space elevator using microsatellites. Acta Astronautica.* Article in press. Accepted on 19 December 2016.

[52] D. Zanutto, E. C. Lorenzini, R. Mantellato, G. Colombatti, and A. Sanchez-Torres. *Orbital debris mitigation through deorbiting with passive electrodynamic drag.* Technical report, University of Padova, Universidad Politécnica de Madrid, 2012. 63rd International Astronautical Congress, Naples, Italy.